Università degli Studi di Napoli *Federico II*

DOTTORATO DI RICERCA IN
FISICA FONDAMENTALE ED APPLICATA

Ciclo: XXVII

Coordinatore: prof. Raffaele Velotta

Engineering spin and orbital angular momentum interactions in a light beam: quantum and classical applications

Settore Scientifico Disciplinare FIS/03

Dottorando
Filippo Cardano

Tutori
Prof. Lorenzo Marrucci
Prof. Enrico Santamato

Anni 2012/2015

Corto Maltese. *Tango*, di Hugo Pratt.

Acknowledgements

At the end of this doctorate project, I would like to thank some people that helped me to carry out my research activity. I thank my two supervisors, **Lorenzo Marrucci** and **Enrico Santamato**; they taught me what being a scientist means. I thank **Ebrahim Karimi**, for our collaboration and for teaching me how to work in the lab. I thank **Domenico Paparo**, for his suggestions and support, and **Corrado de Lisio**, for his help with the laser system. I thank **Maria Maffei**, **Francesco Massa** and **Hammam Qassim**, for their valuable help in the experimental activities and for their patience. I thank **Robert W. Boyd** and **Fabio Sciarrino**, for giving me the chance to spend few months in their research groups. Finally, I thank my friends and colleagues who made me enjoy these years.

Published articles related to my thesis

1. **F. Cardano**, E. Karimi, L. Marrucci, C. de Lisio, and E. Santamato. **Generation and dynamics of optical beams with polarization singularities.** *Opt. Express* **21**, 8815–8820 (2013).

2. **F. Cardano**, E. Karimi, L. Marrucci, C. de Lisio, and E. Santamato. **Violation of leggett-type inequalities in the spin-orbit degrees of freedom of a single photon.** *Phys. Rev. A* **88**, 032101 (2013).

3. V. D'Ambrosio, **F. Cardano**, E. Karimi, E. Nagali, E. Santamato, L. Marrucci, and F. Sciarrino. **Test of mutually unbiased bases for six-dimensional photonic quantum systems.** *Sci. Rep.* **3**, 2726 (2013)

4. E. Karimi, **F. Cardano**, M. Maffei, C. de Lisio, L. Marrucci, R. W. Boyd, and E. Santamato. **Hardy's paradox tested in the spin-orbit Hilbert space of single photons.** *Phys. Rev. A* **89**, 032122 (2014).

5. **F. Cardano**, F. Massa, H. Qassim, E. Karimi, S. Slussarenko, D. Paparo, C. de Lisio, F. Sciarrino, E. Santamato, R. W. Boyd, and L. Marrucci. **Quantum walks and wavepacket dynamics on a lattice with twisted photons.** *Science Advances* **1**, e1500087 (2015).

6. **F. Cardano**, M. Maffei, F. Massa, B. Piccirillo, C. de Lisio, G. De Filippis, V. Cataudella, E. Santamato, and L. Marrucci. **Direct experimental signature of a topological phase transition in a photonic quantum walk.** *In preparation.*

I will explicitly mention in a footnote when a section contains paragraphs, figures or tables that are adapted or copied "verbatim" from one of these articles.

Abstract

Light is a fundamental element in nature. The observation of a large variety of physical phenomena gives the opportunity to catch its intriguing features, which have made it a cornerstone of modern technology. Thanks to an intense theoretical and experimental investigation, nowadays we know that light carries energy, linear and angular momentum, which can be exchanged with matter as a result of an interaction. These quantities can be measured in an experiment and thus represent physical observables both for classical radiation and single photons, the quanta of the electromagnetic (e.m.) field.
The angular momentum (AM) of light is the main ingredient of this work. Here the attention will be concentrated on specific physical architectures where the AM of the e.m. radiation can be considered as the sum of two independent terms, the spin and the orbital components, in analogy to particle systems. It will be clear later on that the spin angular momentum (SAM) is related to the polarization of the optical beam, that is the direction of the oscillating electric field, whereas the orbital angular momentum (OAM) is associated with the spatial distribution of the field. Being independent, SAM and OAM have been discovered and explored in separate contexts for many years, while only recently it has been considered the possibility to address both quantities on the same beam (or individual photons). The interaction between light SAM and OAM gives rise to complex structures of the electromagnetic field, or to the so called classical entanglement in the domain of single photons. This "structured light" has unique features both in classical and quantum optics.
The research presented in this work aimed to show that combining the SAM and OAM in light beams or single photons may be a useful tool for a variety of applications, with particular interest to the case of architectures characterized by spin-orbit interaction. This concept was made concrete through the design and the realization of several experiments, in the framework of singular optics, foundations of quantum mechanics, quantum information theory and quantum simulation.
In order to present clearly the main ideas developed in this research work and the results that have been obtained, this manuscript is divided in five chapters. Chapter 1 is devoted to an introduction of the spin and the orbital angular momenta for a light beam, or

single photons as well, with particular attention to the devices that allow to manipulate these two quantities and to let them interact. In the framework of singular optics, in Chapter 2 it is presented the idea of generating structured light and polarization singularities through spin-orbit interaction in a standard Gaussian beam. In Chapter 3 it is shown how the control of the "classical" entanglement between the SAM and the OAM of a single photon may be exploited as a resource for fundamental tests of quantum mechanics. In Chapter 4 we describe the encoding of qu-dits of quantum information in the spin-orbit space of a single photon; in particular we generated and characterized a set of three mutually unbiased bases for a six-dimensional photonic quantum system. Chapter 5 is about the realization of a photonic platform for the simulation of a simple quantum dynamics, the so called Quantum Walk, which has been exploited to demonstrate a topological phase transition. We conclude the manuscript with a summary of the obtained results and giving an overview of possible prospects.

Contents

Chapter 1

Light beams carrying Spin and Orbital Angular Momenta

1.1 Introduction

A physicist typically learns the basic ideas of energy and momentum for particles, as they can be associated with simple phenomena belonging to a daily experience (playing pool can be an appropriate example!). Similarly we may guess that such "mechanical" properties characterize light as well. A child using a lens to focus the sunlight on a sheet of paper observes that the latter may burn; this is due to the energy transfer from light to the foil, as a result of absorption. Though not as dramatic, it is the same thing happening when we feel our skin warming up after sun exposure. Comets are famous thanks to their bright tail. This is made of frozen particles which leave the comet's surface because of the pressure of the sunlight: the latter carries linear momentum, which is transferred to the particles that eventually form the tail.

Following the same strategy, we can understand the concepts of Spin Angular Momentum (SAM) and Orbital Angular Momentum (OAM). Let us consider a particle which is shined by a light beam; it has been demonstrated experimentally [1] that tailoring suitably the beam features, the interaction between the light and the particle can result in two kinds of rotation. As a gyroscope, the latter can spin around its axis, or as a planet it can move on a circular orbit around the beam center (see 1.1, or [1], Fig. 3 for an experimental image). The two different motions occurr when light is carrying SAM or OAM, respectively; we will discuss later on what characterizes these states of light and how they can be generated.

Energy and momenta of light can be introduced formally in the framework of classical electromagnetism, described by the Maxwell theory. It is well known that light is made

of an electric ($\vec{\mathbf{E}}$) and a magnetic field ($\vec{\mathbf{B}}$), oscillating in space and time [we omit the explicit dependance on spatial and temporal coordinates (x,y,z,t)] according to the fundamental Maxwell's equations, which in free space are given by

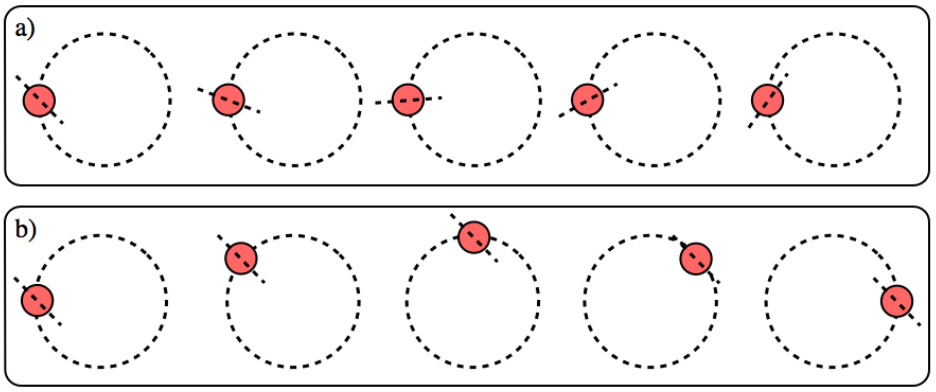

FIGURE 1.1: Naive representation of the mechanical action produced by SAM and OAM of light interacting with a particle. a) The SAM of the impinging light beam induces a rotation of the system around its own axes, parallel to the beam propagation direction. b) The OAM-particle interaction results in a rotation of the whole system around the beam center. Figures from the left to the right are considered as corresponding to increasing temporal frames. This image is a schematic representation of the experimental data reported in Fig. [1] Fig. 3.

$$\nabla \cdot \vec{\mathbf{E}} = 0, \tag{1.1}$$

$$\nabla \cdot \vec{\mathbf{B}} = 0, \tag{1.2}$$

$$\nabla \times \vec{\mathbf{E}} = -\frac{\partial \vec{\mathbf{B}}}{\partial t}, \tag{1.3}$$

$$\nabla \times \vec{\mathbf{B}} = \frac{1}{c^2}\frac{\partial \vec{\mathbf{E}}}{\partial t} \tag{1.4}$$

where c is the vacuum speed of light. With the help of some algebra we can show that equations 1.3 and 1.4 are equivalent to the standard wave equations for the e.m. field

$$\nabla^2 \vec{\mathbf{E}} - \frac{1}{c^2}\frac{\partial^2}{\partial t}\vec{\mathbf{E}} = 0, \tag{1.5}$$

$$\nabla^2 \vec{\mathbf{B}} - \frac{1}{c^2}\frac{\partial^2}{\partial t}\vec{\mathbf{B}} = 0. \tag{1.6}$$

When solving these equations to determine the e.m. field, we have to require that the solutions verify Eqs.1.1 and 1.2 as well, since the latter have been used for deriving Eqs. 1.5 and 1.6. The energy density w, the linear momentum density $\vec{\mathbf{p}}$ and the angular momentum density $\vec{\mathbf{j}}$ are defined in terms of the fields $\vec{\mathbf{E}}$ and $\vec{\mathbf{B}}$

$$w = \frac{1}{2}\epsilon_0|\vec{\mathcal{E}}|^2 + \frac{1}{2}\mu_0^{-1}|\vec{\mathcal{B}}|^2, \tag{1.7}$$

$$\vec{\mathbf{p}} = \epsilon_0\,\Re\,(\vec{\mathcal{E}} \times \vec{\mathcal{B}}), \tag{1.8}$$

$$\vec{\mathbf{j}} = \epsilon_0\,\vec{\mathbf{r}} \times (\vec{\mathcal{E}} \times \vec{\mathcal{B}}). \tag{1.9}$$

Here we are have introduced the complex fields $\vec{\mathcal{E}}$ and $\vec{\mathcal{B}}$, whose real parts correspond to the actual fields $\vec{\mathbf{E}}$ and $\vec{\mathbf{B}}$; this is a standard approach in the electromagnetic theory and we will keep this notation through the whole manuscript.
In a system of particles, the total angular momentum $\vec{\mathbf{J}}$ can be written as $\vec{\mathbf{J}} = \vec{\mathbf{S}} + \vec{\mathbf{L}}$, where $\vec{\mathbf{L}}$ is the angular momentum of the center of mass $\vec{\mathbf{x}}_c$, while $\vec{\mathbf{S}}$ is the angular momentum of the particles calculated with respect to $\vec{\mathbf{x}}_c$. There have been a lot of efforts in trying to identify internal and external angular momenta in light as well; nevertheless, such separation is still not entirely clear and is the subject of an ongoing research. For instance, it has been suggested that for a correct separation to hold, the right quantity to be considered is not $\vec{\mathbf{j}}$ but the angular momentum flux density, which can be introduced starting from the conservation law for the angular momentum in e.m. waves [2]. On the other hand, there exist a specific limit in which a clear and meaningful separation can be obtained. It is the case of the paraxial limit of the electromagnetic theory. In this approximation, the attention is limited to a subclass of solutions of Maxwell's equations 1.1-1.4 associated with light beams that, while propagating in a specific direction, remain well confined around the propagation axis with a slow variation of their spatial distribution. Such features are quite common; for example all beams generated from standard laser sources satisfy such requirements. The component of the angular momentum $\vec{\mathbf{J}}$ along the propagation axis can be correctly written as

$$J_z = S_z + L_z \tag{1.10}$$

where S_z and L_z are well defined distinct quantities and can be measured independently [1, 3, 4]. The theoretical and experimental research described in this thesis is entirely based on paraxial beams, so it is assumed not necessary to present all the debate existing about the spin-orbit separation for a generic e.m. wave (as an example, you can consider [2, 4–7] and references therein); the attention will be rather focused on paraxial beams or, equivalently, to the paraxial approximation of quantum optics.

1.2 Paraxial approximation for electromagnetic waves

Properties of the e.m. field may be conveniently described introducing the potentials $\vec{\mathbf{A}}$ and ϕ, defined by the relations

$$\vec{\mathbf{E}} = -\nabla\phi - \frac{1}{c}\frac{\partial}{\partial t}\vec{\mathbf{A}} \tag{1.11}$$

$$\vec{\mathbf{B}} = \nabla \times \vec{\mathbf{A}} \tag{1.12}$$

Let us concentrate on the vector potential $\vec{\mathbf{A}}$; it can be shown that it obeys a wave equation, similarly to $\vec{\mathbf{E}}$ and $\vec{\mathbf{B}}$

$$\nabla^2\vec{\mathbf{A}} - \frac{1}{c^2}\frac{\partial^2}{\partial t}\vec{\mathbf{A}} = 0. \tag{1.13}$$

$$\tag{1.14}$$

Introducing the complex vector potential $\vec{\mathcal{A}}$, we can assume a harmonic temporal dependance, that is $\vec{\mathcal{A}}(x,y,z,t) = \vec{\mathcal{A}}(x,y,z)e^{i\omega t}$. In this case, the Helmotz equation is obtained

$$\nabla^2\vec{\mathcal{A}} + \frac{\omega^2}{c^2}\vec{\mathcal{A}} = 0, \tag{1.15}$$

A standard set of solutions is given by plane waves $\vec{\mathcal{A}} = \hat{\mathbf{u}}\,\mathcal{A}_0\,e^{-i\,\vec{\mathbf{k}}\cdot\vec{\mathbf{r}}}$, where the wave vector $\vec{\mathbf{k}}$ has to satisfy the dispersion relation $|\vec{\mathbf{k}}|^2 = k^2 = \omega^2/c^2$. The unit vector $\hat{\mathbf{n}}$ defines the direction of the oscillating electric field, which is usually referred as polarization. Eq. 1.1 forces the polarization to lie in a plane transverse to the propagation direction, that is $\hat{\mathbf{n}}\cdot\vec{\mathbf{k}} = 0$; remaining confined in such plane, the polarization can change in time as we will show below.

Plane waves propagate along a specific direction, defined by the vector $\vec{\mathbf{k}}$, but they are infinitely extended, so they cannot be realized in a laboratory. In order to have a physical solution of Maxwell's equation similar to a plane wave, we write the field as

$$\vec{\mathcal{A}} = \hat{\mathbf{n}}\,u(x,y,z)e^{i(kz-\omega t)} \tag{1.16}$$

where u is a complex envelope. When putting the latter expression in Eq. 1.15, we get the equation for the envelope u

$$\nabla^2 u + 2ik\frac{\partial}{\partial z}u = 0. \tag{1.17}$$

Requiring u to vary slowly along z, the second order derivative can be neglected

$$\frac{1}{k^2}\left|\frac{\partial^2}{\partial x^2}u\right| \leq \frac{1}{k}\left|\frac{\partial}{\partial x}u\right| \tag{1.18}$$

and Eq. 1.17 turns into the so called paraxial wave equation (PWE)

$$\frac{\partial^2}{\partial x^2}u + \frac{\partial^2}{\partial y^2}u + 2ik\frac{\partial}{\partial z}u = 0. \tag{1.19}$$

Simple arguments can be used to show that the condition 1.18 basically corresponds to neglecting components of the field of order k_T^2/k^2 or higher, where k_T is wave-vector component in the plane orthogonal to the propagation direction.
To introduce the concepts of Spin Angular Momentum and Orbital Angular Momentum, we express the vector potential $\vec{\mathbf{A}}$ in cylindrical coordinates, assigning a specific dependance on the azimuthal coordinate φ, compatible with the PWE 1.19:

$$\vec{\mathcal{A}} = (\alpha\,\hat{\mathbf{x}} + \beta\,\hat{\mathbf{y}})\,u(r,z)e^{im\varphi}e^{i(kz-\omega t)} \tag{1.20}$$

where α and β are complex coefficients satisfying the normalization condition $|\alpha|^2 + |\beta|^2 = 1$, and m is an integer. The energy and angular momentum densities can be computed for fields $\vec{\mathbf{E}}$ and $\vec{\mathbf{B}}$ associated with this potential, using the Lorentz Gauge condition $\nabla\cdot\vec{\mathbf{A}} - 1/c\partial_t\phi = 0$ and Eqs. 1.7 and 1.9. The final result is (for details about the calculation you can refer to [8, 9]:

$$j_z = \omega\epsilon_0 l|u|^2 - \sigma_z\epsilon_0\frac{r}{2}\frac{\partial}{\partial r}|u|^2 \tag{1.21}$$

$$w = \epsilon_0\omega|u|^2 \tag{1.22}$$

where $\sigma_z = 2\Im(\alpha\beta^*)$. Integrating these quantities over the all space, we get the important expression

$$\frac{J_z}{W} = \frac{\sigma_z + m}{\omega}. \tag{1.23}$$

The Spin Angular Momentum S_z, proportional to the quantity σ_z, is associated with the polarization degree of freedom; any change of spatial distribution of field does not alter its value. The Orbital Angular Momentum L_z, proportional to the integer m, is a result of the field distribution over the plane perpendicular to the propagation direction, in particular of the phase factor $e^{im\varphi}$, and it is not related to the polarization. So, for a paraxial wave, SAM and OAM are well defined, independent quantities. In the domain of quantum optics, they are associated with quantum operators $\widehat{S}_z$ and $\widehat{L}_z$, verifying the

commutation relation

$$\left[\widehat{S}_z, \widehat{L}_z\right] = 0. \tag{1.24}$$

The associated eigenvalues are proportional to $\hbar$, which represents the elementary AM unit that can be carried by a single photon. While for such particle the SAM may be only $\pm\hbar$, the OAM spectrum is not bound and individual photons may carry $m\hbar$ orbital angular momentum, where m is an integer number. Eq. 1.24 guarantees that the SAM and OAM are compatible observables.

1.3 The SAM space

The polarization of a light beam determines its spin angular momentum content. In the paraxial regime, the electric field is approximatively transverse to the propagation direction ($\vec{\mathbf{E}} \cdot \vec{\mathbf{k}} \simeq 0$) and proportional to the vector potential $\vec{\mathbf{A}}$; these conditions can be obtained from Eqs. 1.1 and 1.11, respectively, neglecting the second order derivatives of the field with respect to the spatial coordinates. As a consequence, in this context we can refer to both $\vec{\mathbf{A}}$ or $\vec{\mathbf{E}}$ equivalently. In the most general case, the direction and the modulus of the vector $\vec{\mathbf{E}}(x, y)$ will depend on the transverse coordinates (x, y). Since we want to focus our attention on the possible polarization states, we will not consider the spatial dependance of the field, assuming the vector $\vec{\mathbf{E}}$ to be uniform in the transverse plane. This spatial structure is the key element for the orbital angular momentum of light, as we will discuss below.
The electric field, orthogonal to the propagation direction, can be written as

$$\vec{\mathcal{E}} = c_h\, \hat{\mathbf{e}}_h + c_v\, \hat{\mathbf{e}}_v \tag{1.25}$$

where unit vectors $(\hat{\mathbf{e}}_h, \hat{\mathbf{e}}_v)$ are oriented as the (x, y) axes, while (c_h, c_v) are complex numbers: in such representation, the intensity of the field is given by $|\vec{\mathbf{E}}|^2 = |c_h|^2 + |c_v|^2$. Being interested only in the polarization of the field, we can require its intensity to be normalized, that is $|c_h|^2 + |c_v|^2 = 1$. In the future we may consider other basis, in particular the diagonal and the circular ones. They are defined as

$$\hat{\mathbf{e}}_a = \frac{1}{\sqrt{2}}(\hat{\mathbf{e}}_h - \hat{\mathbf{e}}_v), \quad \hat{\mathbf{e}}_d = \frac{1}{\sqrt{2}}(\hat{\mathbf{e}}_h + \hat{\mathbf{e}}_v) \tag{1.26}$$

$$\hat{\mathbf{e}}_l = \frac{1}{\sqrt{2}}(\hat{\mathbf{e}}_h + i\,\hat{\mathbf{e}}_v), \quad \hat{\mathbf{e}}_r = \frac{1}{\sqrt{2}}(\hat{\mathbf{e}}_h - i\,\hat{\mathbf{e}}_v). \tag{1.27}$$

Labels h, v, a, d, l, r stand for horizontal, vertical, anti-diagonal, diagonal, left-circular and right circular, respectively; the meaning of this notation will be clear soon. In the

quantum regime, the polarization of a single photon is represented similarly using the Dirac notation

$$|E\rangle = c_h\,|H\rangle + c_v\,|V\rangle \tag{1.28}$$

Kets $|H\rangle$ and $|V\rangle$ represent a single photon which is horizontally or vertically polarized, respectively. In this case, state normalization requires that $|c_h|^2 + |c_v|^2 = 1$. Eqs. 1.25 and 1.28 are equivalent and the single particle quantum formalism of Dirac kets maybe extended to the classical picture. In this framework, in analogy with Eq. 1.26 we define the states associated with diagonal and circular polarizations

$$|A\rangle = \frac{1}{\sqrt{2}}\begin{pmatrix}1\\-1\end{pmatrix} \tag{1.29}$$

$$|D\rangle = \frac{1}{\sqrt{2}}\begin{pmatrix}1\\1\end{pmatrix} \tag{1.30}$$

$$|L\rangle = \frac{1}{\sqrt{2}}\begin{pmatrix}1\\i\end{pmatrix} \tag{1.31}$$

$$|R\rangle = \frac{1}{\sqrt{2}}\begin{pmatrix}1\\-i\end{pmatrix} \tag{1.32}$$

Both in classical or quantum formalism, the polarization state of a single photon is fully determined by the pair of complex numbers (c_h, c_v), where only two out of four real parameters are independent; indeed the normalization condition fixes a first constraint, which has to be added to the consideration that the state in Eqs. 1.25 and 1.28 is defined up to a global phase factor. It is usual to have a compact expression for the field, introducing a 2-d complex vector

$$|E\rangle = \begin{pmatrix}c_h\\c_v\end{pmatrix} \tag{1.33}$$

Including the harmonic dependance in Eq. 1.25 or 1.33, we get the oscillating field:

$$\vec{\mathcal{E}}(t) = (c_h\,\hat{\mathbf{e}}_h + c_v\,\hat{\mathbf{e}}_v)e^{-i\omega t}. \tag{1.34}$$

In the previous equation, we are assuming that the relative phase $\alpha = \mathrm{Arg}(c_v/c_h)$ between the two components does not change in time, that is the field is a coherent superposition of H and V polarizations; this case is not general, since partially polarized states are possible when allowing α to have random oscillations. These states can be described introducing the density operator formalism in the quantum domain (see

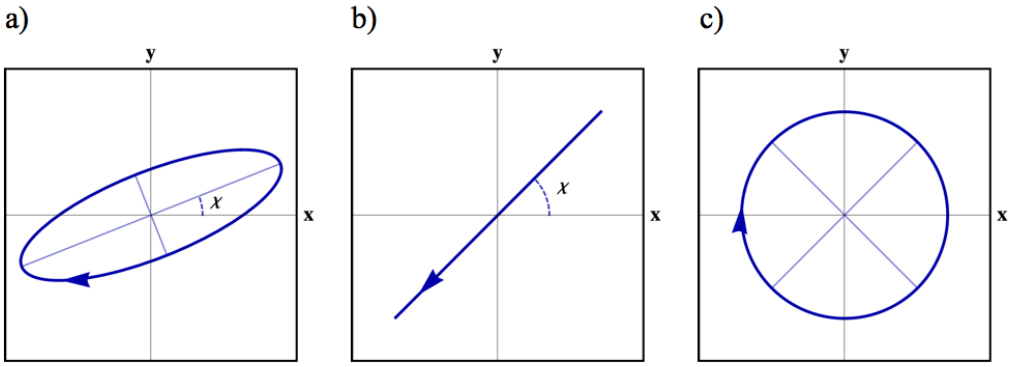

FIGURE 1.2: Temporal evolution of the electric field in the transverse plane. In a paraxial and harmonic electromagnetic wave which is uniformly polarized, at every point in the transverse plane the electric field changes in time describing an elliptical trajectory, whose properties (orientation and eccentricity) are determined by the coefficients c_h and c_v. a) In the most generic case, the polarization trajectory is an ellipse. b) When $\mathrm{Arg}(c_v/c_h) = n\pi$, the polarization is linear. c) When $c_v/c_h = \pm i$, we obtain circularly polarized light. In all figures, we are representing the field at the origin, corresponding to the intersection of the propagation axis and a generic transverse plane.

Sec.4.3), or equivalently using the Stokes representation that will be presented below. The electric field $\vec{\mathbf{E}}(t)$ is the the real part of Eq. 1.34; as shown in Fig 1.2, this vector changes in time following an elliptical trajectory, usually referred to as polarization ellipse. In this representation, the independent parameters determining the polarization state are the eccentricity of the orbit and its orientation; coefficients (c_h, c_v) can be obtained directly from such quantities (up to a global phase) [10].

Two specific configurations deserve to be mentioned. When α is a multiple of π, the polarization ellipse is squeezed into line, oriented at $\chi = \mathrm{Tan}^{-1}(|c_v/c_h|)$ (Fig. 1.2, b)). On the other hand, when $c_v/c_h = \pm i$ the polarization ellipse results into a circle (Fig. 1.2, c)). Anti-clockwise and clockwise rotations of the field are referred as Left-Circular (LCP) and Right-Circular (RCP) polarizations, respectively. Circularly polarized e.m. waves are relevant in the context of spin angular momentum; indeed for these states the SAM takes its extreme values, being $\sigma_z = 2\Im(c_h^* c_v) = \pm 1$ for LCP and RCP, respectively. In the quantum domain, left-circularly and right-circularly polarized photons represent the eigenstates of the quantum operator $\widehat{S}_z$, and they carry a spin angular momentum equal to $\pm\hbar$ along the propagation direction, respectively. In Fig. 1.3 we report the field evolution along the propagation direction, at a given time t, for linear and circular polarizations.

The polarization state of a light beam can be assigned either in terms of the field components (c_h, c_v), or specifying the features of the polarization ellipse. We introduce now other two possible representations: the Poincaré sphere and the Stokes parameters. The latter are four real numbers, which are usually labelled as S_0, S_1, S_2 and S_3; they are

related to the field components in the three different bases introduced hitherto and are defined as follows

$$\begin{aligned} S_0 =& |c_l|^2 + |c_r|^2 = |c_h|^2 + |c_v|^2 = |c_a|^2 + |c_d|^2, \\ S_1 =& |c_h|^2 - |c_v|^2, \\ S_2 =& |c_d|^2 - |c_a|^2, \\ S_3 =& |c_l|^2 - |c_r|^2. \end{aligned} \tag{1.35}$$

The quantities $|c_j|^2$ can be measured by combining wave-plates and polarizers, plus a

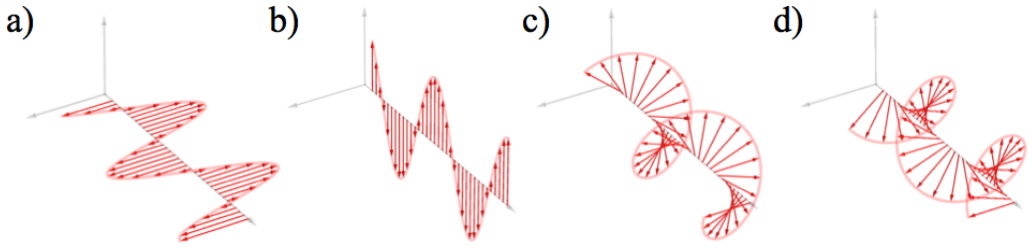

FIGURE 1.3: Evolution of the polarization along the propagation axis. At a given time t, we consider the electric field at different points of the z axis. a) and b) represent linear horizontal and vertical polarizations, respectively, where the vector $\vec{\mathbf{E}}$ changes its modulus while its orientation is uniform. The reverse behavior can be observed in panels c) and d), representing left and right circular polarizations, respectively. In this case, $\vec{\mathbf{E}}$ has a fixed modulus but changes its direction describing a helix, with a pitch equal to the wavelength of the radiation.

standard device for the measurement of the intensity of the e.m. field. As a consequence, the Stokes parameter can be easily measured in a simple experimental architecture. When the light beam is fully polarized, we have that $S_0^2 = S_1^2 + S_2^2 + S_3^2$. Accordingly, can introduce the reduced Stokes parameters, defined as $s_i = S_i/S_0$, with $i \in \{1, 2, 3\}$. If we consider a Cartesian frame where $\{s_1, s_2, s_3\}$ are the three coordinates along the (x, y, z) axes, we can observe that all polarizations states are positioned on a spherical surface with unit radius. This sphere is usually referred to as the Poincaré sphere. Cartesian coordinates given by the reduced Stokes parameters can be replaced by the polar angles (θ, ϕ). Referring to the circular basis $(\hat{\mathbf{e}}_L, \hat{\mathbf{e}}_R)$, coefficients (c_l, c_r) may be conveniently expressed in terms of (θ, ϕ)

$$|E\rangle = \begin{pmatrix} \cos\left(\frac{\theta}{2}\right) \\ e^{i\varphi} \sin\left(\frac{\theta}{2}\right) \end{pmatrix} \tag{1.36}$$

Here we have defined the sphere so as to have north and south poles corresponding the LCP and RCP, respectively. We report this Poincaré sphere in Fig. 1.4. Stokes parameters or the Poincaré sphere representation can be used to describe partially polarized

states of light; since for partial polarizations $0 \leq s_i \leq 1$ ($S_0^2 \geq S_1^2 + S_2^2 + S_3^2$) we have to consider all the inner points of the sphere. In this general representation, on the surface of the sphere we find fully polarized states, whereas the origin is associated with the state which is completely unpolarized.

As a conclusion, we remark that circularly polarized light carries a finite value of SAM along the propagation direction, equal to $\pm\hbar$ per photon. Once the polarization state is assigned, the quantity S_z may be evaluated introducing the associated operator $\widehat{S}_z$; according to the different notations, it can be expressed as

$$\widehat{S}_z = \hbar\left(|L\rangle\langle L| - |R\rangle\langle L|\right) \tag{1.37}$$

$$\widehat{S}_z = \hbar \begin{pmatrix} 1 & 0 \\ 0 & -1 \end{pmatrix} \tag{1.38}$$

where we have used LCP and RCP as basis vectors.

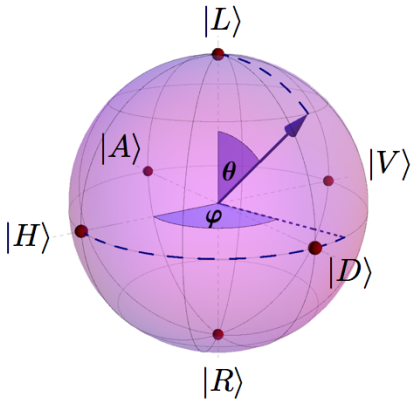

FIGURE 1.4: Poincaré sphere for the SAM space of light. In this representation, where the angles (θ, ϕ) are defined in Eq.1.36, north and south poles correspond to $|L\rangle$ and $|R\rangle$, respectively, while all linear polarizations are positioned on the equator of the sphere.

1.4 The OAM space

The strategy we adopted to characterize the state of a paraxial electromagnetic wave relies on the consideration that it is possible to have the electric field direction uniform in the transverse plane, with a space-varying amplitude. In the previous section we

provided a complete description of the polarization degree of freedom of the field, introducing the SAM space. We concentrate now on the spatial distribution described by the complex envelope $u(\rho, \varphi, z)$ and the associated Orbital Angular Momentum content.
A light beam carries OAM if its envelope depends on the azimuthal coordinate φ through the phase factor $e^{im\varphi}$ (see Eq. 1.20). The latter characterizes different sets of solutions of the paraxial wave equation (Eq. 1.19), as for example Laguerre Gauss (LG), Bessel and Hyper Geometric (HYGG) beams [10, 11]. Although all these beams may have a complex structure, they are characterized by a common feature. The term $e^{im\varphi}$ determines the geometry of the wavefronts of the field, which has a helical shape as shown in Fig. 1.5. Points on the propagation axes z are affected by a phase singularity (where the latter is not defined), and, as a consequence, by a vanishing field (see Fig. 1.6 for an example). Helical wavefronts and zero-intensity on the propagation axis are general properties of e.m. waves carrying OAM, which are referred to as helical modes of light.
Helical modes represent a complete set of states to describe the azimuthal structure of

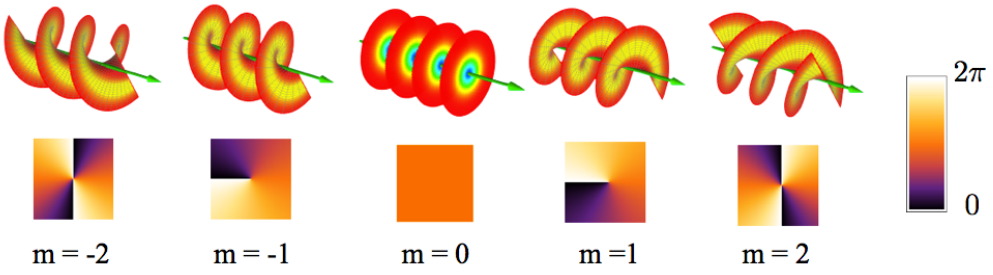

FIGURE 1.5: Wavefront structure and phase distribution of helical modes of light. The color scale for the phase plot is reported on the right of the figure. This image is adapted from the Wikipedia page "Orbital Angular Momentum of light", edited by L. Marrucci and E. Karimi.

a light beam, which is described by the OAM space. In the Dirac notation, we can refer to these modes as $|m\rangle$. As stated below, they are orthonormal

$$\langle m|m'\rangle = \int_0^{2\pi} \frac{\mathrm{d}\varphi}{2\pi} e^{-i(m-m')\varphi} = \delta_{m,m'} \tag{1.39}$$

and provide the basis to express any state in the OAM space (in the previous equation $\delta_{m,m'}$ is the Kronecker discrete function)

$$|\psi\rangle_o = \sum_{m=-\infty}^{\infty} c_m |m\rangle_o. \tag{1.40}$$

It is worth to mention that functions $e^{im\phi}$ provide the basis for the Discrete Fourier Transform of the periodic coordinate φ; m and φ are conjugate variables.

A quantum operator $\widehat{L}_z$ is associated with the component of the OAM along the propagation direction; we can represent it in terms of its eigenstates $|m\rangle$:

$$\widehat{L}_z = \sum_{m=-\infty}^{\infty} \hbar\, m\, |m\rangle\langle m| \tag{1.41}$$

Helical modes and the associated OAM space describe the azimuthal structure of a paraxial beam; for a complete characterization of these e.m. waves, we need to consider the distribution of the field along the radial coordinate. For this purpose, we may consider specific solutions of the paraxial wave equation, as for instance the set of Laguerre-Gauss modes. We dedicate a separate section to the introduction of these particular modes, representing probably the simplest example of light beams carrying orbital angular momentum[3].

1.4.1 Laguerre-Gauss modes of light

In 1992 Allen and coworkers realized for the first time that LG modes carry Orbital Angular Momentum [3]; this represented the starting point of a very productive research area, still very active, focused on the OAM of light and its applications (see [4] for a review). Laguerre-Gauss modes have the following expression

$$\mathrm{LG}_{p,m}(r,\phi,z) = A_{p,m} \left(\frac{r}{w(z)}\right)^{|m|} e^{-\frac{r^2}{w(z)^2}} L_p^{|m|}\left(\frac{2r^2}{w(z)^2}\right) e^{\frac{i\pi r^2}{\lambda R(z)}}\, e^{im\phi}\, e^{-i(2p+|m|+1)\arctan\left(\frac{z}{z_R}\right)}, \tag{1.42}$$

where the normalization constant $A_{m,p}$ is equal to $\sqrt{\frac{2^{|m|+1}p!}{\pi w(z)^2\,(p+|m|)!}}$. In the expression of LG modes, λ is the wavelength of the radiation, $w(z) = w_0\sqrt{1+(z/z_R)^2}$, $R(z) = z\left[1+(z/z_R)^2\right]$ and $z_R = \pi w_0^2/\lambda$ are the beam radius, wavefront curvature radius and Rayleigh range, respectively, w_0 being the radius at the beam waist [12]. $L_p^{|m|}(x)$ are the generalized Laguerre polynomials. Introducing dimensionless coordinates $\rho = r/w_0$ and $\zeta = z/z_R$, these modes are given by

$$\mathrm{LG}_{p,m} = A_{p,m} \left(\frac{\rho}{\sqrt{1+\zeta^2}}\right)^{|m|} e^{-\frac{\rho^2}{1+\zeta^2}} L_p^{|m|}\left(\frac{2\rho^2}{1+\zeta^2}\right) e^{\left(\frac{i\pi\rho^2}{\zeta}\right)}\, e^{im\phi}\, e^{-i(2p+|m|+1)\arctan(\zeta)}. \tag{1.43}$$

The positive integer p and the integer m are the two indices defining a LG mode, with m being its OAM content. In Fig. 1.6 we report some example of intensity and phase distribution for LG modes. As a final remark, we observe that these modes are

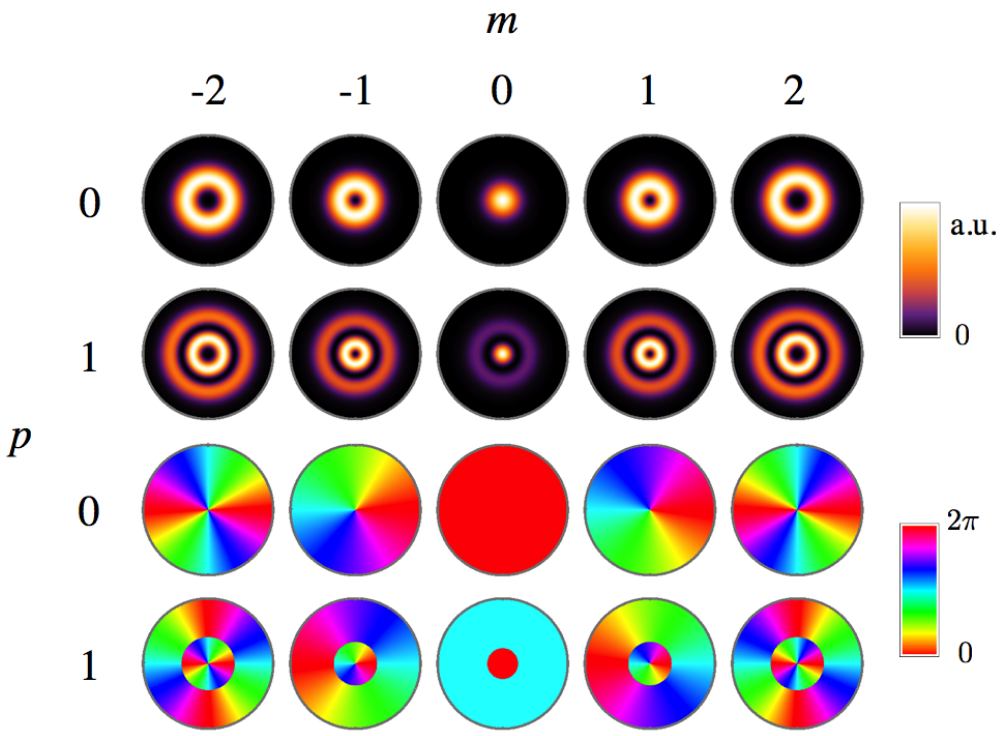

FIGURE 1.6: Intensity and phase pattern of Laguerre-Gauss beams. From these plots it is clear that the index p determines the presence of multiple rings. The zero intensity rings correspond to the distances where the Laguerre polynomials vanish and change their sign. This is clearly visible in the phase plots, where we can see that these rings are marked by a π jump.

orthonormal, i.e.

$$\int dx\, dy\, LG^{*}_{p,m}\, LG_{p',m'} = \delta_{m,m'}\delta_{p,p'} \tag{1.44}$$

1.5 The Spin-Orbit space

Paraxial e.m. waves are characterized by physical quantities which can be measured experimentally. This is the case for the projections of the wave-vector $\vec{\mathbf{k}}$, of the OAM and the SAM along the propagation axes, and the radial distribution of the field in the transverse plane. States carrying a well defined value for each of these quantities, i.e. the eigenstates of the associated operators, represent a complete set for the description of the state of a generic paraxial light beam. In other words, the field can be written as

$$E(r,\varphi,z,t) = E_0 \int_{-\infty}^{\infty} dk \sum_{j=L,R} \sum_{p=0}^{\infty} \sum_{m=-\infty}^{\infty} c_{j,m,p}(k)\, e^{-i(\omega t - kz)}\, |j,m,p\rangle \tag{1.45}$$

where the Dirac ket $|L, m, p\rangle$ ($|R, m, p\rangle$) represents Left (Right)-circularly polarized light with spatial distribution given by the Laguerre-Gauss mode $LG_{p,m}$. In the context of this work we will be mostly interested in the state of the radiation associated with the SAM and OAM degrees of freedom, which we describe through the SAM and OAM spaces ($\mathcal{H}_\pi$, $\mathcal{H}_o$), respectively. Assuming fixed the values of both k_z (the wavelength) and p (radial distribution of field), we consider the state of a light beam in the spin-orbit space. The latter, labeled as $\mathcal{H}$, is given by the direct product of SAM and OAM subspaces

$$\mathcal{H} = \mathcal{H}_\pi \otimes \mathcal{H}_o \tag{1.46}$$

and is spanned by the basis vectors

$$|j, m\rangle = |j\rangle_\pi \otimes |m\rangle_o, \tag{1.47}$$

with $j \in \{L, R\}$ and $m \in \mathbb{Z}$. Neglecting the dependance through the radial and longitudinal coordinates (r, z), the generic electric field will be represented as

$$|E\rangle = \sum_{j=L,R} \sum_{m=-\infty}^{\infty} c_{j,m} |j, m\rangle. \tag{1.48}$$

We can observe from the latter equation that for an arbitrary e.m. wave the global state of the field cannot be written as a product of a polarization term and an amplitude envelope, as it was done for pedagogical reasons to introduce the concepts of SAM and OAM (see Eq. 1.20):

$$|E\rangle \neq |E\rangle_\pi \otimes |E\rangle_o. \tag{1.49}$$

In a classical picture, this means that in the transverse plane the polarization state of the electric field is not uniform but depends on the coordinates (r, φ). This concept is deeply discussed in Ch. 2 (see for instance Fig. 2.2). When Eq. 1.48 describes the state of a single photon, there is "entanglement" between the two degrees of freedom of SAM and OAM. Since regarding two observable quantities of the same particle, and not a single property for two distant partners (mathematically, the two configurations are identical), this is sometimes referred to as "classical entanglement" [13]. The generation of controlled entanglement between SAM and OAM is the subject of Ch. 3.

The notation we have introduced allows one to describe the state of a paraxial light beam, with a particular focus on its SAM and OAM content; the same notation can be used for a physical system made of a single photon as well, but may not be appropriate

if considering multi-particles states. In this case, it is worth to use the formalism of the Quantum Field Theory, where $\vec{\mathbf{E}}$ is a quantum operator expressed in terms of creation and annihilation operators acting on the Fock space of single photons. Considering only the spin-orbit space, such quantum field can be written as

$$\widehat{E} = \sum_j \sum_m \widehat{a}_{j,m}\, \hat{\mathbf{e}}_j\, e^{im\varphi}\, e^{-i\omega t} + \text{H.C.} \tag{1.50}$$

where H.C. stands for the hermitian conjugation and $(\widehat{a}_{j,m}, \widehat{a}^{\dagger}_{j,m})$ are the annihilation and creation operators for a bosonic particle, respectively, associated with the spin-orbit mode $|j\rangle_\pi \otimes |m\rangle_o$. They act on the Fock space, spanned by vectors $|n_{j,m}\rangle$, representing a state with n photons in the mode $|j,m\rangle$; here n is a positive integer. The formalism of the Fock space, introduced here for completeness, will be used only in Ch. 5 when describing an experiment involving a system made of two photons.

1.6 Devices and techniques for controlling and measuring SAM and OAM

The preparation and the characterization of spin-orbit states of light rely on specific devices which allow for controlling the two degrees of freedom in a optical beam. Given the field as expressed in Eq. 1.48, this consists in the possibility of setting the initial values of coefficients $c_{j,m}$, changing them with a controlled dynamics, and measuring their value. In this section we introduce the instruments and the associated techniques to manipulate and measure SAM and OAM separately. Given the relevance for the research work described here, we will devote a separate section to the description of the q-plate, the device we exploit to engineer a spin-orbit coupling in the light beam.

1.6.1 Waveplates and polarizers

The control of the SAM state of a light beam is realized through wave plates and polarizers; since these are common tools in every optics laboratory, we will introduce them very briefly. In general, a polarizer is a slab of a material which, when crossed by a light beam, allows only a specific linear polarization to pass, absorbing or reflecting the other component. Considering for simplicity this allowed polarization as the horizontal one, such polarizer will be represented by the operator

$$\widehat{P}_H = |H\rangle\langle H| = \begin{pmatrix} 1 & 0 \\ 0 & 0 \end{pmatrix} \tag{1.51}$$

When rotated in the transverse plane, a polarizer gives the opportunity to generate any linear polarization.
A wave-plate is a thin layer of a birefringent material. Considering this oriented in order that $\hat{\mathbf{e}}_x$ and $\hat{\mathbf{e}}_y$ are two of its optic axes, the device effect results in a phase shift between the horizontal and vertical components of the field (neglecting a global phase factor)

$$\widehat{WP} = \begin{pmatrix} e^{-i\delta/2} & 0 \\ 0 & e^{i\delta/2} \end{pmatrix} \tag{1.52}$$

where δ depends on the thickness of the plate, the wavelength of the radiation, and the difference between the refractive indices relative to the two axes. Two cases are of particular interest: we refer to these devices as quarter-wave plates (QWP) or half-wave plates (HWP) when $\delta = \pi/2$ and $\delta = \pi$, respectively. Orienting suitably a set of wave plates it is possible to implement any unitary transformation in the SAM space $\mathcal{H}_\pi$; the general expression of the associated Jones matrices is given in Appendix A. Combining QWPs and HWPs with a polarizer allows for the preparation and detection of any polarization state.

1.6.2 Holography to prepare and detect OAM modes

The common strategy to prepare a light beam in a OAM mode is to engineer a device which converts the fundamental Gaussian mode, generated from the laser source, in a beam with the helical phase $e^{im\varphi}$. The simplest approach would be introducing the desired phase delay through a slab of transparent material with a non uniform thickness $d(\varphi) = m\lambda\varphi/2\pi n$, where n is the material refractive index; such device is called Spiral Phase Plate (SPP). Though simple, a SPP has the drawback of requiring precise control on manufacturing the material at very small length scales, less than a micron for optical wavelengths and standard refractive media.
The widest used technique to generate helical modes is holography. The latter allows one to generate any optical field after shining a device called hologram with a suitable reference beam [10]. In order to achieve this result, the interference pattern of a reference beam and the desired optical field is recorded or computed, and reported on the hologram. After the reference beam impinges on such hologram, which modulates its phase and amplitude, the optical field is obtained. In the past, holograms were built recording the interference pattern on a suitable material, as a photographic paper; nowadays they are conveniently generated through a computer.

We are interested in generating OAM modes $|m\rangle$, which we assume here to be plane waves with the factor $e^{im\varphi}$. In Fig. 1.7 we report the interference pattern of a reference

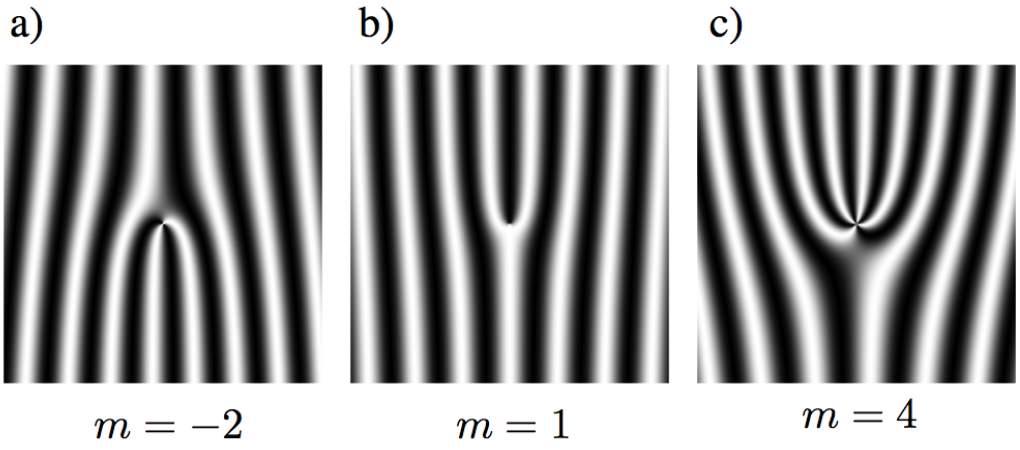

FIGURE 1.7: Light intensity in the (x,y) plane of a superposition of a plane wave, propagating along z, and a helical mode $|m\rangle$, whose propagation direction lies in the (x,z) plane. In the picture, we are assuming x and y axes to correspond to the horizontal and vertical directions, respectively. Light intensity is encoded in the gray-level scale. As a result of the interference, the typical pitchfork pattern appear. The difference between the number of fringes of the upper and lower part of the figure is equal to the OAM of the mode $|m\rangle$.

plane wave e^{ikz} and an helical mode $|m\rangle$ with the same wavelength, propagating in the (x, z) plane; the standard sinusoidal modulation, due to the different propagation directions, is modified in a fork-like shape. Pitch-fork holograms we use for the generation of helical modes are phase holograms acting on the impinging beam introducing a phase $\phi(x, y)$. In order to convert the reference plane wave into a mode of order m, we engineer this phase as

$$\phi = B(k_x x + m\varphi) \tag{1.53}$$

where $B(t)$ is the blazed function $B(t) = \mathrm{Mod}(t, 2\pi)$, and $1/k_x$ defines the period of B along the x direction. Considering the hologram positioned in $z = 0$, at the exit of the latter the field will be in the state

$$E = e^{iB(t)} = \sum_{m'=-\infty}^{\infty} c'_m \, e^{im't} = \sum_{m'=-\infty}^{\infty} c'_m \, e^{im'(k_x x - m\varphi)} \tag{1.54}$$

where we have expanded the periodic function $B(t)$ in a Fourier series. In case of blazing periodicity, it is straightforward to prove that c_1 is the only non-vanishing coefficient in the Fourier decomposition (1.54). At the exit of the hologram the beam is totally converted in the mode $|m\rangle$, and propagates along the first diffraction order corresponding to the direction $\theta_1 = \arctan k_x/k$. A scheme of the introduced protocol is represented

in Fig. 1.8. It is important to observe that the state $|m\rangle$ prepared exploiting pitchfork holograms does not correspond to the Laguerre Gauss mode $\mathrm{LG}_{0,m}$; indeed the prepared state, that is $\mathrm{LG}_{0,0}\, e^{im\varphi}$, is a superposition of LG beams with different p

$$\mathrm{LG}_{0,0}\, e^{im\varphi} = \sum_{p=0}^{\infty} c_p^m\, \mathrm{LG}_{p,m} \tag{1.55}$$

Given the generic state in the OAM space, described by Eq. 1.40, it is important to

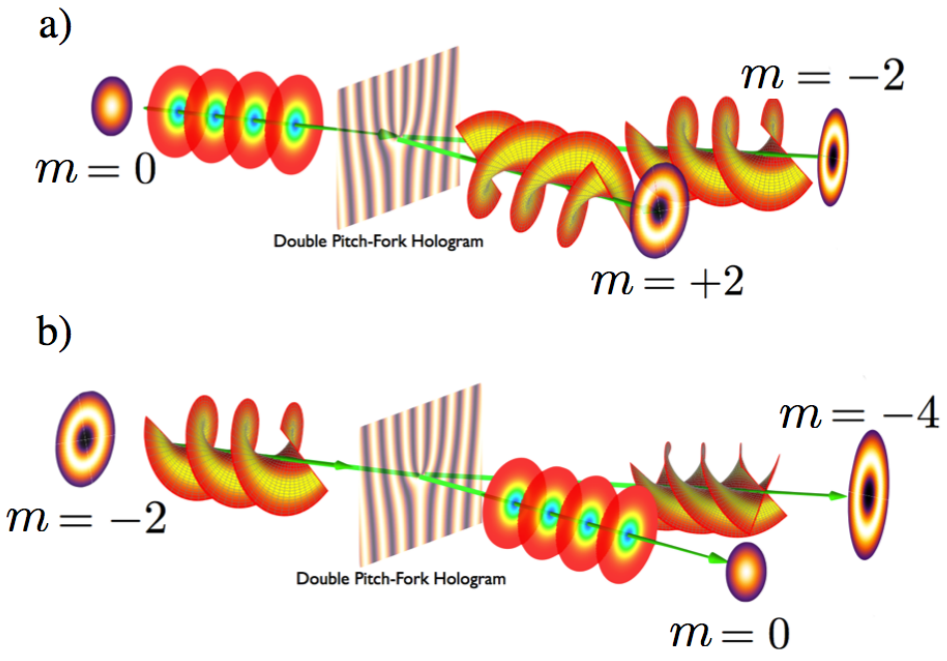

FIGURE 1.8: Generation and detection of helical modes using pitch-fork holograms.

determine the intensity associated with each helical mode $|m\rangle_o$, that is the value $|c_m|^2$. This is possible combining the introduced holographic technique with a device which acts as a mode filter (the analog of a polarizer for the SAM space). A standard choice is to use Single Mode Optical Fibers (SMF); when light is injected into the fiber, total internal reflection allows the radiation to propagate with low losses only if the spatial mode is that of an approximately Gaussian beam. We are making the assumption that the beam waist w_0 and the radius of the internal part of the fiber are matched. The measurement of the intensity associated with a specific helical mode $|m\rangle$ in a complex light beam can be thus performed using an hologram of order $-m$, which converts only the helical state $|m\rangle$ into a Gaussian mode. The emerging light, propagating along the first diffraction order, is then coupled into a SMF; at the exit of the latter, the intensity

of the radiation is proportional to $|c_m|^2$.
Computer-Generated-Holograms (CGH) can be used to generate and detect not only helical modes, but any spatial distribution of the field in the transverse plane. We will discuss this generalized technique in Ch. 4.

1.7 Spin-Orbit interaction: the q-plate

The precise control of the polarization of an optical beam can be achieved exploiting the birefringence in anisotropic materials; at the same time, the spatial distribution of the field can be modulated through non-uniform media, such as an hologram. The combination of these properties in a material whose anisotropy is not homogeneous gives rise to spin-orbit coupling in a light beam. Relying on this concept, a photonic device called q-plate allows the generation of helical modes whose OAM content is conditioned by the polarization. It consists of a slab of uniaxial liquid crystal material (LC) whose optic axes are arranged to form a non-uniform pattern in the transverse plane. As for standard wave plates, in a light beam crossing a LC cell the components of the field associated with the fast and slow axes suffer a phase delay δ; the latter depends on the thickness of the plate, the wavelength of the radiation, the ordinary and extraordinary refractive indices of LCs and the orientation of the optic axes of the molecules with respect to the propagation direction. In a q-plate the thickness of the cell and longitudinal orientation of the molecules are homogeneous, so as to have a uniform δ. For the generation of a pure OAM mode, this value has to be equal to π (HWP configuration); the action of a HWP on circularly polarized light is simple:

$$\begin{aligned} \widehat{HWP} \cdot |L\rangle_\pi &= |R\rangle_\pi \, e^{i2\alpha} \\ \widehat{HWP} \cdot |R\rangle_\pi &= |L\rangle_\pi \, e^{-i2\alpha} \end{aligned} \tag{1.56}$$

where we have supposed the HWP rotated around the z axis of an angle α. In a q-plate, α is arranged in a singular pattern, whose expression is given by

$$\alpha(x, y) = q\varphi + \alpha_0 \tag{1.57}$$

where α_0 is the angle at $\varphi = 0$ and the integer or half integer number q is called topological charge. The fast axis orientation is singular at the origin, while in a closed loop around this point it rotates by an angle equal to $2q\pi$ (see Fig. 1.9). Combining Eq. 1.56 and Eq. 1.57 we can observe that a circularly polarized plane wave crossing a q-plate is converted in a helical mode of order $\pm m$, with the OAM sign depending on

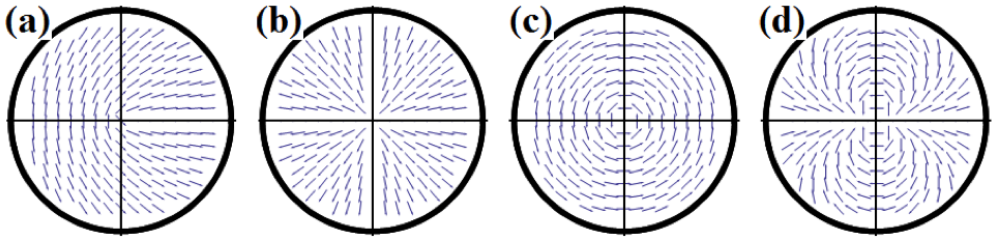

FIGURE 1.9: Arrangement of the optical axes in a q-plate. Panels a) - d) refer to the following cases: a) $(q = 1/2, \alpha_0 = 0)$, b) $(q = 1, \alpha_0 = 0)$, c) $(q = 1, \alpha_0 = \pi/2)$, d) $(q = 2, \alpha_0 = 0)$. This picture is adapted from Ref. [14].

the handedness of the initial polarization (see Fig. 1.10);

$$\begin{aligned} \widehat{QP}_{\delta=\pi} \cdot |L, 0\rangle &= |R, 2q\rangle \, e^{i2\alpha_0} \\ \widehat{QP}_{\delta=\pi} \cdot |R, 0\rangle &= |L, -2q\rangle \, e^{-i2\alpha_0} \end{aligned} \tag{1.58}$$

When the input beam is in a superposition of circular polarizations, the output state will

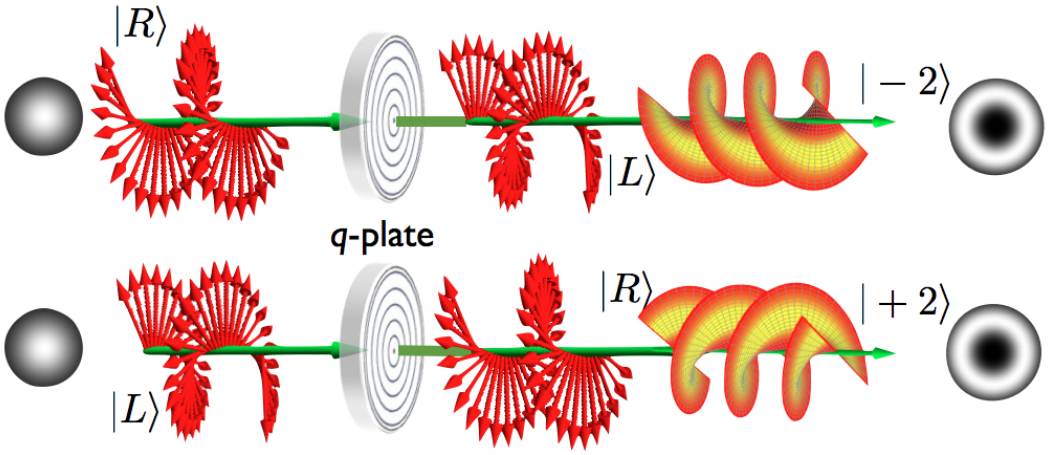

FIGURE 1.10: Generation of helical modes using a q-plate. Picture adapted from the Wikipedia page "Angular momentum of light".

not be separable into the product of SAM and OAM independent terms. Consider for example a horizontally polarized beam; since in the circular basis $|H\rangle = 1/\sqrt{2}(|L\rangle + |R\rangle)$, after the q-plate the field will be in the spin-orbit state (we set $\alpha_0 = 0$ for simplicity)

$$\widehat{QP}_{\delta=\pi} \cdot |H, 0\rangle = \frac{1}{\sqrt{2}} \left(|R, 2q\rangle + |L, -2q\rangle \right). \tag{1.59}$$

Changing the value of q and controlling the polarization of the input beam it is possible to engineer complex structures in the optical field.

To conclude, we consider the general case where the phase retardation δ can take any

value in the range $(0, 2\pi)$. As demonstrated in Appendix A, the action of the q-plate is expressed as follows

$$\begin{aligned}\widehat{QP}_\delta \cdot |L, m_0\rangle &= \cos(\delta/2)|L, m_0\rangle + i\, \sin(\delta/2)\, e^{-i2\alpha_0}|R, m_0 + 2q\rangle, \\ \widehat{QP}_\delta \cdot |R, m_0\rangle &= \cos(\delta/2)|R, m_0\rangle + i\, \sin(\delta/2)\, e^{i2\alpha_0}|L, m_0 - 2q\rangle,\end{aligned} \tag{1.60}$$

where we have considered as input state not only a plane wave but a general OAM eigenstate $|m_0\rangle$. The result expressed in Eq. 1.60 can be interpreted as follows: a part of the incoming field, proportional to $\cos(\delta/2)$, is left unchanged; we refer to this as the "unconverted" component of the beam. In the "converted" term, proportional to $\sin(\delta/2)$, the OAM is raised or lowered by $2q$ according to the handedness of the input polarization. The value of the retardation δ can be finely tuned through an external electric field applied to the faces of the plate [15], or by controlling its temperature [16]. In Fig. 1.11 we report the data of the experimental measurements of δ of a q-plate when varying the applied voltage. This simple procedure allows one to adjust the plate retardation in a broad range of wavelengths, getting the value of δ suitable for the purpose of the experiment.

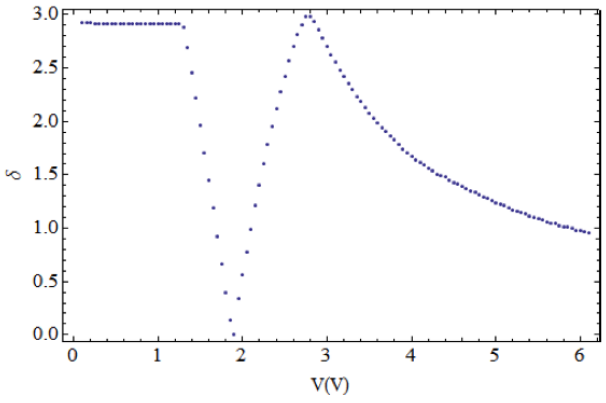

FIGURE 1.11: Tuning the q-plate retardation δ applying an external electric field. The figure is adapted from [17], Fig. 3.13.

Chapter 2

Vector beams and polarization singularities

2.1 Introduction

A q-plate alters the polarization and the spatial distribution of a light beam, so as to give rise to an e.m. wave where the field in general is not uniform in the transverse plane, both in amplitude and direction. These beams are usually called Vector Beams (VB) or, when showing a cylindrical symmetry [18], Cylindrical Vector Beams (CVB). VBs are particular solutions of the paraxial limit of vectorial Maxwell's equations and have intriguing properties. The field geometry in the transverse plane can have a non trivial topology, associated with singularities in the polarization degree of freedom, such as C-points and L-lines, or in the phase distribution. In the context of polarization singularities, C-points and L-lines correspond to spatial regions where the orientation or the ellipticity of the polarization ellipse are not defined, respectively [19–21]. The first case corresponds to circular polarization states, the second to linear polarizations. Vector Beams are also referred to as Vector Vortex Beams (VVB) when they present phase singularities associated with zero-intensity points, as for standard helical modes. Among these, beams whose polarization pattern have a radial or an azimuthal distribution have unique features when sharply focused [22], and represent an example of field structure which is invariant with respect to rotations around the propagation axis. In the last decade CVBs have been exploited for a variety of different applications, such as for instance single molecule imaging [23], particle acceleration [24], Raman spectroscopy [25], particle trapping [26], material surface structuring [27, 28], alignment-free quantum communication [29, 30]. Recently, a Möebius strip has been observed in the polarization

structure of a specific VB [31]. Various approaches have been developed for the generation of such e.m. waves; active methods rely on modifying the laser sources (the cavity, the crystal,...) generating CVBs as output mode [32–34]. On the other hand, passive methods exploit optical devices to convert a Gaussian beam into a vectorial one [35–38]. In this chapter we discuss an experimental technique we developed to generate and characterize CVBs using a q-plate, tailoring dynamically the beam features by suitable control of the polarization of the input beam and the LCs phase retardation δ. Thus we generated radial and azimuthal polarizations [39], as well as other geometries for the field in the transverse plane, including the fundamental polarization singularities [40]. The proposed approach presents several advantages; it is simple, since it relies entirely on the spin-orbit coupling operated by the q-plate on a uniformly polarized Gaussian beam. The whole process occurs in a single light beam, differently from interferometric schemes where the field components are manipulated separately and then recombined. Finally, this method allows for fast switching in the generation of different CVBs, which can be obtained preparing suitably the polarization state of the input beam.

2.2 Vector Beams

Vector Beams are paraxial e.m. waves whose field components have a different spatial distribution, in any polarization basis. Referring to the circular basis, we can express the field as:

$$E = \begin{pmatrix} c_L\, u_L(r,\varphi,z) \\ c_R\, u_R(r,\varphi,z) \end{pmatrix} \tag{2.1}$$

In a VB u_L and u_R are different solutions of the paraxial wave equation, which can be represented conveniently as a sum of LG modes. As a simple and illustrative case we consider (u_L, u_R) to be a superposition of only two helical modes, corresponding to $\mathrm{LG}_{0,m}$ and $\mathrm{LG}_{0,-m}$. Linear combinations of these two modes form a 2-dimensional (2D) Hilbert space $\mathcal{H}_o^m$; when combined with the polarization degree of freedom, the direct product of the SAM space $\mathcal{H}_\pi$ and the OAM subspace $\mathcal{H}_o^m$ give rise to a four-dimensional space $\mathcal{H}_4^m$, generated by the states $\{|L,m\rangle, |L,-m\rangle, |R,m\rangle, |R,-m\rangle\}$ [41, 42]. This can be decomposed into the direct sum of two subspaces $\mathcal{S}_m$ and $\mathcal{S}_{-m}$, generated by vectors $\{|L,-m\rangle, |R,m\rangle\}$ and $\{|L,m\rangle, |R,-m\rangle\}$, respectively

$$\mathcal{H}_4^m = \mathcal{S}_m \oplus \mathcal{S}_{-m} \tag{2.2}$$

This decomposition is motivated by the different topological properties of the states forming these two spaces, represented in Fig. 2.2 in terms of the associated Poincaré

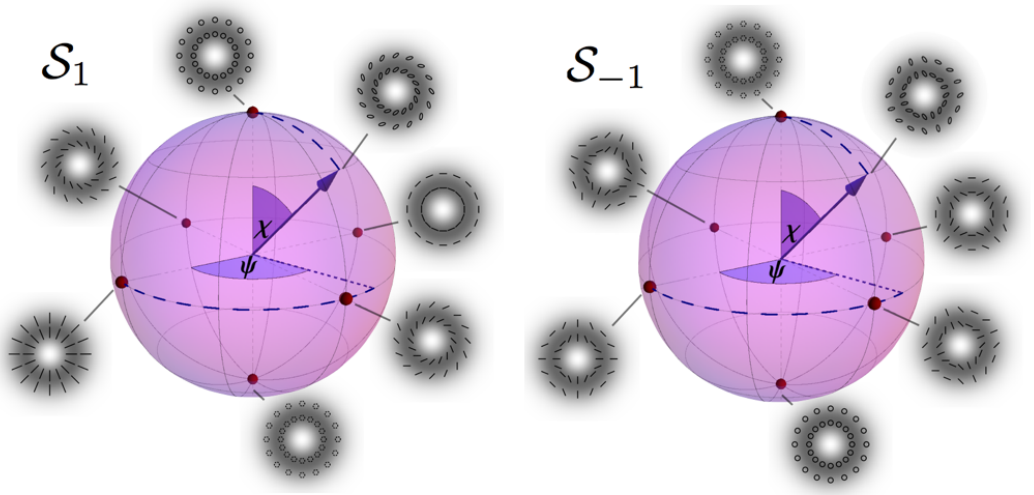

FIGURE 2.1: Poincaré spheres representation of the hybrid spaces $\mathcal{S}_1$ and $\mathcal{S}_{-1}$. On the equator we find states where the polarization is linear in every point of the transverse plane, while at the poles we have uniformly circularly polarized states. Generic points on the spheres have elliptical polarizations, whose major axis is arranged in a topological structure a) The $\mathcal{S}_1$ space contains states with topological charge $\eta = 1$; in particular, their polarization is invariant respect to rotation around the propagation axis. b) The $\mathcal{S}_{-1}$ space has states with $\eta = -1$.

spheres (we report the simplest case $m = 1$). In any plane transverse to the propagation direction, all beams in $\mathcal{H}_4^m$ have a singular point located on the optical axis. The field vanishes at these points, as a consequence of the phase singularity affecting both left and right circular components. A topological charge η can be associated with the polarization pattern around the singular points; it is equal to the number of full rotations of the orientation of the field, when following a closed trajectory around the singularity. As orientation we are considering the direction of the major axis of the polarization ellipses. It is clear form both Fig. 2.1 and Fig. 2.2 that states in $\mathcal{S}_m$ and $\mathcal{S}_{-m}$ have $\eta = m$ and $\eta = -m$, respectively. In particuar, in Fig. 2.2 we can observe that when $m > 1$, the direction of the electric field is arranged in pictorial patterns; states with positive charge have a structure similar to that of petals in a flower; the electric field orientation forms spider webs instead in negatively charged optical beams [43]. The complexity of VBs increases when considering envelopes u_L and u_R with a more complicated spatial dependance, as for example including the radial degree of freedom; nevertheless, this possibility will not be considered here. We will discuss below only the relevant case where one of the two polarization components is in the fundamental Gaussian mode, as this introduces C and L singular points in the field (see Sec. 2.4).

States in the subspace $\mathcal{S}_1$ have a particular simmetry, since a rotation around the propagation axis leaves unchanged their polarization distribution. We can recognize this feature in the few patterns reported in the $\mathcal{S}_1$ Poincaré sphere in Fig. 2.1. This

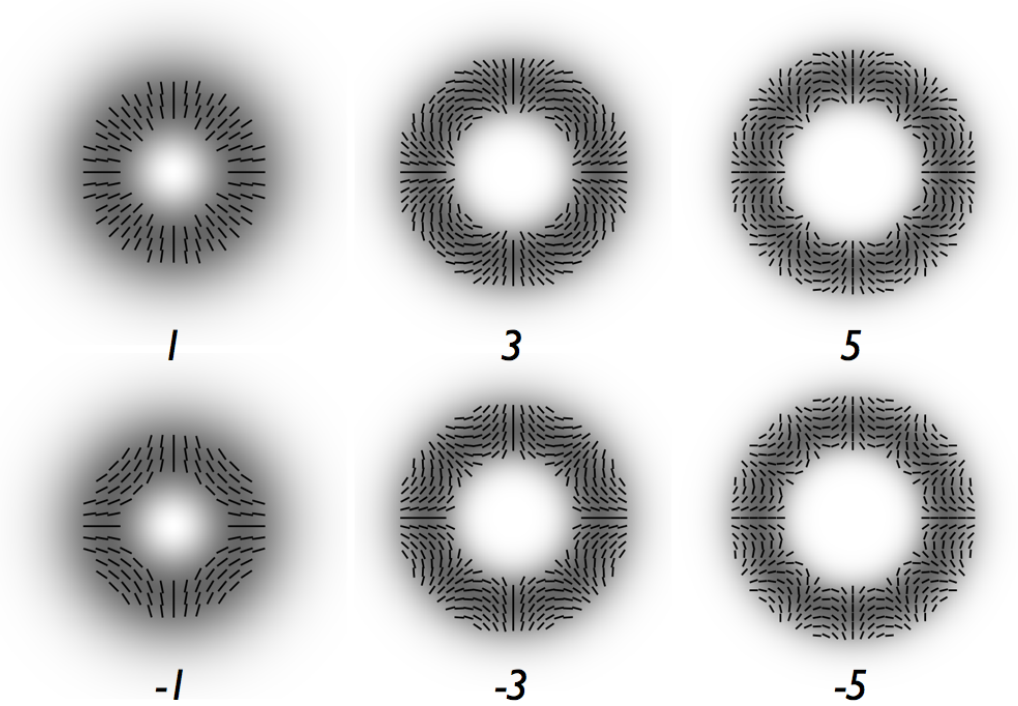

FIGURE 2.2: Polarization pattern corresponding to the state $1/\sqrt{2}(|L,m\rangle + |R,-m\rangle)$, for different values of m corresponding to positive and negative topological charges. When increasing the order of the helical modes, the orientation of polarization ellipses varies faster along the azimuthal coordinate.

result can be demonstrated by noticing that the effect of the rotation on the $\mathcal{H}_\pi$ and $\mathcal{H}_o$ basis states results in the introduction of a phase factor proportional to the rotation angle α:

$$\begin{pmatrix} |L\rangle \\ |R\rangle \end{pmatrix} \rightarrow \begin{pmatrix} e^{+i\alpha}|L\rangle \\ e^{-i\alpha}|R\rangle \end{pmatrix}, \qquad |m\rangle \rightarrow e^{im\alpha}. \tag{2.3}$$

Choosing $m = \pm 1$, opposite phase factors cancel each other in the product states $|L,-1\rangle$ and $|R,1\rangle$. This symmetry has been exploited to demonstrate a quantum communication protocol where the invariant states are used to encode a bit of quantum information; as a striking difference with respect to standard photonic protocols, the sender and the receiver do not need to align their transverse axis [29]. Two important examples of rotational invariant states are the azimuthal and radial polarizations, here referred to

as $|r\rangle$ and $|\phi\rangle$, respectively. Their expression is

$$|r\rangle = \frac{1}{\sqrt{2}}\left(|L,-1\rangle + |R,1\rangle\right) \tag{2.4}$$

$$|\phi\rangle = \frac{1}{\sqrt{2}}\left(|L,-1\rangle - |R,1\rangle\right) \tag{2.5}$$

As all other linearly polarized states, they lie on the equator of the $\mathcal{S}_1$ Poincaré sphere, in points $(\theta,\phi) = (\pi/2, 0)$ and $(\pi/2, \pi)$, respectively. Using a single q-plate it is possible to generate these beams in a very simple experimental architecture [39].

2.3 A q-plate to generate Vector Beams [1]

A combination of wave plates and a single q-plate allows to generate all VBs in the 4-dimensional space $\mathcal{H}_4^m = \mathcal{H}_\pi \otimes \mathcal{H}_o^m$ introduced in the previous section. Consider a light beam whose polarization has been prepared in the state $|\theta,\phi\rangle_\pi$, corresponding to the point (θ,ϕ) on the SAM Poincaré sphere. According to Eq. 1.58, after passing through a q-plate with $\delta = \pi$ the global spin-orbit state is

$$\begin{aligned}\widehat{Q}_{\delta=\pi}\cdot\left[\cos\left(\frac{\theta}{2}\right)|L,0\rangle + \sin\left(\frac{\theta}{2}\right)e^{-i\phi}\,|R,0\rangle\right] = \\ = \cos\left(\frac{\theta}{2}\right)|R,2q\rangle + \sin\left(\frac{\theta}{2}\right)e^{-i\phi}\,|L,-2q\rangle\end{aligned} \tag{2.6}$$

where we have considered the plate orientation to be α_0=0. The state reported in the last term of Eq. 2.6 is a CVB belonging to $\mathcal{S}_{\pm m}$, with $m = 2q$. The q-plate introduces a one to one correspondence between $\mathcal{H}_\pi$ and $\mathcal{S}_{\pm 2q}$; in particular, every point (θ,ϕ) on the SAM sphere is mapped into the same point of the corresponding $\mathcal{S}_{2q}$ Poincaré sphere. Without changing the q-plate, states in $\mathcal{S}_{-2q}$ can be obtained adding a HWP at the end of the system, which simply transforms left into right circular polarization, and vice-versa. In the experiment we are describing in this section, we used q-plates with $q = 1/2$ and $q = 1$ to generate VBs, in particular radial and azimuthal polarizations. To confirm the generation of such states, we measured the polarization pattern of the final beam, and compared it to the theoretical predictions.

The experimental setup is described in Fig. 2.3. A 10mW average power Helium-Neon laser beam at $\lambda = 632.8$nm, in the TEM_{00} spatial mode, was spatially cleaned by focusing into a $50\mu m$ pinhole followed by a truncated lens placed at a distance equal to its focal length. This procedure allows one to have a collimated beam with a uniform intensity. A linear polarizer was used to have $|H\rangle_\pi$ as the initial SAM state; after

[1] Some paragraphs and sentences of this section are adapted or copied verbatim from the work [39] which I coauthored.

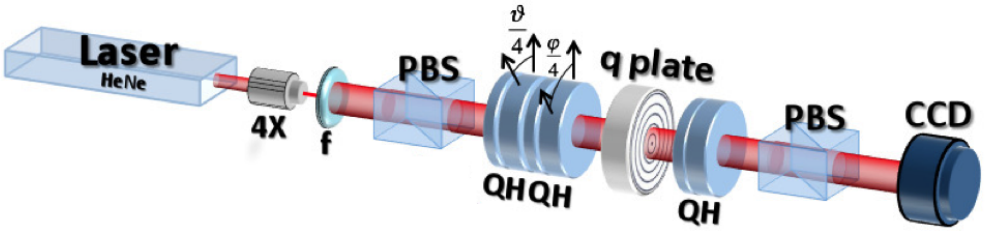

FIGURE 2.3: Experimental setup [39] . Setup to generate and analyze different polarization topologies generated by a q-plate. The polarization state of the input laser beam was prepared by rotating the two half-wave plates in the QHQH set at angles $\vartheta/4$ and $\varphi/4$ to produce a corresponding rotation of (ϑ, φ) on the Poincaré sphere. A combination of wave plates and a polarizer is used for polarization analysis through projections on the states (R, L, H, V, A, D). For each state projection, the intensity pattern was recorded by CCD camera and the signals were analyzed pixel-by-pixel to reconstruct the polarization pattern in the beam transverse plane. Legend: 4X - microscope objective of 4X used to clean the laser mode, f - lens, Q - quarter wave plate, H - half wave plate, PBS-polarizing beam-splitter.

that, the state $|\theta, \phi\rangle_\pi$ is obtained through a sequence of wave plates. The beam was then sent into an electrically tuned q-plate, which generated a non-separable spin-orbit state as given by Eq. 2.6. The external electric field applied to the plate was adjusted to have optical retardation $\delta = \pi$. The output beam was analyzed by point-to-point polarization tomography; the polarization components relative to the bases (H, V), (A, D) and (L, R) are analyzed by combining a QWP-HWP set and a linear polarizer. The associated intensities are recorded at each pixel of a CCD camera (Sony AS-638CL), whose sensor resolution is 120×120; the beam size has been adjusted so as to efficiently exploit the CCD area. Examples of the recorded intensity profiles are shown in Fig. 2.4; it can be noted that in the case of a VB (panels a) and c)), the intensities of the different components of the field have a different spatial distribution. The polarization distribution in the beam transverse plane is reconstructed trough a suitable algorithm implemented using the software *Mathematica*, by Stephen Wolfram. For every pixel (i, j), the Stokes parameters are computed in terms of the intensities $I_H(i, j)$, $I_V(i, j)$, $I_A(i, j)$, $I_D(i, j)$, $I_L(i, j)$ and $I_R(i, j)$. When rotating the wave plates to project the polarization on different basis, the beam direction may undergo a tiny alteration. To minimize the error due to this effect, the values of the measured Stokes parameters were averaged over a grid of 20 × 20 squares equally distributed over the image area. In the first part of the experiment, we shined a q-plate with q=1/2 using a light beam with horizontal, vertical and left-circular polarizations. Applying the transformation introduced in Eq. 2.6, we can note that $|L, 0\rangle$ is turned into the helical mode with

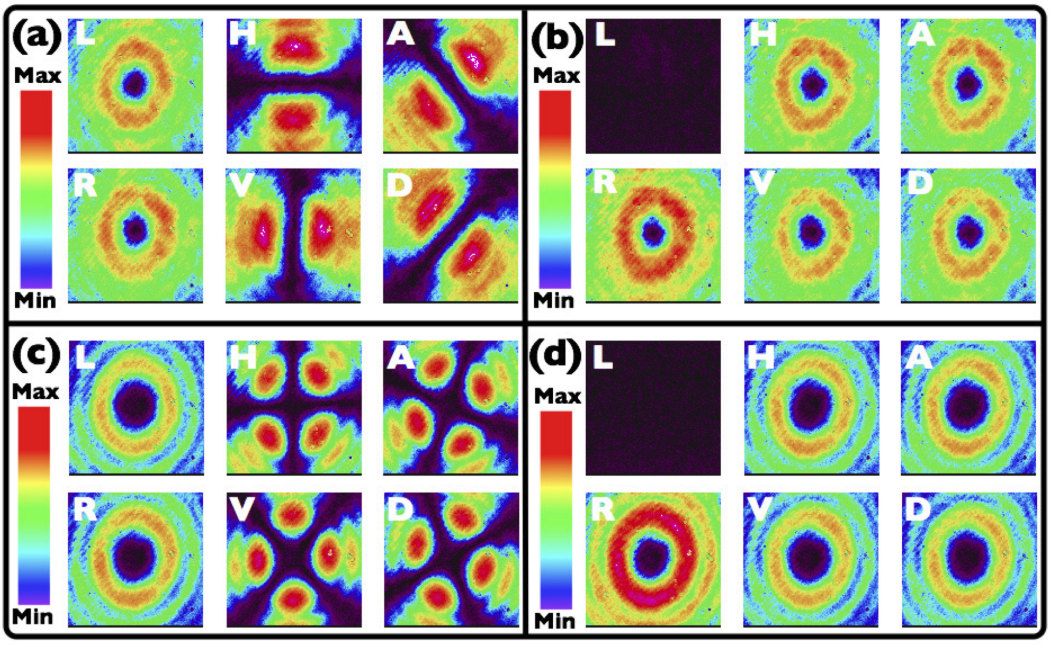

FIGURE 2.4: Intensities of the polarization components as recorded by the CCD camera after projecting over horizontal (H), vertical (V), anti-diagonal (A), diagonal (D), left-circular (L) and right-circular (R) polarization base states for different q-plates and input polarizations [39]. a) and b) are for the $q = 1/2$-plate, and horizontal-linear a) and left-circular b) polarization of the input beam. c) and d) are the same for the $q = 1$-plate. The color scale bar shows the intensity scale (arbitrary units) in false colors.

$m = 1$, with a uniform right-circular polarization. On the other hand, states $|H, 0\rangle$ and $|V, 0\rangle$ are converted into radially and azimuthally polarized beams, respectively. The reconstructed polarization patterns are shown in Fig. 2.5 a), b) and c), respectively. They show a nice agreement with theoretical distributions reported in Fig. 2.1 and 2.2. Similar results are obtained changing the topological charge to $q = 1$. In this case, we obtain VBs with topological charge $\eta = 2$; in Fig. 2.5d) and e), we report the data relative to the case with $|H, 0\rangle$ and $|L, 0\rangle$ as initial states. As discussed previously, the case of $q = 1/2$-plate is particularly interesting since it allows the generation of radial and azimuthal polarizations, obtained when the input state is $|H, 0\rangle$ or $|V, 0\rangle$, respectively. These have a number of applications and can be used to generate uncommon beams such as electric and magnetic needle beams, where the optical field is confined below diffraction limits. We stress the important point that this technique allows one to generate these peculiar states using a single optical element, the q-plate, which converts the input beam by transmission without altering its propagation direction; moreover, it does not need to split the beam and recombine it in a interferometer. In other methods [36–38] the need of stable and precise alignment plays a crucial role.

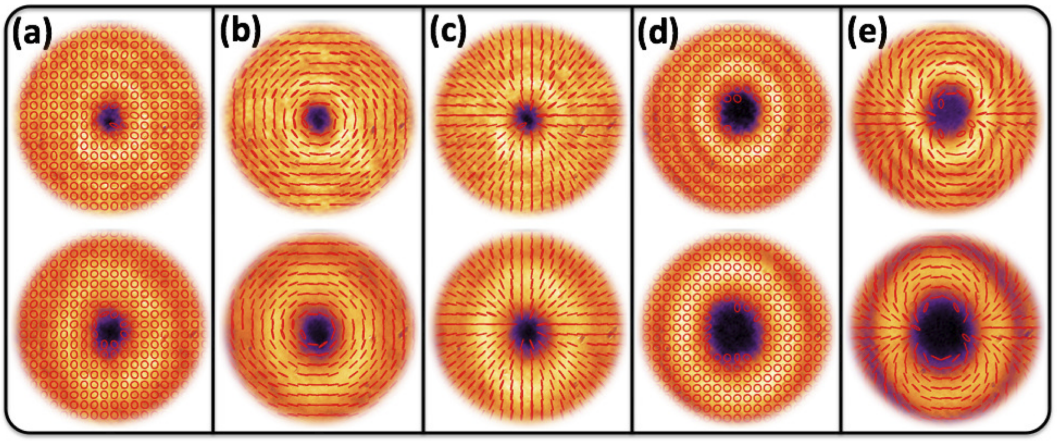

FIGURE 2.5: Reconstructed polarization pattern of vector beams generated by the q-plate [39] . Highest-row panels: the transverse polarization and intensity distribution in the near field at the exit face of the q-plate. Lower panels: the polarization and intensity distributions in the far field beyond the q-plate. a), b), and c): polarization topological structure generated by the $q = 1/2$-plate for left-circular, V-linear, and H-linear input polarizations, respectively. d)-e): polarization topological structure generated by the $q = 1$-plate for left-circular and H-linear input polarizations, respectively. a) and d) have uniform circular polarization distributions.

2.4 Polarization singularities in a optical beam

Vector fields may have complex geometries, showing defects surrounded by patterns with a non-trivial topology. In the case of the e.m. field in a paraxial beam, at any point (x, y) in the transverse plane the vector $\vec{\mathbf{E}}(x, y, t)$ changes in time describing an ellipse, which is singular when it turns into a circle or a line. Indeed for circular and linear polarizations the orientation of this trajectory and its handedness are undefined, respectively [19]. In the transverse plane, light can be circularly polarized in isolated points (C-points), since two conditions have to be satisfied: the two linear components of the field must have equal modulus and their phase difference has to be $\pm\pi/2$. Whereas points with linear polarization are arranged in continuous lines, since it is necessary only to have the two components oscillating in phase [44]. The beam propagation introduces a dynamical evolution of the polarization singularities in the transverse plane, as a consequence of different dynamics characterizing high order spatial modes of light [20, 40, 44, 45]. Such scenario can be even richer when considering partially polarized light; a beautiful example is the polarization distribution of the sunlight scattered by the atmosphere, which presents four singular points near to the sun and anti-sun positions [46].

The classification of polarization singularities in terms of C-points and L-lines applies to all elliptical fields. A valuable example consists in surfaces, where the ellipse associated with the Gaussian curvature degenerates in circles and lines at the so called "umbilic points" and "parabolic lines", respectively (see [44] and references therein for

other physical examples).

Polarization singularities arise from the superposition of e.m. waves with different

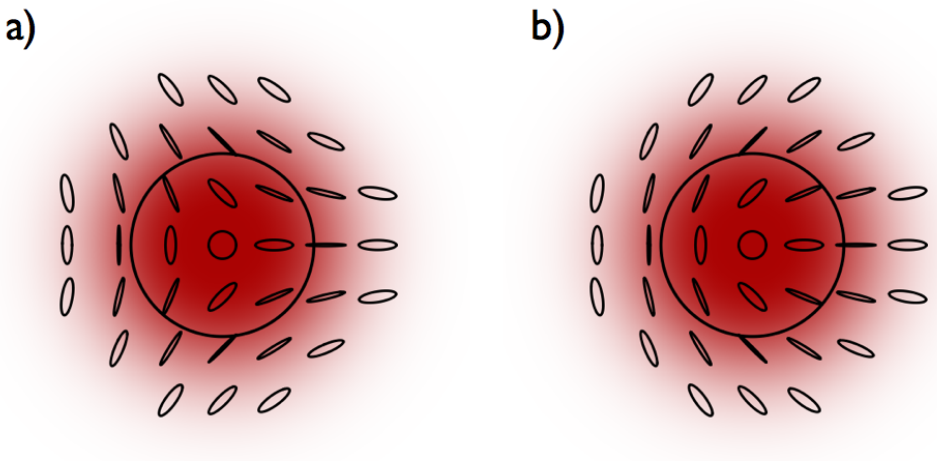

FIGURE 2.6: Polarization pattern of a light beam in the state $|PSB\rangle_{\pm 1}$, obtained in the transverse plane corresponding the beam waist of the LG modes.

polarization and spatial distribution [20, 44]; the structure of the local elliptical field introduces a natural classification of C-points in terms of a topological charge η. As for Vector Vortex Beams, the latter is defined as the number of 2π rotations of the ellipses major axis, when following an anti-clockwise loop around the singular point. The sign of η is positive when the rotation is anti-clockwise as well; being the orientation angle defined modulo π, the fundamental topological charges correspond to $\pm 1/2$. The major axis pattern around C-points with $\eta = \pm 1/2$ is shown in Fig. 2.6; a singularity with $\eta = -1/2$ is called "star", while for $\eta = 1/2$ we have two possibilities corresponding to the same topology. Around the singular point, there can be one or three directions where the ellipses orientation is radial [44]; accordingly, L-lines are called "lemon" or "monstar", respectively (see Fig. 2.7 b), c)).

A simple example of polarization singular beam (PSB) is obtained superimposing the two Laguerre Gauss modes $\mathrm{LG}_{0,0}$ and $\mathrm{LG}_{0,m}$, coupled to orthogonal polarization states. Considering these as circular polarizations, we can express this field as

$$|PSB\rangle_m = c_L\, \hat{\mathbf{e}}_L\, \mathrm{LG}_{0,0} + c_R\, \hat{\mathbf{e}}_R\, \mathrm{LG}_{0,m} \tag{2.7}$$

In Fig. 2.6 we report the polarization pattern of $|PSB\rangle_{\pm}1$, in the case in which $c_L = c_R$. It can be observed that a single C-point is located on the propagation axis, with a topological charge $\eta = \pm 1/2$, corresponding to a star and a lemon, respectively. A single L-line, marked as a continuous black circle, separates the outer and the inner regions characterized by opposite handedness; the latter is a general property of singular polarization patterns [20, 44, 45].

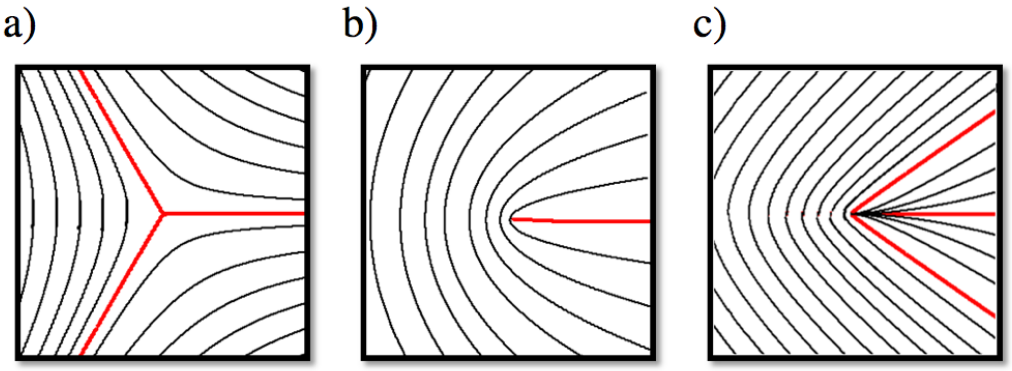

FIGURE 2.7: Comparison of the polarization pattern for the star, lemon and monstar C-points, which are displayed in panels a), b) and c), respectively.

When expressing the field in the circular basis, we can observe that at C-points a component of the field is vanishing; being the latter a scalar quantity, points where it vanishes are phase vortices with a specific topological charge m. The two invariants η and m have to satisfy the simple relation [47]

$$2\eta = m. \tag{2.8}$$

Complex structures with multiple C-points arise when considering larger superpositions

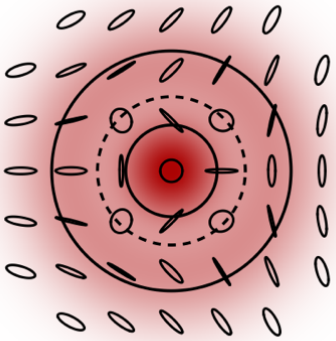

FIGURE 2.8: Poincaré beam showing a double covering of points on the Poincaré sphere in the transverse plane. This pattern corresponds to the state $|PSB\rangle = 1/\sqrt{2}(\hat{\mathbf{e}}_L\,\mathrm{LG}_{0,1} + \hat{\mathbf{e}}_R\,\mathrm{LG}_{1,0})$; as a difference with respect to previous cases, we are exploiting the radial index p.

of higher modes, as naturally occurring for example when a helical beam suffers double refraction in a crystal [45].

The polarization pattern resulting from the state $|PSB\rangle_{\pm 1}$ shows an interesting feature. Indeed it is possible to show that such pattern contains all possible polarization states,

associated with different points on the transverse plane. In particular it has been demonstrated that this mapping consists in the stereographic projection of the Poincaré sphere onto the (x, y) plane [48]. Beams where the polarization pattern is a representation of the whole polarization space are called Poincaré beams (PB). States defined as in Eq. 2.7 with $m = 1$ represent the simplest example of Poincaré beams. When including the possibility of superimposing LG modes with different radial structures we obtain more complex polarization patterns, as reported in Fig. 2.8 where we show a PB with a double covering of the SAM Poincaré sphere[49].

2.5 Generation of polarization singular beams using a tunable q-plate [2]

A q-plate alters the state of a Gaussian and uniformly circularly polarized light beam, which is transformed as follows (Eq. 1.60):

$$\widehat{QP}_\delta \cdot |L, 0\rangle = \cos(\delta/2)|L, 0\rangle - i \sin(\delta/2)\, |R, 2q\rangle \tag{2.9}$$

where we set $\alpha_0 = \pi/2$. The output state coincides with expression 2.7, where $c_L = \cos(\delta/2)$, $c_R = -i \sin(\delta/2)$ and $m = 2q$. Moreover, we are assuming states $|m\rangle_o$ to be LG modes with $p = 0$, even though in the real experiment this is just an approximation. We know indeed that the radial distribution of the field at the output of a q-plate is different with respect to the one of a LG mode with $p = 0$, which anyway represents the dominant contribution in the far field. Nevertheless, this does not alter the azimuthal polarization distribution of the final beam and, as a consequence, the topology of the generated C-points. We will discuss this minor point at the end of this section.

The experiment layout, shown in Fig. 2.9, relies on the same scheme reported in Fig. 2.3, with the addition of a movable stage for the measurement of the polarization pattern evolution along the propagation axis. This kind of analysis was not necessary for the experiment involving vector beams, being their polarization pattern invariant under beam propagation, as explained below. A laser beam generated by a He:Ne source at $\lambda = 632.8$ nm, with 10 mW average power, is spatially cleaned in order to have a Gaussian mode with uniform intensity. By means of a linear polarizer and a QWP, the polarization is prepared in the state $|L\rangle$. The light beam then passes through a q-plate, whose retardation can be tuned suitably by varying a controlled external electric field [15]. As discussed previously, at the exit of the device the initial optical field is converted

[2] Some paragraphs and sentences of this section are adapted or copied verbatim from the work [40] which I coauthored.

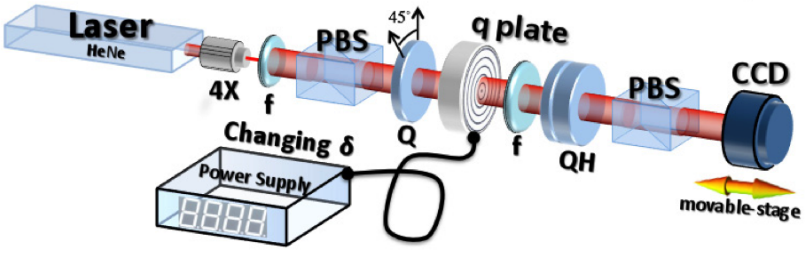

FIGURE 2.9: Experimental setup [40]. A He-Ne laser beam is first spatially filtered focusing via a microscope objective (4X) into a 50 μm pinhole; the beam is then collimated using a lens (f). Its polarization is then prepared in a left (right) circular state by a polarizing beam-splitter (PBS) and a quarter-wave plate (Q). A q-plate with tunable retardation δ then transforms the beam into a PSB. The polarization pattern of the latter was analyzed by a quarter-wave plate, a half-wave-plate (H) and another polarizer, followed by imaging on a CCD camera. The δ parameter of the PSB was adjusted by electrically tuning the q-plate. In order to study the propagation dynamics of the PSB, the CCD camera was mounted on a translation stage and moved around the focal plane of an output lens.

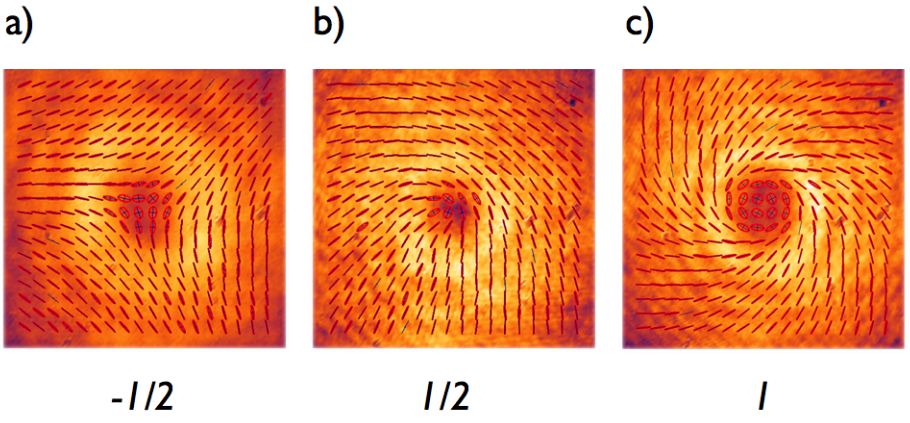

FIGURE 2.10: Intensity and polarization distribution at the near field for beams generated with q-plates having different topological charges [40]. a) When $q = -1/2$, we obtain a star at the central point. b) The lemon correspond to $q = 1/2$. c) When $q = 1$ the C-point charge is equal to 1, and the surrounding pattern has a spiraling structure.

in a PSB; its singular polarization distribution has been measured in the near and in the far field, corresponding to the image and focal plane of a lens positioned after the q-plate, respectively. Using the same technique reported in Sec. 2.3, we determined the Stokes parameters in every grid made of 20×20 pixels. Three examples of the reconstructed polarizations are reported in Fig. 2.10; tuning the plate retardation to the value $\delta = \pi/2$, we measured the near field polarization distribution when using q-plates with q=1/2,-1/2 and 1. Associated patterns have a C-point on the beam axis, with topological charge equal to that of the plate. Then using a device with q=1/2, we adjusted the coefficients c_L and c_R of Eq. 2.7 by varying δ from 0 to $3\pi/2$, in steps of $\pi/4$. For optical retardations

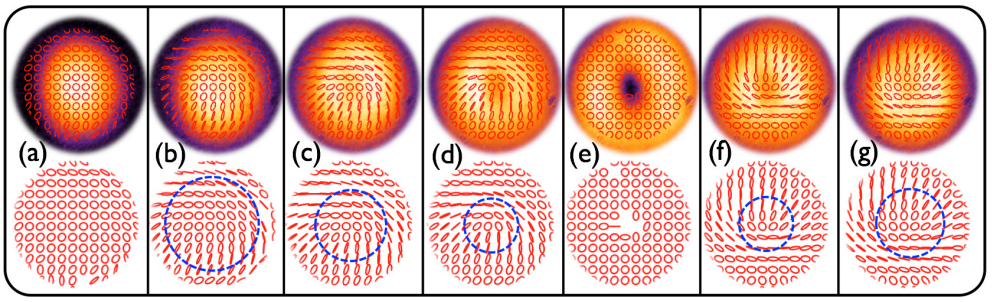

FIGURE 2.11: Intensity distributions and reconstructed polarization patterns of beams generated by a q-plate with $q = 1/2$, for seven different optical retardations [40]. (a) $\delta = 0$ (or 2π), (b) $\delta = \pi/4$, (c) $\delta = \pi/2$, (d) $\delta = 3\pi/4$, (e) $\delta = \pi$, (f) $\delta = 5\pi/4$, and (g) $\delta = 3\pi/2$. The corresponding L-line radii relative to the beam waist w_0 are the following: (a) undefined (b) $\rho_0 = 2.0w_0$, (c) $\rho_0 = 1.4w_0$, (d) $\rho_0 = 1.1w_0$, (e) undefined, (f) $\rho_0 = 1.0w_0$, and (g) $\rho_0 = 1.5w_0$.

$\delta = 0$ and $\delta = \pi$, the beam has uniform polarization corresponding to states $|L\rangle$ and $|R\rangle$, respectively. In the first case, the beam profile is Gaussian, whereas for $\delta = \pi$ it has the classical doughnut shape. In intermediate cases, the beam has a C-point at its center, with charge $\eta = q$. The value of δ determines the radius of the L-line, which decreases when going from 0 to π; moreover, we can observe that the two regions $\delta < \pi$ and $\delta > \pi$ are distinguished by a π rotation of the polarization pattern, as a result of a π difference in the relative phase between coefficients c_L and c_R. In a second experiment, we studied the dynamics of different PSBs with $\eta = -1/2, +1/2$ and $+1$ topologies under free-air propagation, keeping the parameter δ fixed to the value $\pi/2$. To this purpose, we moved the CCD camera along the propagation axis around the imaging-lens focal plane. We recorded the beam polarization patterns at six different planes in the range $-z_R \leq z \leq z_R$, where z_R is the lens Rayleigh parameter and $z = 0$ corresponds to the beam waist location. The experimental results are shown in Fig. 2.12. As it can be seen, the polarization pattern evolves during propagation. Indeed LG_{00} and $\mathrm{LG}_{0,m}$ modes of Eq. (2.7) have different z dependences of their Gouy phases; the relative Gouy phase between them is given by $\psi = |m| \arctan(z/z_0)$, which in the explored region varies in the range $|m|[-\pi/4, \pi/4]$. In the case $m = \pm 1$ (i.e. $\eta = 1/2$) the phase evolution leads to a rigid rotation of the whole polarization structure by an angle equal to ψ [as shown in Fig. 2.12 a) and b)], while when $m = 2$ (i.e. $\eta = 1$), the pattern dynamics consists in the evolution from radial to spiral and then to azimuthal distributions (Fig. 2.12 c)).

Before concluding, we discuss the radial distribution of the PSB generated by the q-plate, that we assumed to be that of a Laguerre Gauss mode with $p = 0$. At the exit of the device the field, that was initially in a uniformly polarized ($|L\rangle$) Gaussian state, is given by

$$\widehat{\mathrm{U}}_\delta \cdot |L\rangle = \mathrm{HyGG}_{-|q|\sqrt{2},q\sqrt{2}}(\rho, d/\bar{n}) \left[\cos\left(\frac{\delta}{2}\right)|L\rangle + e^{i2\alpha_0} \sin\left(\frac{\delta}{2}\right)|R\rangle\, e^{2iq\,\phi} \right], \quad (2.10)$$

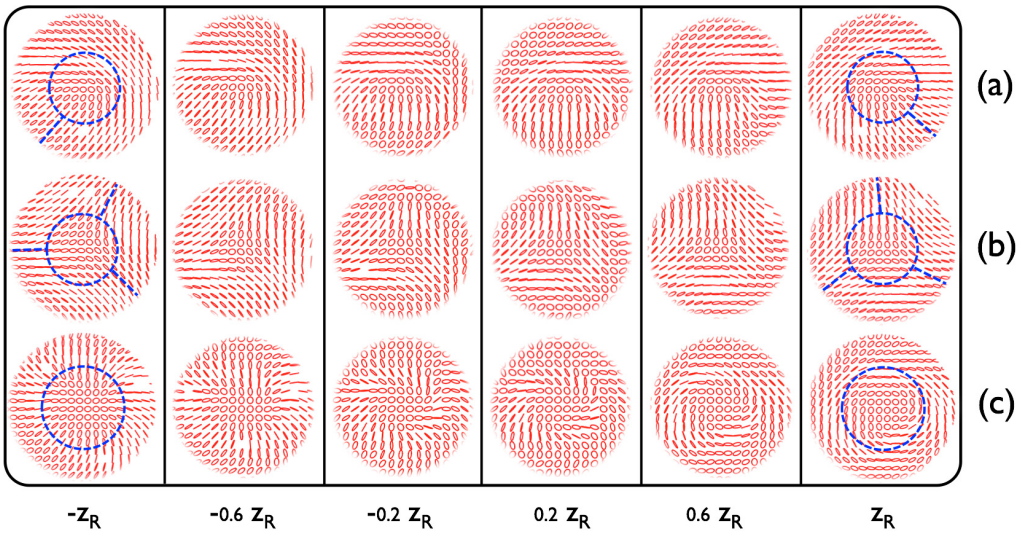

FIGURE 2.12: Reconstructed experimental polarization patterns of different PSB beams [40]. (a) $\eta = m/2 = +1/2$, (b) $\eta = m/2 = -1/2$ and (c) $\eta = m/2 = +1$. Patterns have been reconstructed by measuring the maps of reduced Stokes parameters in six different longitudinal planes within the beam Rayleigh range, from $-z_R$ to $+z_R$. The corresponding rotation of polarization patterns for (a) and (b) are 90° and $88° = (30 + 30 + 28)°$, respectively.

where the operator $\widehat{\mathrm{U}}_\delta$ describes the action of a q-plate, including the alteration of the radial profile of the impinging beam. In Eq. 2.10, $\mathrm{HyGG}_{-|q|\sqrt{2},q\sqrt{2}}$ denotes the amplitude profile of a hypergeometric-Gaussian beam [11]. The latter equation describes with good approximation the output mode profile of a q-plate of charge q, thickness d and average refractive index $\bar{n}$ for a Gaussian input (see Ref. [50] for more details). In the far-field, the profiles associated with the converted and un-converted terms are different. However the HyGG term multiplied by the phase factor $\exp(2iq\phi)$ can be expanded in a series of LG modes [11] with $m = 2q$ and different p. In the far-field, it is a good approximation to consider only the larger term, coinciding with $\mathrm{LG}_{0,2q}$. In this case, Eq. (2.10) is reduced to Eq. (1.60). The output state coincides with expression 2.9.

Chapter 3

Testing the foundations of quantum mechanics

3.1 Introduction

Quantum mechanics (QM) is the physical theory we use to model all natural phenomena we observe at the microscopic scale, which eventually determines the properties of macroscopic objects. While no experimental outcome has ever contradicted its predictions, it has subtle features which have intrigued the scientific community hitherto. In 1935, Einstein, Podolsky and Rosen (EPR) argued QM to be an *incomplete* theory, formulating their results in terms of a famous paradox [51]. Aiming to recover the physical realism and the theory completeness, Hidden Variable Theories (HVT) were introduced [52–54]; they extended QM through the addition of more dynamical variables, which have a deterministic evolution, whereas we are not able to observe them experimentally. The lack of a direct evidence of such elements seemed to determine the impossibility to test whether HVT were plausible or not. An important breakthrough was achieved in 1964, thanks to a theorem formulated by J. S. Bell [53]. Considering a bipartite system, he proved that the correlations predicted by any local HVT were limited by an upper bound, while for entangled degrees of freedom QM predictions did not fulfill this requirement. Bell's inequalities were tested for the first time in 1982 in the pioneering experiment by A. Aspect, J. Dalibard and G. Roger [55]; the authors measured the polarization of two photons emitted simultaneously in an atomic process, showing that their correlations indeed respected QM laws, thus violating the inequalities. In the same spirit, A. J. Leggett formulated a novel theorem in 2003, which included a class of theories which were non-local [56]. Results of previous experiments could not be used to test Leggett's inequalities, which needed some extra measurements. In recent

years the violation of such inequalities has been reported adopting several experimental schemes [57–61].

We learn from Bell-like theorems that a feasible route to test the possibility of hidden variable models is to evaluate the correlations between two degrees of freedom of a bipartite system; here entanglement is the main resource, because these highly correlated systems show features which are not reproducible by HVTs. It is quite common to identify these bipartite systems with a pair of identical particles, considering for each of them a 2D degree of freedom, such as the polarization of a single photon. When measuring some property of one particle of the pair, this approach allows to exploit the locality (or relativistic causality) principle to assume that the outcome could not depend on any operation performed simultaneously on the other party, because of the space-like separation between these events. Nevertheless, Bell's or Leggett's theorems can be investigated by means of the entanglement between two degrees of freedom of a single particle [62]. While locality cannot be assumed anymore, we can rely on the more general non-contextuality of the two considered observables [63]. Spin and orbital angular momentum of single photons are perfect candidates for this kind of tests, as we will show later on.

In this chapter we report on two experiments aiming to test contextual and non-contextual hidden variable theories. In both cases, we exploited the non classical correlations between the SAM and the OAM of single photons whose state is suitably prepared using wave plates and a q-plate. Non-contextual hidden variable theories (NCHVT) where studied through the verification of the Hardy paradox, which is a particular case of a Bell-like theorem without inequalities [64]. On the other hand, we investigated Leggett's inequalities to test a class of contextual hidden variable models. Before presenting the associated results, we will discuss the main ingredients of hidden variable theories in the framework of the non-contextuality principle; we will complete the discussion providing a simple derivation of the Bell theorem, the Hardy paradox and introducing Leggett's inequalities.

3.2 EPR Paradox, locality and contextuality

Following EPR [51], the completeness of a physical theory consists in a one-to-one correspondence between its elements and the so called elements of reality characterizing the described system. An element of reality is a feature of the system that the theory predicts deterministically. For instance, let us consider a horizontally polarized photon passing through a polarizing beam splitter (PBS), oriented so as to transmit and reflect horizontal and vertical polarizations, respectively. Placing a couple of detectors at the exit ports, we can measure the quantity S_1, which is equal to ± 1 according to the

photon being transmitted or reflected, respectively. The associated quantum operator is $\widehat{S}_1 = |H\rangle\langle H| - |V\rangle\langle V|$. As a consequence of the initial state preparation, we know that repeating the experiment many times we would always obtain S_1=1; thus we can associate an element of reality with the latter quantity, since even without measuring it we can be sure that it is equal to one. With the help of wave plates, we can use the same PBS to measure S_2, associated with the operator $\widehat{S}_2 = |D\rangle\langle D| - |A\rangle\langle A|$; this time, we will get $S_2 = \pm 1$, where at each outcome is associated a probability equal to 1/2. The absence of a deterministic result denies in this case the possibility to assign S_2 an element of reality. This simple example allows us to understand that in QM there exist no states describing systems with elements of reality associated with non-commuting operators, as for example $\widehat{S}_1$ and $\widehat{S}_2$. EPR argues that these systems are possible in nature, thus claiming that quantum mechanics is an incomplete theory.
EPR paradox has been formulated in a more accessible version by Bohm [52]; he considered a pair of identical photons, whose quantum state is given by

$$|\psi\rangle = \frac{1}{\sqrt{2}}(|H\rangle_1|V\rangle_2 - |V\rangle_1|H\rangle_2) \tag{3.1}$$

where photons 1 and 2 (P1 and P2) are propagating along different directions. State of Eq. 3.1 describes for example the polarization state of photon pairs generated through spontaneous parametric downconversion in a nonlinear crystal. In this case, if we measure $S_1^{(1)}$ for P1, with equal probability we could get the outcome $+1$ or -1; nevertheless if in a single run we get $S_1^{(1)} = 1$, we know with probability equal to one that $S_1^{(2)} = -1$. Assuming that the two observables are local, the outcome of a measurement on P2 cannot be affected by the choice of the detection settings on P1; thus we can conclude that $S_1^{(2)} = -1$ even before the experiment and we assign it an element of reality. In a different experiment, we could choose to measure S_2 for both particles. In the new basis, the photon pair is described by the state

$$|\psi\rangle = \frac{1}{\sqrt{2}}(|A\rangle_1|D\rangle_2 + |D\rangle_1|A\rangle_2). \tag{3.2}$$

Assuming the we get the outcome $S_2^{(1)} = 1$, we again know with probability equal to one that $S_2^{(2)} = -1$ even without performing any further measurement. As for the previous case, $S_2^{(2)}$ may be considered as an element of reality for the system. Here comes the paradox, since, first of all, the elements of reality we are assigning to the system depend on the measurement that has been performed. If these two elements are a real feature of the system, then in QM we do not have a state to describe it. In this formulation of the paradox, it is important to point out the role of the locality principle. If any measurement on P1 could alter the state of the distant photon, it would not be possible to assign elements of reality to P2, since its properties have changed with respect to the

initial configuration.
For any pair of observables A and B, it is possible to state whether in joint measurements a single outcome is influenced or not by the choice of the detection settings relative to the other observable. The second case represents the non-contextuality assumption, which generalizes the locality principle to the case where A and B are not associated with distant objects, but for example represent different degrees of freedom of a single particle. The non-contextuality can be invoked when the observables are compatible; in the QM framework, this is equivalent to the requirement that

$$[\widehat{A}, \widehat{B}] = 0 \tag{3.3}$$

Considering non-contextuality in place of locality does not alter the content of Bell-like theorems, but only the interpretation about which class of HVT they investigate.

3.3 Hidden variables and the Bell theorem

EPR concluded their famous paper stating that *"the wave function does not provide a complete description of the physical reality"*, conjecturing on the other hand that this description would be possible [51]. With the aim of completing the theory, hidden variable theories rely on the presence of deterministic variables which have a dynamical evolution and fully characterize the state of the system. If on one hand these variables cannot be detected experimentally, on the other we can think that the values of the observable quantities are just the result of ensemble averages, assuming that HV have a specific probability distribution.
In his celebrated theorem, J. S. Bell considered an explicit HV model to describe the spin state of a spin 1/2 particle, or equivalently the polarization of a single photon [53]. When this model is extended to systems as those described by Eq. 3.1, its predictions do not match the ones by QM and, above all, the experimental results.
Let us consider the Bell model for the polarization of single photons. Here, it is convenient to label a polarization state using unit vectors $\hat{\mathbf{p}}$, which individuate points on the Poincaré sphere. In this context, we will refer to a PBS oriented along the direction $\hat{\mathbf{a}}$ when this, combined with suitable wave plates, will transmit or reflect $\hat{\mathbf{a}}$ and $-\hat{\mathbf{a}}$ polarizations, respectively. Such a PBS, plus two detectors at the exit ports, is used to measure the quantity A, whose average value is given by

$$\langle \widehat{A} \rangle = \hat{\mathbf{a}} \cdot \hat{\mathbf{p}} \tag{3.4}$$

This is the content of the famous Malus law. When measuring A, the result of each individual measurement will depend on the orientation of the apparatus and on the

value of some hidden variables λ which are specifying the state of the system

$$A = A(\hat{\mathbf{a}}, \lambda). \tag{3.5}$$

Variables λ are defined in a specific domain Λ and are characterized by a probability distribution $\rho(\lambda)$. The average value of A over the possible values of the HV is defined as

$$\bar{A} = \int_{\Lambda} d\lambda\, \rho(\lambda)\, A(\hat{\mathbf{a}}, \lambda) \tag{3.6}$$

The mean values $\bar{A}$ and $\langle \widehat{A} \rangle$ are not the same quantities, but they have to coincide if we want the HV model to be a plausible theory; indeed we know that QM predicts correctly all experimental outcomes reported hitherto. A possible model satisfying the requirement $\bar{A} = \langle \widehat{A} \rangle$ is the following;

$$\bar{A}(\hat{\mathbf{a}}, \lambda) = \begin{cases} 1 & 0 \leq \lambda \leq \lambda_a \\ -1 & \lambda_a < \lambda \leq 1 \end{cases} \qquad \lambda_a = \frac{\hat{\mathbf{p}} \cdot \hat{\mathbf{a}} + 1}{2} \tag{3.7}$$

when assuming $\rho(\lambda) = 1$ in the domain Λ. It is straightforward to prove that

$$\bar{A} = \int_{\Lambda} d\lambda\, \rho(\lambda)\, A(\hat{\mathbf{a}}, \lambda) = \hat{\mathbf{p}} \cdot \hat{\mathbf{a}} \tag{3.8}$$

Now we are ready to generalize the model to the case of two non-contextual observables A and B. The correlation between the two quantities is defined as

$$\overline{AB} = \int_{\Lambda} d\lambda\, \rho(\lambda)\, A(\hat{\mathbf{a}}, \lambda) B(\hat{\mathbf{b}}, \lambda) \tag{3.9}$$

Here the non-contextuality allows us to consider A and B as depending only on their detection settings and not on the others. Consider now two experiments; in the first, we measure A and B along $\hat{\mathbf{a}}$ and $\hat{\mathbf{b}}$, while in the second we measure A' and B' along $\hat{\mathbf{a}}'$ and $\hat{\mathbf{b}}'$. Being binary variables which can be equal only to ± 1, A, B, A', and B' verify the following equation

$$(A + A')B - (A - A')B' = \pm 2 \tag{3.10}$$

This equation is meaningful only if assuming the non-contextuality of the observables. Doing the ensemble average of Eq. 3.10, and considering its absolute value, we get

$$\left|\overline{AB} + \overline{A'B} - \overline{AB'} + \overline{A'B'}\right| = \left| \int_{\Lambda} d\lambda\, \rho(\lambda) \left[(A + A')B - (A - A')B'\right] \right| \leq 2 \tag{3.11}$$

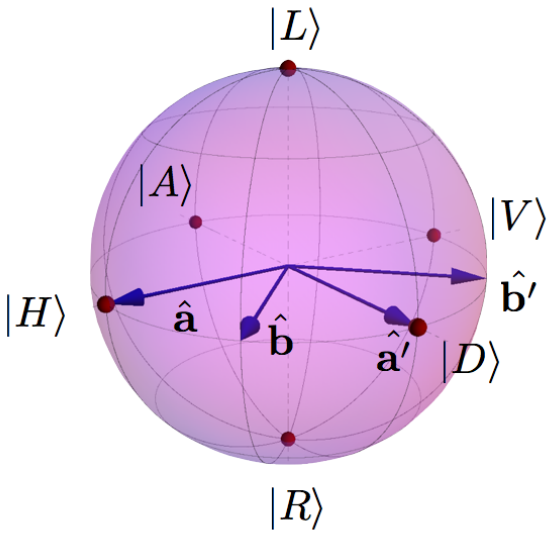

FIGURE 3.1: Sets of states for the maximal violation of CHSH inequalities.

Bell inequalities in the form of Eq. 3.11 were formulated by J. F. Clauser, M.A. Horne, A. Shimony e R. A. Holt, thus they are referred to as CHSH inequalities [65]. Eq. 3.11 states that any non-contextual hidden variable theory (NCHVT) would predict an upper bound for a suitable combination of correlations between the two degrees of freedom. These restrictions are effectively violated when considering QM predictions for entangled states. For instance, for the state of Eq. 3.1 the correlation between A and B is equal to

$$C(\hat{\mathbf{a}}, \hat{\mathbf{b}}) = \hat{\mathbf{a}} \cdot \hat{\mathbf{b}}. \tag{3.12}$$

If $\hat{\mathbf{a}}$, $\hat{\mathbf{b}}$, $\hat{\mathbf{a}}'$ and $\hat{\mathbf{b}}'$ lie on the equator of the Poincaré sphere and are equally spaced by an angle equal to $\pi/4$ (as shown in Fig. 3.1), it is simple to show that the left term of Eq. 3.11 becomes $2\sqrt{2}$, which is clearly larger than 2. The violation of the Bell or CHSH inequalities has been reported several times starting from the pioneering work by A. Aspect *et al.* [55]. Though an experiment satisfying simultaneously all requirements of the Bell's theorem, closing the famous loopholes (see [66] and references therein) was not reported yet, it is quite unlikely that a non-contextual realistic model is possible.

3.4 The Hardy Paradox [1]

Bell inequalities pointed out for the first time the contrast between the predictions of any non-contextual realistic theory and quantum mechanics. In 1993 L. Hardy ideated

[1] Some paragraphs and sentences of this section are adapted or copied verbatim from the work [67] which I coauthored.

a novel gedanken experiment [64], providing an illuminating example to show the contradictions arising from this interpretation of physical reality. Hardy's paradox is about a set of certainty or impossibility ("all versus nothing") statements which seems to be contradictory in a classical interpretation, thus providing a form of "Bell's theorem without inequalities" [68]. A similar experiment was proposed by D. Greenberger, M. Horne, and A. Zeilinger (GHZ) [69]; as a difference with respect to the latter, Hardy's experiment requires only two compatible observables (and not three) and requires only partial entanglement (and not maximal). Relying on two-photons entanglement, several tests of the Hardy paradox have been reported hitherto [70–76].

Let us consider two compatible degrees of freedom S_1 and S_2, as for example the polarization of two photons. Assuming the non-contextuality principle, we agree that there can be no relative influence between the measurement operations on different DOFs. When referring to S_1, we can either measure the quantity Σ or Σ', while on S_2 we measure Λ or Λ'. Σ and Σ' are not compatible measurements, as the associated quantum operators are not commuting; the same condition holds for Λ and Λ'. On the other hand, we remark that Σ and Σ' are compatible with Λ and Λ'.

We repeat the experiment many times, considering a large ensemble of photons prepared in the identical initial state. For each degree of freedom, we choose at random the detection settings among the possible configurations defined previously. As a result of the experiment, we can evaluate the frequencies, and the probabilities as a consequence, of the events associated with all possible combinations of Σ, Σ', Λ and Λ' being ± 1. Now we conjecture that is possible to prepare the initial state in order to get these results:

P1 : The outcome $\Sigma = +1$ and $\Lambda = +1$ never occurs, that is $P_{\Sigma,\Lambda}(+1,+1) = 0$.

P2 : The outcome $\Sigma = -1$ and $\Lambda' = -1$ never occurs, that is $P_{\Sigma,\Lambda'}(-1,-1) = 0$.

P3 : The outcome $\Sigma' = -1$ and $\Lambda = -1$ never occurs, that is $P_{\Sigma',\Lambda}(-1,-1) = 0$.

It will be proved below that for any realistic non-contextual model, these three properties should logically imply the validity of the following fourth property:

P4 : The outcome $\Sigma' = -1$ and $\Lambda' = -1$ never occurs, that is $P_{\Sigma',\Lambda'}(-1,-1) = 0$

It is possible to show that quantum mechanics predictions, and real experimental outcomes, allows us to find that, in a sizable fraction of measurements of Σ' and Λ', the outcome $\Sigma' = -1$ and $\Lambda' = -1$ is indeed obtained, thus contradicting P4. This is Hardy's paradox.

The proof of P4 from P1-P3 is very simple. We can interpret Eq. P2 as follows: if we measure $\Lambda' = 1$, with probability equal to one we will find that $\Sigma = +1$. At the same

time, from Eq. P3, we can deduce that if we measure $\Sigma' = 1$, than $\Lambda = +1$. From equation P1, we know that the outcome $\Lambda = +1$ and $\Sigma = +1$ occurs with vanishing probability; as a consequence of the two previous statements, it is not possible to have $\Lambda' = -1$ and $\Sigma' = -1$. Using Venn diagrams, we can visualize the properties we deduced based on Eq. P1-P3. The Venn sets associated with the outcomes $\Sigma = +1, \Sigma' = -1, \Lambda = +1$, and $\Lambda' = -1$ are shown in Fig. 3.2. From property P2 we infer that the event $\Lambda' = -1$ implies the event $\Sigma = +1$ which is represented by the fact that the Venn set for the event $\Lambda' = -1$ is internal to that for the event $\Sigma = -1$, as shown in Fig. 3.2. Similarly, from P3 we infer that the event $\Sigma' = -1$ implies the event $\Lambda = +1$, that is, the Venn set of the event $\Sigma' = -1$ is internal to that of the event $\Lambda = +1$. Now property

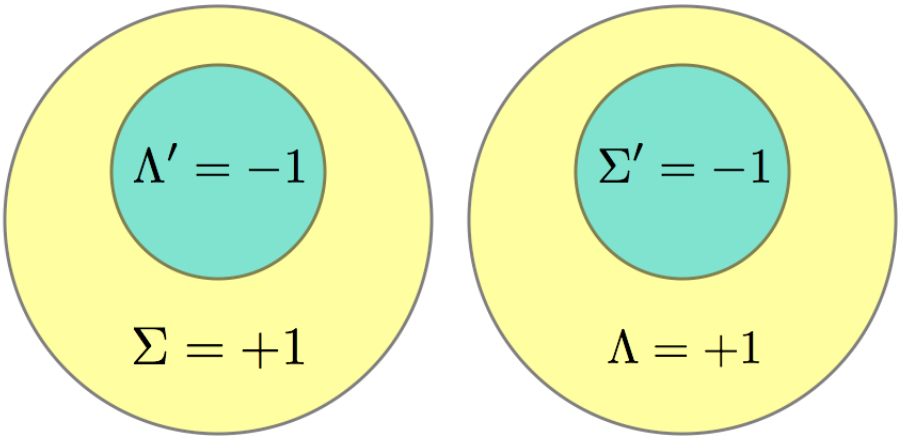

FIGURE 3.2: Venn diagrams for the events $\Sigma = +1, \Sigma' = -1, \Lambda = +1$, and $\Lambda' = -1$, satisfying conditions P1, P2, P3. The sets $\Sigma' = -1$ and $\Lambda' = -1$ being internal to disjoint sets cannot intersect, so that P4 follows immediately.

P1 implies that the Venn sets of the events $\Sigma = +1$ and $\Lambda = +1$ have no intersection, as shown in Fig. 3.2. It is now evident from the figure that the sets of the events $\Sigma' = -1$ and $\Lambda' = -1$ cannot intersect as well, from which we deduce property P4.

We shall now prove that there exist physical systems where probabilities predicted by quantum mechanics verify Eqs. P1-P3, whereas they violate Eq. P4. In agreement with our experimental strategy, as degrees of freedom we consider single photon's SAM and the OAM, where for the latter we restrict our attention to the subspace generated by the two helical modes $|\pm 1\rangle$. As discussed in Ch. 1, in the paraxial limit SAM and OAM represent compatible observables (see Eq. 1.24), thus they can be exploited for this kind of tests. In this spin-orbit space, the Hardy state is expressed as

$$|\psi\rangle = \cos(\gamma)|L\rangle_p|-1\rangle_o - \sin(\gamma)|R\rangle_p|1\rangle_o, \tag{3.13}$$

where the p and o subscripts denote the polarization and OAM Hilbert spaces $\mathcal{H}_p$ and $\mathcal{H}_o$, respectively[2]. The entanglement in the state $|\psi\rangle$ is determined by the angle γ; separable or maximally entangled states are obtained when $\gamma = 0$ and $\gamma = \pi$, respectively, while partial entanglement is associated with intermediate values. In the following we shall restrict γ to the range $0 < \gamma < \pi/4$.

Let us now define the observables to be measured in the experiment, expressing them in terms of the associated quantum operators. For each 2D Hilbert space, let us consider two pairs of orthogonal states:

$$\begin{aligned}
|+\rangle_i &= N\left(\sqrt{\sin\gamma}\,|+1\rangle_i + \sqrt{\cos\gamma}\,|-1\rangle_i\right)\\
|-\rangle_i &= N\left(-\sqrt{\cos\gamma}\,|+1\rangle_i + \sqrt{\sin\gamma}\,|-1\rangle_i\right)\\
|+'\rangle_i &= N'\left(\sqrt{\cos^3\gamma}\,|+1\rangle_i + \sqrt{\sin^3\gamma}\,|-1\rangle_i\right)\\
|-'\rangle_i &= N'\left(-\sqrt{\sin^3\gamma}\,|+1\rangle_i + \sqrt{\cos^3\gamma}\,|-1\rangle_i\right)
\end{aligned} \tag{3.14}$$

where $N = (\sin\gamma + \cos\gamma)^{-1/2}$ and $N' = (\sin^3\gamma + \cos^3\gamma)^{-1/2}$, and $i = p, o$. When $i = p$, states $(|+1\rangle_p, |-1\rangle_p)$ correspond to circular polarizations $(|L\rangle, |R\rangle)$. The observable operators are then defined as follows:

$$\begin{aligned}
\hat{\Sigma} &= |+\rangle_p\langle+|_p - |-\rangle_p\langle-|_p\\
\hat{\Sigma}' &= |+'\rangle_p\langle+'|_p - |-'\rangle_p\langle-'|_p\\
\hat{\Lambda} &= |+\rangle_o\langle+|_o - |-\rangle_o\langle-|_o\\
\hat{\Lambda}' &= |+'\rangle_o\langle+'|_o - |-'\rangle_o\langle-'|_o
\end{aligned} \tag{3.15}$$

Let us now calculate the quantum predictions for the four probabilities appearing in properties P1–P4. They are given by expressions such as $P_{\Sigma,\Lambda}(+1,+1) = |\langle+|_p\langle+|_o|\psi\rangle|^2$ and similar ones. A simple calculation shows that the probabilities appearing in P1, P2, P3 are indeed zero, but that the probability in P4 is given by

$$P_{\Sigma',\Lambda'}(-1,-1) = |\langle-'|_p\langle-'|_o|\psi\rangle|^2 = \left[\frac{\sin 4\gamma}{4(\cos^3\gamma + \sin^3\gamma)}\right]^2, \tag{3.16}$$

which is nonzero for the range $0 < \gamma < \pi/4$ (hence, for all partially entangled states, excluding only separable and maximally entangled ones). In particular, the probability (3.16) is maximized for $\gamma \approx 24.9°$, for which $P_{\Sigma',\Lambda'}(-1,-1) = [(1+\sqrt{5})/2]^{-5} \approx 9\%$.

The experimental verification of the Hardy paradox would require the measurement of

[2]Please note that in this section we adopted the label p to refer to the SAM space, in place of the greek letter π.

vanishing probabilities; in real experiments, different kind of errors and finite instrumental accuracy makes this an extremely difficult task. Nevertheless we introduce an inequality which generalizes the Hardy paradox to take into account experimental imperfections; a similar result was already reported by Mermin [68].

Realism of the model means that we can assign probabilities to the set of elementary events corresponding to each possible result of the measurement of the observables $\Sigma, \Lambda, \Sigma', \Lambda'$, even when they are not measured. Because each measurement can have only the two results ± 1, we have sixteen probabilities associated with each event. The difference between a realistic statistical model and quantum mechanics stems from the fact that, in the former, probabilities can be assigned to the elementary events, while this is impossible in quantum mechanics in general. For example, any realistic statistical model assigns values (eventually zero or one) to all 16 probabilities $\mathcal{P}_n$ $(n = 1, \ldots, 16)$ of the four-fold joint measurements of Σ, Σ', Λ, and Λ', as reported in Table 3.1; this is impossible in quantum mechanics, because the primed observables do not commute with the unprimed ones. Besides realism, the model non-contextuality corresponds to

	Σ	Σ'	Λ	Λ'		Σ	Σ'	Λ	Λ'
$\mathcal{P}_1$	-1	-1	-1	-1	$\mathcal{P}_9$	$+1$	-1	-1	-1
$\mathcal{P}_2$	-1	-1	-1	$+1$	$\mathcal{P}_{10}$	$+1$	-1	-1	$+1$
$\mathcal{P}_3$	-1	-1	$+1$	-1	$\mathcal{P}_{11}$	$+1$	-1	$+1$	-1
$\mathcal{P}_4$	-1	-1	$+1$	$+1$	$\mathcal{P}_{12}$	$+1$	-1	$+1$	$+1$
$\mathcal{P}_5$	-1	$+1$	-1	-1	$\mathcal{P}_{13}$	$+1$	$+1$	-1	-1
$\mathcal{P}_6$	-1	$+1$	-1	$+1$	$\mathcal{P}_{14}$	$+1$	$+1$	-1	$+1$
$\mathcal{P}_7$	-1	$+1$	$+1$	-1	$\mathcal{P}_{15}$	$+1$	$+1$	$+1$	-1
$\mathcal{P}_8$	-1	$+1$	$+1$	$+1$	$\mathcal{P}_{16}$	$+1$	$+1$	$+1$	$+1$

TABLE 3.1: Set of all possible values for the four observables Σ, Σ', Λ, Λ' and corresponding symbols for the probabilities.

the assumption that the results of a measurements on a given observable are independent of possible joint measurements carried out on other compatible observables. This means that each probability $\mathcal{P}_n$ depends on the observables pertaining the system under study and not on the context in which the measurements are performed. In particular, the $\mathcal{P}_n$ cannot depend on parameters characterizing the measurement apparatus or the environment. Non-contextuality is always assumed in classical physics and it is implicit in the probabilities $\mathcal{P}_n$ in Table 3.1, independently of their actual values. From the probabilities $\mathcal{P}_n$, we may easily calculate the probabilities defining properties P1–P4,

relevant for Hardy's paradox. We obtain

$$\begin{aligned} P_{\Sigma,\Lambda}(+1,+1) &= \mathcal{P}_{11} + \mathcal{P}_{12} + \mathcal{P}_{15} + \mathcal{P}_{16} \\ P_{\Sigma',\Lambda}(-1,-1) &= \mathcal{P}_1 + \mathcal{P}_2 + \mathcal{P}_9 + \mathcal{P}_{10} \\ P_{\Sigma,\Lambda'}(-1,-1) &= \mathcal{P}_1 + \mathcal{P}_3 + \mathcal{P}_5 + \mathcal{P}_7 \\ P_{\Sigma',\Lambda'}(-1,-1) &= \mathcal{P}_1 + \mathcal{P}_3 + \mathcal{P}_9 + \mathcal{P}_{11} \end{aligned} \tag{3.17}$$

Observing that all probabilities on the right of the last of Eqs. (3.17) are already present on the right of the first three equations, we find the following inequality

$$\begin{aligned} P_{\Sigma',\Lambda'}(-1,-1) \quad \leq \quad & P_{\Sigma,\Lambda}(+1,+1) + P_{\Sigma',\Lambda}(-1,-1) \\ & + P_{\Sigma,\Lambda'}(-1,-1) \end{aligned} \tag{3.18}$$

This relation should hold true in any non-contextual realistic model and is trivially satisfied in the ideal noiseless case given by properties P1–P4.

3.5 Leggett Inequalities[3]

In 2003 A. J. Leggett formulated a new theorem providing a set of inequalities for a class of contextual HVTs, which he named as Crypto-Contextual Hidden Variable Theories [56]. In analogy to Bell and Hardy models, he considered a bipartite system characterized by two degrees of freedom, that we can name X and Y. In the original paper, the SAM (polarization) of two correlated photons was used, while again here we take X to be the SAM and Y a 2D subspace of OAM of a single photon introduced in the previous section. Two observers perform projective measurements on the two degrees of freedom, using detection apparatus defined by vectors $\hat{\mathbf{a}}$ and $\hat{\mathbf{b}}$ on the Poincaré spheres relative to X and Y, respectively. In the crypto-contextual models, as for the Bell model, the possible outcomes of these measurements are pre-determined (either deterministically or stochastically) by a set of hidden variables λ, defined in a domain Λ. Due to our lack of knowledge about these hidden variables, all measured quantities result from an average in the hidden variable domain, weighted by the probability distribution $\rho(\lambda)$ that the system is in state λ.

In the original model proposed by Leggett [56], the hidden variables λ are defined by assigning a specific "hidden" spin-like state $\hat{\mathbf{u}}$ to X and $\hat{\mathbf{v}}$ to Y. This is done even if the overall quantum state is prepared in an entangled state for which the individual

[3]Some paragraphs and sentences of this section are adapted or copied verbatim from the work [67] which I coauthored.

subsystems A and B would have no definite quantum state. The expectation values for the observables X and Y with measurement settings $\hat{\mathbf{a}}$ and $\hat{\mathbf{b}}$, respectively, are then assumed to be given by the following expressions:

$$\begin{aligned} \langle x \rangle_\lambda &= \sum_x x\, P(x|\hat{\mathbf{a}}, \hat{\mathbf{b}}, \lambda) = \hat{\mathbf{u}} \cdot \hat{\mathbf{a}}, \\ \langle y \rangle_\lambda &= \sum_y y\, P(y|\hat{\mathbf{a}}, \hat{\mathbf{b}}, \lambda) = \hat{\mathbf{v}} \cdot \hat{\mathbf{b}}, \end{aligned} \tag{3.19}$$

where $\lambda = (\hat{\mathbf{u}}, \hat{\mathbf{v}})$. The correlation $C(\hat{\mathbf{a}}, \hat{\mathbf{b}})$ between measurements performed on X and Y are given by the expression

$$C(\hat{\mathbf{a}}, \hat{\mathbf{b}}) = \int_\Omega d\lambda\, \rho(\lambda) \left(\sum_{xy} xy\, P(x, y|\hat{\mathbf{a}}, \hat{\mathbf{b}}, \lambda) \right), \tag{3.20}$$

where $P(x, y|\mathbf{a}, \mathbf{b}, \lambda)$ is a joint probability that the outcome projective measurement on $\mathbf{a}$ and $\mathbf{b}$ are x and y, respectively. The model allows for contextuality of the two observables X and Y, because this joint probability is in general non-separable, that is, $P(x, y|\mathbf{a}, \mathbf{b}, \lambda) \neq P(x|\mathbf{a}, \lambda)P(y|\mathbf{b}, \lambda)$. This in particular implies that each individual measurement outcome x of the observable X may in general depend on the observable Y settings $\mathbf{b}$, and possibly even on its simultaneous outcome y, and vice versa. However, it should be noted that Eqs. (3.19) do imply a "non–signalling" condition, so that each average value of a given observable is taken to be independent of the measurement settings of the other observable.

For this model, C. Branciard *et al.* derived a simplified version of Leggett-type inequalities [60], which we adopted for the experimental test of contextual realism (see next section). This inequality involves three measurements on X along the vectors $\mathbf{a}_i$ and six on Y, along the vectors $\mathbf{b}_i$ and $\mathbf{b}'_i$, where $i = \{1, 2, 3\}$, with the following constraints: the three vector pairs $\mathbf{b}_i, \mathbf{b}'_i$ form a same angle ϕ, their differences $\mathbf{b}_i - \mathbf{b}'_i$ must be three mutually orthogonal vectors, and their sums $\mathbf{b}_i + \mathbf{b}'_i$ must be respectively parallel to the $\mathbf{a}_i$ (see Fig. 3.9). When these conditions are satisfied, Leggett's model gives rise to the following inequality [60]:

$$\begin{aligned} E_3(\phi) &= \frac{1}{3} \sum_{i=1}^{3} \left| C(\mathbf{a_i}, \mathbf{b_i}) + C(\mathbf{a_i}, \mathbf{b'_i}) \right| \\ &\leq 2 - \frac{2}{3} \left| \sin \frac{\phi}{2} \right| = L_3(\phi). \end{aligned} \tag{3.21}$$

Quantum mechanics, on the other hand, predicts a violation of this inequality. Indeed, if the system is prepared in a maximally entangled state of the observables X and Y, such as for example $|\Phi^+\rangle = (|+1\rangle_p|-1\rangle_o + |-1\rangle_p|+1\rangle_o)/\sqrt{2}$, the correlation coefficients

predicted by quantum mechanics are given by

$$C(\mathbf{a},\mathbf{b})^{\mathrm{QM}} = -\mathbf{a}\cdot\mathbf{b} = -\cos(\phi/2)\,, \tag{3.22}$$

from which we obtain

$$E_3^{\mathrm{QM}}(\phi) = 2|\cos\phi/2|. \tag{3.23}$$

This function $E_3^{\mathrm{QM}}(\phi)$ is above the Leggett bound of Ł$_3(\phi)$ for a wide range of values of the angle ϕ, as shown in Fig. 3.3.

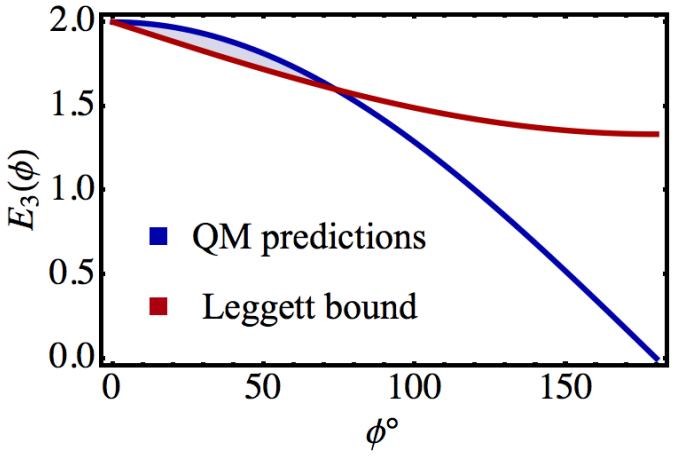

FIGURE 3.3: Comparison between correlations predicted by the Leggett model and those estimated through QM. It is possible to see that for small values of the angle ϕ QM correlations are above the Leggett limit, even though the violation is not as large as for the CHSH inequalities.

3.6 Experimental Tests of Contextual and Non-Contextual Realism

Bell, Hardy and Leggett models consider physical systems made of two degrees of freedom, described in terms of identical 2D Hilbert spaces. As discussed previously, we reproduced these systems considering the SAM and the OAM of a single photon, which represent compatible observables in the paraxial limit. This strategy has several advantages with respect to multi particle schemes, since on one hand it allows higher detection efficiencies, while on the other the tunable generation of entanglement is much simpler;

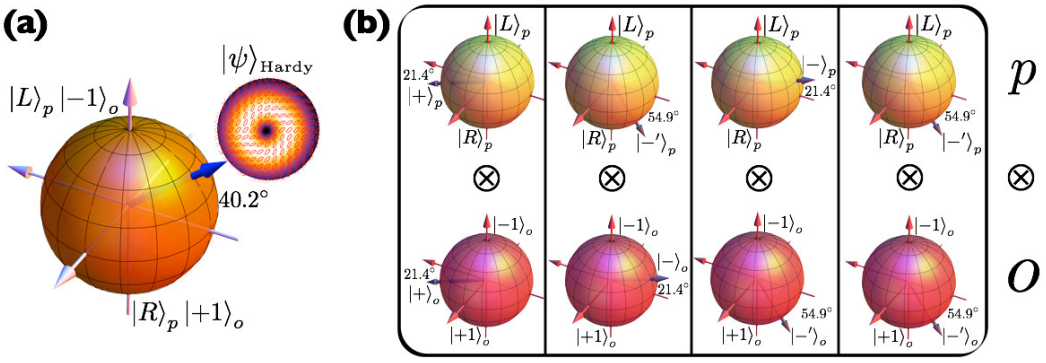

FIGURE 3.4: Poincaré sphere representation in the SAM-OAM space of light for the states involved in the Hardy paradox [67]. (a) Graphical representation of the photon Hardy state (3.13) for $\gamma = 24.9°$ on the higher-order spin-orbit Poincaré sphere [41, 42]. The inset shows also the simulated transverse distribution of polarization (represented by the small ellipses) and intensity (represented by the color brightness) for the optical mode of such Hardy state. (b) Photon states in the Hilbert subspaces of polarization (upper row) and OAM (lower row), represented as arrows on Poincaré (Bloch) spheres. These states define the measured observables in Hardy's paradox test. The mathematical expressions of these states are given in Eq.(3.14).

in our architecture, entanglement between SAM and OAM of a photon is obtained exploiting a single q-plate, whose optical retardation is tuned by means of an external electric field.

3.6.1 Demonstration of the Hardy paradox[4]

To test the Hardy paradox we implemented the projective measurements defined in Eq. 3.15 on a physical system consisting in a single photon, whose spin-orbit state is prepared in the Hardy state (3.13). We experimentally determined the probabilities that the photon is in one of the states associated with the projective measurements (3.15), in order to show that for suitable values of γ our results verify Eqs. P1-P3 while violating Eq. P4. As discussed previously the physical system here considered is described in terms of the 4D spin-orbit Hilbert space of light; in Fig. 3.4 we provide a graphical representation of the states given in Eq. 3.14 in terms the Poincaré spheres relative the SAM and the 2D OAM spaces. In the same picture we report the inhomogeneous polarization distribution charactering the partially entangled Hardy state.

The layout of the apparatus is shown in Fig. 3.5. Photon pairs generated as discussed in Appendix B are coupled into a SMF; at the exit of the latter, a set of wave plates is used to recover the initial polarizations, altered by propagation inside the fiber. Photons are then split by means of PBS, according to their polarization; the V-polarized photon,

[4]Some paragraphs and sentences of this section are adapted or copied verbatim from the work [67] which I coauthored.

reflected at the PBS, is detected by a silicon avalanche photodiode (D1) and used as trigger, whereas the H-polarized photon is used for the Hardy's test, in the heralded single-photon regime. In order to prepare the photonic Hardy state (3.13), we exploited

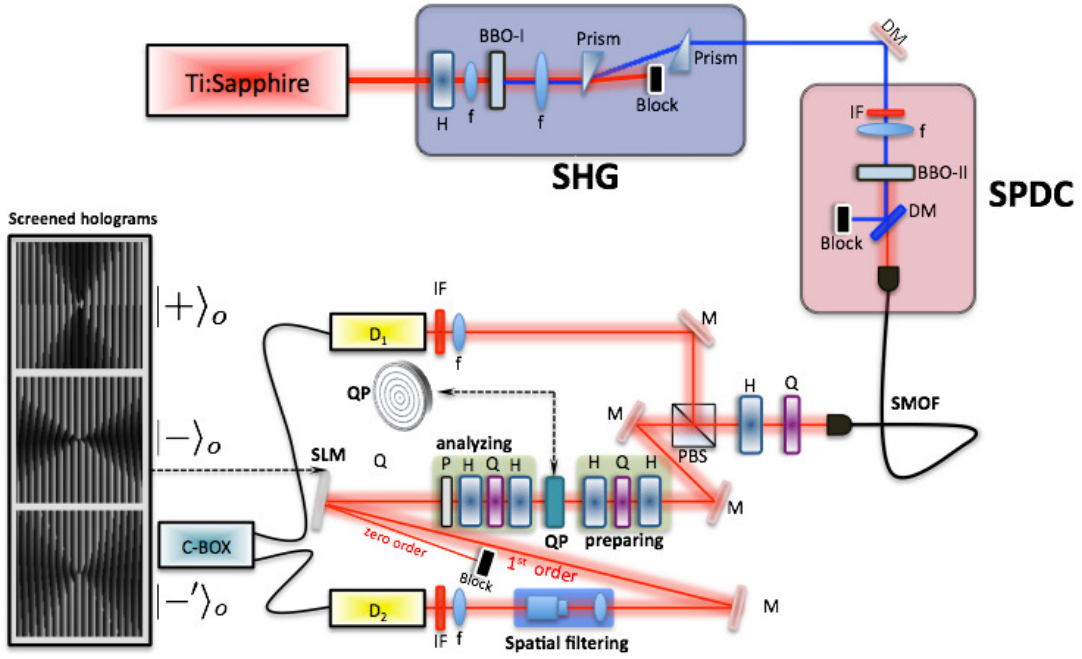

FIGURE 3.5: Experimental setup [67]. The SHG and SPDC stages are used to prepare the heralded photon used in the Hardy test and its trigger companion, as explained in the main text and in Appendix B. In the main setup, the heralded photon is prepared in a controlled polarization state and then converted into a spin-orbit partially entangled state by the q-plate. For carrying out the tomography of this state and the Hardy test, the photon was then projected (filtered) with another sequence of wave plates and a polarizer, for the polarization measurement, and by diffraction on a computer-generated hologram (hologram patterns used for filtering specific states are shown in the left inset) screened on a SLM, followed by spatial filtering in zero OAM mode and photon detection. The photon counts coming from the trigger detector (D_1) and the heralded photon one (D_2) were sent to a coincidence box, for recording the number of photon coincidences occurring in a given time window. Legend: C-BOX - coincidence box; D_i - single photon detector; DM - dichroic mirror; f - lens; H - half-wave plate; IF - bandpass interference filter; M - mirror; Q - quarter-wave plate; QP - q-plate; P - polarizer; SLM - spatial light modulator.

the spin-orbit coupling occurring in a tuned q-plate. For this purpose, we prepared the OAM part of the input photon in fundamental Gaussian mode, as obtained after passing through a single-mode fiber; the SAM part was prepared so as to have an elliptical polarization $\cos(\gamma)|R\rangle_p - \sin(\gamma)|L\rangle_p$[5]. After spin-orbit state preparation, the photon was sent to the q-plate. Starting from the q-plate action (1.60) when $\delta = \pi$, it is easy to check that at the output of the device the Hardy state (3.13) is obtained. The parameter γ, which defines the degree of entanglement in the final state, was adjusted using a sequence of birefringent wave plates: a half-wave plate, with optical axis rotated

[5]Please note that in this section we adopted the label p to refer to the SAM space, in place of the greek letter π.

at the angle $\gamma/2$ from the direction of the input polarization, a quarter-wave plate, with the axis set at $\pi/4$, and another half-wave plate at $-\pi/8$ (see Fig. 3.5).

We checked the quality of the Hardy state we prepared by carrying out a full quantum tomography (see Sec. 4.3), based on projecting (filtering) the state on a set of mutually unbiased bases in both polarization and OAM Hilbert spaces, and then using a standard maximal likelihood estimator for best fit. The polarization filtering was carried out by using a second set of birefringent wave plates followed by a polarizer. The OAM filtering was based on a standard holographic method [77], by diffracting the photons on a set of computer-generated holograms (optimized for fidelity [78, 79]) visualized on a SLM and then filtering the zero OAM component within the first-order diffracted photons. Fig. 3.6 shows the experimentally reconstructed density matrix $\widehat{\rho}_\psi = |\psi\rangle\langle\psi|$ of the generated spin-orbit state (3.13) for $\gamma = 0$, $\gamma = \pi/8$, and $\gamma = \pi/4$.

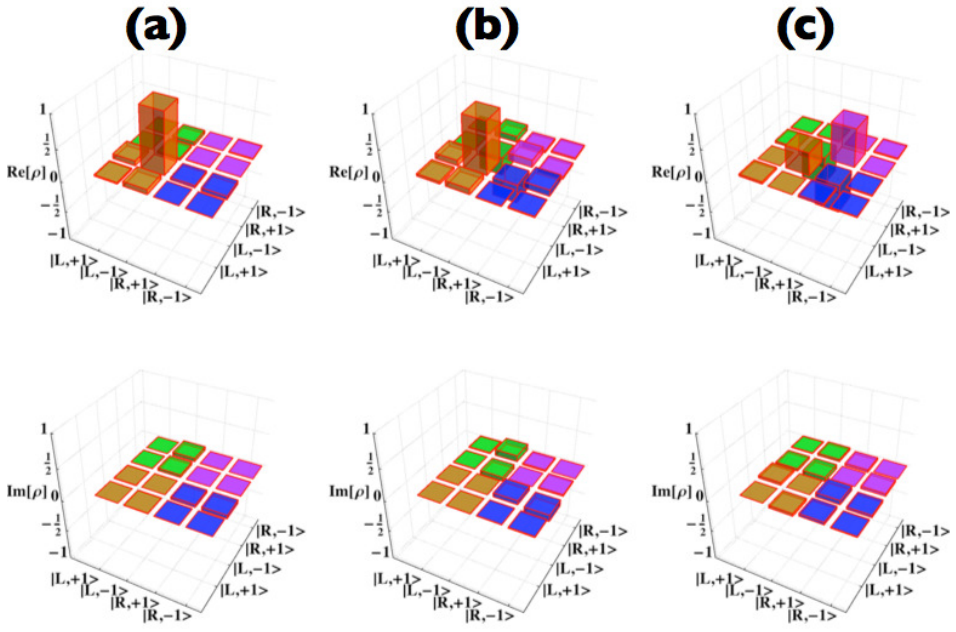

FIGURE 3.6: Experimental characterization of partially entangled spin-orbit single-photon states defined in Eq. 3.13 [67]. (a-c) Experimental reconstructed density matrix for three different values of the entanglement parameter γ: (a) $\gamma = 0$, (b) $\gamma = \pi/8$, (c) $\gamma = \pi/4$. The associated state fidelities are $F = 0.985 \pm 0.004$, $F = 0.984 \pm 0.004$, and $F = 0.956 \pm 0.005$, respectively.

For carrying out the Hardy test, we then set $\gamma = 24.9°$ in order to maximize the probability (3.16), as explained above. While heralded photons prepared in this state are sent in the main apparatus, we made a series of projective measurements of the observables S_z, Σ, Σ' in the polarization subspace and L_z, Λ, Λ' in the OAM subspace. In particular,

the probabilities of detecting specified spin-orbit states were assessed experimentally by counting the number of photon coincidences between the test photon and the trigger one in a temporal window of 100 s. We first measured the probabilities of the four spin-orbit basis states $|L\rangle_p|+1\rangle_o, |L\rangle_p|-1\rangle_o, |R\rangle_p|+1\rangle_o, |R\rangle_p|-1\rangle_o$, which are the eigenstates of $\hat{S}_z$ and $\hat{L}_z$. The results are shown in Fig. 3.7 (a) and are in reasonable agreement with the quantum predictions obtained from state (3.13). More precisely, while the counts for states $|L\rangle_p|-1\rangle_o$ and $|R\rangle_p|-1\rangle_o$ were consistent with theory within experimental uncertainties, the counts for state $|R\rangle_p|+1\rangle_o$ were about 25% smaller than theory and there was a 3% fraction of counts for state $|L\rangle_p|+1\rangle_o$, which in theory should have vanishing probability.

Next, we measured the four probabilities appearing in Eqs. P1-P4 entering Hardy's paradox, by performing a projective measurement on the four states $|+\rangle_p|+\rangle_o$, $|-'\rangle_p|-\rangle_o$, $|-\rangle_p|-'\rangle_o$, and $|-'\rangle_p|-'\rangle_o$. The experimental results are given in Fig. 3.7 (b). The count frequency of state $|-'\rangle_p|-'\rangle_o$ was found to be $(7.4 \pm 0.2)\%$ (specified errors are estimated as standard deviations computed assuming Poissonian statistics and ignoring other possible sources of errors), against a quantum prediction of 9%. The other states presented much smaller, but nonvanishing count frequencies: $(2.1 \pm 0.1)\%$, $(0.45 \pm 0.06)\%$, and $(1.0 \pm 0.1)\%$, respectively for states $|+\rangle_p|+\rangle_o, |-'\rangle_p|-\rangle_o$, and $|-\rangle_p|-'\rangle_o$. This outcome, probably due to an imperfect state preparation and/or to some residual cross-talk in the OAM and polarization measurements, makes it not possible to apply the simple all-versus-nothing reasoning presented above for Hardy's paradox. But this is normal for an experimental test, as no experimental result can be perfectly zero, because of the unavoidable noise and other experimental imperfections. To take into account experimental imperfections, one must replace the all-versus-nothing paradox with the Bell-like inequality reported in Eq. 3.18. As quantum predictions do, our results reported above violate the inequality by over seven standard deviations, thus confirming the contextual behavior of quantum mechanics.

As a conclusion, we remark that non-contextuality in our single particle experiment was assumed based on the observable compatibility, and not on their spatial separation. While this is a conceptual limitation of our test, the use of a single particle demonstrated in our approach has some other advantages. The first is that the experiment is much simpler to implement, compared to a two-particle test. We used a heralded photon regime, but a similar demonstration could be based on an attenuated light source, thus making it even simpler. Simple-to-perform experiments testing the conceptual paradoxes of quantum mechanics may have a strong educational value. A second advantage is that the quantum detection efficiency for a single-photon detection can be made significantly larger than for the two-photon case. This, in turn, could be exploited in the future to carry out Hardy-like tests that are free from other assumptions, such as the

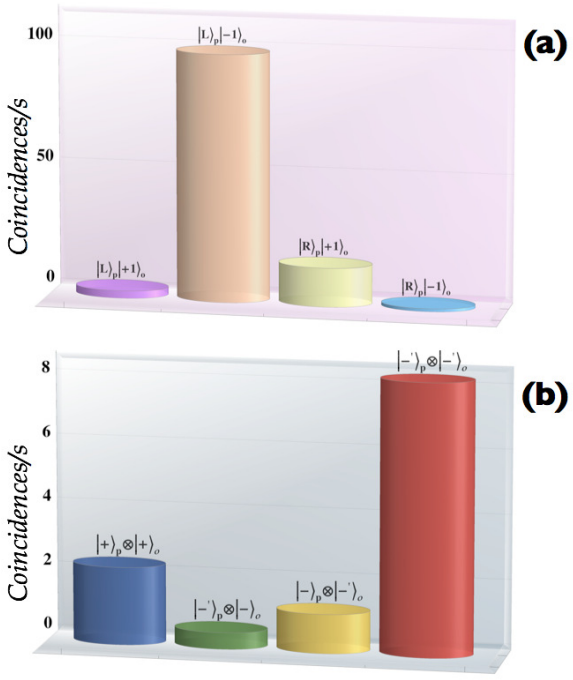

FIGURE 3.7: Experimental verification of Hardy's paradox, by using state (3.13) for the input photon with $\gamma = 24.9°$ [67]. (a) Coincidence count rates for the four spin-orbit basis states. The measurement time window was of 100 s and the mean total number of coincidences was of $N_{tot} = 12000 \pm 110$, corresponding to the rate $C_{tot} = 120.0 \pm 1.1$ coincidences/s. (b) Coincidence count rates for the measurement of spin-orbit states (3.14), which define the observables Σ, Σ', Λ, and Λ'. The ratio of the reported coincidence rate values with C_{tot} gives the experimental frequencies and the estimates of the probabilities for the photon to be in the corresponding state.

fair sampling hypothesis, or other detection-related loopholes that may undermine their validity, similarly to the case of Bell inequalities (on this issue see for instance Ref. [66]).

3.6.2 Experimental violation of Leggett inequalities[6]

Leggett inequalities provide a tool for determining the impossibility of a class of non-contextual realistic models. We tested them by measuring the quantum correlations existing between the SAM and the OAM of a single photon, when the quantum state of the latter has maximal entanglement between the two considered degrees of freedom. The layout of our experimental setup is shown in Fig. 3.8. As discussed in Appendix B, a photon pair in the polarization state $|H, V\rangle$ is generated exploiting the SPDC process in a nonlinear BBO crystal. Both photons were coupled in a single mode fiber; at the exit of the latter they were spatially separated by means of a PBS, according to their polarization. The V-polarized photon was coupled directly to an avalanche single photon detector (D_1) by an appropriate set of lenses and mirrors and was used as trigger.

[6]Some paragraphs and sentences of this section are adapted or copied verbatim from the work [80] which I coauthored.

The H-polarized photon, transmitted by the PBS, was used to perform the SAM-OAM measurements by detecting coincidences with the trigger photon, so as to operate in a heralded-single-photon quantum regime.

A tuned q-plate with topological charge $q = 1/2$ was used to prepare the spin-orbit state of the photon, which enters the setup with horizontal polarization and in the fundamental Gaussian spatial mode. After the q-plate, we obtained a maximally-entangled spin-orbit state:

$$|H\rangle_\pi|0\rangle_o \overset{q\text{-plate}}{\longrightarrow} |\Phi^+\rangle = \frac{1}{\sqrt{2}}(|L\rangle_\pi|-1\rangle_o + |R\rangle_\pi|+1\rangle_o). \tag{3.24}$$

The heralded photon prepared in the single-photon SAM-OAM entangled state $|\Phi^+\rangle$

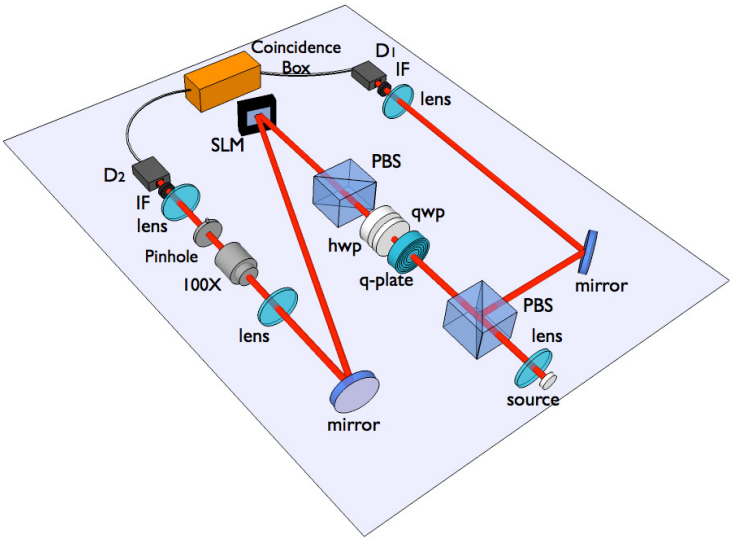

FIGURE 3.8: Experimental apparatus used for performing the Leggett test in the SAM-OAM Hilbert space of a single-photon [80]. See text for a detailed explanation of the setup workings. Legend: PBS - polarizing beam splitter; hwp - half-wave plate; qwp - quarter-wave plate; SLM - spatial light modulator; 100X - microscope objective; IF - interference filters (10 nm bandwidth); D_i - single-photon detectors.

was then sent to the detection apparatus, where its SAM and OAM values, corresponding to observables X and Y, were both measured. The projective measurement on the SAM state of the photon was singled out by means of a properly-oriented sequence of a half-wave plate, a quarter-wave plate, and a polarizer. The orientations of the two wave plates define the selected projection state **a** of the measurement, in the SAM Poincaré sphere. Then, the OAM measurement was achieved by diffraction on a spatial light modulator (SLM) followed by a spatial-filter system composed of a lens, a 100X microscope objective, and a pinhole having a 1 mm radius. The OAM projection state corresponding to each vector **b** in the OAM Poincaré sphere of $|m| = 1$ was thus determined by the hologram pattern visualized on the SLM, as was computed statically by a computer-generated-holography technique [81]. The spatial filter was used to select only the TEM_{00} Gaussian component of the diffracted beam in the far-field zone. The

selected photon, after both projections, was finally coupled to another avalanche single-photon detector D_2. The signals from the two detectors D_1 and D_2 were read out by a coincidence box and a digital counter. The experimental correlation coefficients $C(\mathbf{a}, \mathbf{b})$

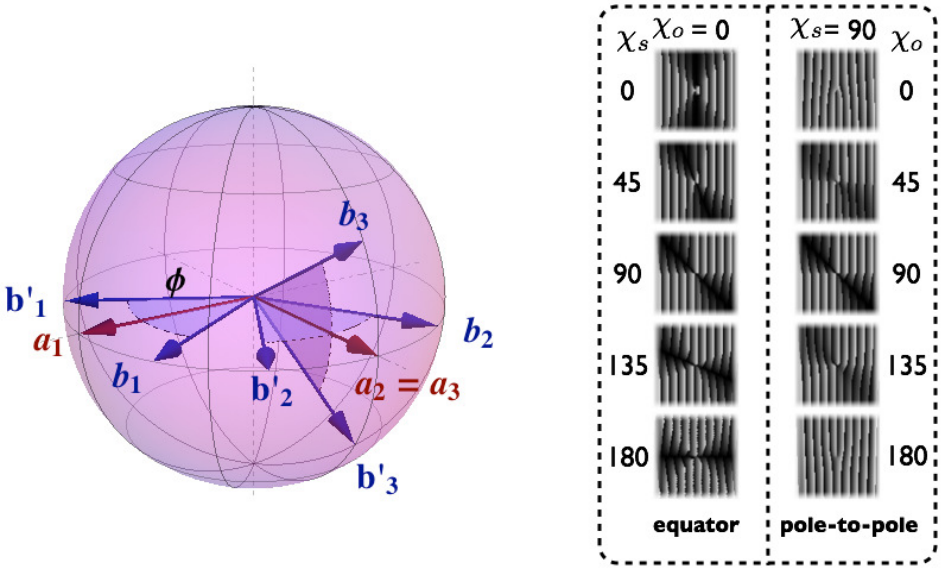

FIGURE 3.9: The set of state projections in the SAM and OAM states used to test the Leggett-type inequalities [80]. The SAM (polarization) states to be measured were taken on the Poincaré sphere equator, i.e., $\mathbf{a}_1 = |H\rangle$, $\mathbf{a}_2 = \mathbf{a}_3 = |D\rangle = (|H\rangle + |V\rangle)/\sqrt{2}$. The OAM states $\mathbf{b}_1$ and $\mathbf{b'}_1$ were also taken along the equator line, at symmetrical azimuthal angles $\pm\phi/2$ relative to $\mathbf{a}_1$. Similarly, $\mathbf{b}_2$ and $\mathbf{b'}_2$ were taken along the equator line, at symmetrical angles $\pm\phi/2$ relative to $\mathbf{a}_2$. Finally, $\mathbf{b}_3$ and $\mathbf{b'}_3$ were taken along a meridian line, at symmetrical polar angles $\pm\phi/2$ relative to $\mathbf{a}_3 = \mathbf{a}_2$. Examples of the computer-generated holograms needed to measure these OAM states are shown in the right inset, with χ_o and χ_s representing the polar and azimuthal angles (in degrees) on the OAM Poincaré sphere, respectively.

between the measurements of SAM and OAM were computed as

$$C(\mathbf{a}, \mathbf{b}) = \frac{N(\mathbf{a}, \mathbf{b}) + N(-\mathbf{a}, -\mathbf{b}) - N(\mathbf{a}, -\mathbf{b}) - N(-\mathbf{a}, \mathbf{b})}{N(\mathbf{a}, \mathbf{b}) + N(-\mathbf{a}, -\mathbf{b}) + N(\mathbf{a}, -\mathbf{b}) + N(-\mathbf{a}, \mathbf{b})}, \tag{3.25}$$

where $N(\mathbf{a}, \mathbf{b})$ are the experimental coincidence counts between the detectors D_1 and D_2 when the SAM and OAM projections are set to $\mathbf{a}$ and $\mathbf{b}$, respectively [65].

For the Leggett test, the adopted geometry of measurement settings $\mathbf{a}_i$, $\mathbf{b}_i$, and $\mathbf{b'}_i$ is shown in Fig. 3.9, together with some representative holograms used to measure the OAM states.

Figure 3.10 shows the experimental $E_3(\phi)$ data, as based on the measured correlation coefficients, for an angle ϕ varying within the range (0° - 180°), in steps of 4°. The experimental data (blue points) are in good agreement with the predictions of quantum mechanics (violet dashed line), with only a small loss of visibility due to experimental imperfections. For a specific region, i.e., $8° \leq \phi \leq 52°$, we obtained a violation of the

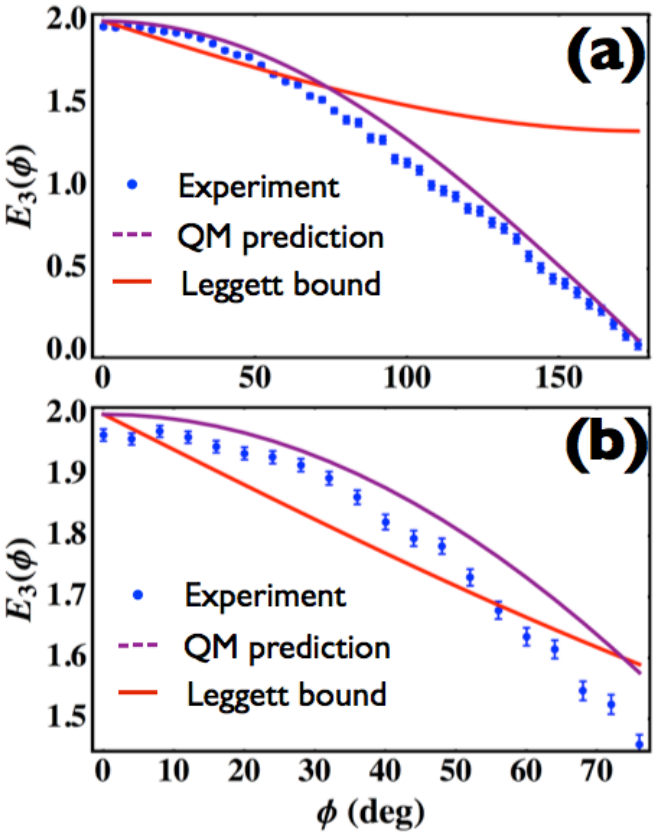

FIGURE 3.10: Experimental and theoretical values of Leggett's function $E_3(\phi)$ [80]. The blue points are the experimental data. Error bars are derived from Poissonian statistics on the coincidence counts and correspond to one standard deviation. The violet dashed line is the quantum mechanics prediction for the same function. The solid red line is the Leggett's bound $L_3(\phi)$. Panel (a) shows the entire range of measurement, $\phi \in [0, 180°]$. Panel (b) is a zoomed-in plot of the region in which a violation of the Leggett's bound is observed, i.e., $8° \leq \phi \leq 52°$.

Leggett bound. The maximum violation is found for $\phi = 28°$ and it is equal to 7.4σ, where σ is a standard deviation.

Chapter 4

Realization of mutually unbiased bases for a six-dimensional photonic quantum system

4.1 Introduction [1]

The complementarity between different observables is a key element in quantum sciences, as for instance in areas like quantum state reconstruction [82] and quantum key distribution [83]. Quantum theory describes these observables in terms of non-commuting hermitian operators, whose eigenstates are all pairwise unbiased. Reflecting this feature, sets of eigenstates of complementary observables are referred to as mutually unbiased bases (MUBs).

In high-dimensional systems, complementary observables and the corresponding MUBs have been exploited to enhance the security in quantum cryptograpy [84], perform fundamental tests of quantum mechanics, such as quantum contextuality [85–87], explore logical indeterminacy [88], and many other tasks in quantum information. For example, new QKD protocols have been proposed in which a larger error rate can be tolerated while preserving security [89, 90]. Moreover a different protocol extending Ekert91 [91] by using entangled qutrits has been experimentally realized [92]. In quantum state tomography, MUBs play a crucial role because they correspond to the optimal choice of the measurements to be performed in order to obtain a full reconstruction of the density matrix. In this framework, an important problem is the determination of the maximum number of MUBs which can be defined simultaneously for a given d-dimensional Hilbert

[1] Some paragraphs and sentences of this section are adapted or copied verbatim from the work [79] which I coauthored

space. Hitherto, this problem has been solved only for specific cases, corresponding to d being a prime number or a power of a prime number. For these systems, $d+1$ MUBs can be defined at the same time. On the other hand, there is a strong numerical evidence that such result does not hold for generic systems, even though a mathematical demonstration is still missing.

Different experimental approaches have been recently adopted to implement complete sets of MUBs for state reconstruction in photonic systems. For example, the polarization of a photon pair was used to define MUBs in dimension four [93]. The orbital angular momentum (OAM) of single photons has been used to address Hilbert spaces with $d = 2, 3, 4, 5$ [94] and multiple propagation modes were combined to reach dimensions $d = 7, 8$ [95]. Hybrid methods combining polarization and OAM were also used to define and manipulate photonic ququarts ($d = 4$) [96]. However, since in $d = 6$ no complete set of MUBs is known, this case has not been investigated hitherto for state tomography and even the minimal set of three MUBs has never been demonstrated in an experimental framework.

In this chapter we report the implementation of the minimal set of MUBs in a six-dimensional (6D) photonic quantum system, following two different approaches. In the first one, we considered the 6D Hilbert space as the product of a two-dimensional (2D) and a three-dimensional (3D) space. Accordingly, these spaces can be encoded in the polarization and the OAM degrees of freedom, respectively, if considering for the OAM the subspace generated by helical modes $|-1\rangle$, $|0\rangle$ and $|+1\rangle$. In our second experiment, we prepared and characterized the three 6D MUBs exploiting pure OAM states of a single photon. To generate complex superposition of helical modes, a novel holographic technique was developed, which allows the exact generation of arbitrary optical fields. As a difference with respect to previous techniques, this provides a high fidelity in the state generation, which was crucial to guarantee an effective uniform overlap between states in different MUBs. The approach introduced in this work can be easily extended to higher dimensional spaces, where the generation and the accurate control of maximal sets of MUBs is a very demanding task.

4.2 Mutually unbiased bases for six-dimensional systems[2]

In a d-dimensional Hilbert space H_d we can consider two observables A and B. The associated eigenstates $\{|a_i\rangle\}$ and $\{|b_i\rangle\}$, with $i \in \{0, 1, ..., d-1\}$, are two possible basis

[2]Some paragraphs and sentences of this section are adapted or copied verbatim from the work [79] which I coauthored

for H_d; they are said to be mutually unbiased if

$$|\langle b_j|a_i\rangle|^2 = \frac{1}{d}, \qquad \forall i,j \in \{0,1,...,d-1\}\,. \tag{4.1}$$

It is possible to show that such a pair of MUBs always exists; indeed let us identify eigenstates $|a_i\rangle$ with the computational basis

$$\{|a_i\rangle\} = \{|0\rangle, |1\rangle, ..., |d-1\rangle\}\,; \tag{4.2}$$

the dual basis obtained by discrete Fourier transform

$$|b_i\rangle = \frac{1}{\sqrt{d}} \sum_{j=0}^{d-1} \omega_d^{ij} |a_j\rangle \tag{4.3}$$

is mutually unbiased to the previous one. In Eq. 4.3 $\omega_d = \exp(\mathrm{i}2\pi/d)$, and the non-italic i denotes the imaginary unit (not to be confused with the index i). The operators associated with these specific basis provides an algebraic complete set that fully parametrizes the physical degree of freedom described by the Hilbert space: all other operators acting on this space are product of powers of $\hat{A}$ and $\hat{B}$ [97].

When $d = n^p$, with n prime number and p a positive integer, $d+1$ MUBs can be defined simultaneously and can be found using several methods, that is the Galois Field, the Heisenberg-Weyl group, Hadamard matrices, etc. (for a review see [97, 98]). These sets of MUBs are said to be complete, since as we will see below they provide the minimum number of projective measurements for determining a quantum state in H_d. In the general case of composite dimensions that are not prime powers, such as $d = 6, 10, 12, ...$, all previous methods fail [99]. On the base of extensive numerical simulations, it has been conjectured that complete sets of MUBs do not exist in this case [100], although this conjecture hitherto has not been rigorously proved. A minimum number of MUBs that is known to exist in such cases is given by $p^k + 1$, where p^k is the lowest factor in the prime decomposition of the number d [101]. For instance, in the $d = 6$ case, three MUBs can be easily constructed, but no evidence for the existence of a fourth basis that is unbiased with the first three has ever been found.

In the remaining part of this section, we will focus our attention on a 6D Hilbert space. For this space, three MUBs can be easily found decomposing the space in the product of 2D and 3D spaces, that is $H_6 = H_2 \otimes H_3$. We know that for both subspaces a complete set exists, made of three and four bases, respectively. We refer to the corresponding states as $|m_i^\alpha\rangle$ and $|n_j^\beta\rangle$; here indices $i \in \{1,2\}$, $j \in \{1,2,3\}$ label different states in each basis, while $\alpha \in \{1,2,3\}$, $\beta \in \{1,2,3,4\}$ label different bases in the subspaces H_2 and H_3, respectively. By combination of these states we obtain twelve bases for the global space H_6, but a maximum of three bases can be found to be mutually unbiased. A

possible choice is given by the following three bases:

$$\begin{aligned} I &= \{|m_i^1\rangle \otimes |n_j^1\rangle\} \\ II &= \{|m_i^2\rangle \otimes |n_j^2\rangle\} \\ III &= \{|m_i^3\rangle \otimes |n_j^3\rangle\} \end{aligned} \tag{4.4}$$

It can be immediately seen that any other combination obtained introducing the fourth basis $\left\{|n_j^4\rangle\right\}$ of H_3 would not be mutually unbiased with the others, since it is missing a different basis in H_2. This set of 18 product states cannot be extended by any other vector in H_6, even if entangled states are considered [102]; moreover if a complete MUBs set in $d = 6$ existed, then only one among the seven bases therein could be composed of product states, while all others must be entangled [103].
States $|m_i^\alpha\rangle$ and $|n_j^\beta\rangle$ can be directly calculated as the eigenstates of the matrices reported in Appendix C. We will provide their explicit expression when discussing our scheme to realize these 6D MUBs in a photonic system.

4.3 Quantum state tomography

Quantum state reconstruction, or quantum state tomography (QST), consists in the determination of the quantum state of an ensemble of many identical particles (or more complex physical systems). In this context, MUBs are a fundamental resource since projective measurements over states belonging to a set of MUBs may represent an optimal choice in QST. In the most generic quantum scenario, which includes the possibility of statistical mixtures, the state of a system is described by the density operator $\widehat{\rho}$, which for pure states is equal to

$$\widehat{\rho} = |\psi\rangle\langle\psi| \tag{4.5}$$

Assigning a specific basis in a Hilbert space H_d, the density operator can be expressed as a $d \times d$ complex matrix $\rho_{i,j}$. Associated eigenvalues λ_j represent the probabilities that the system can be found in each of the corresponding eigenstates; accordingly they are semi-positive real numbers verifying the property

$$0 \leq \lambda_j \leq 1 \tag{4.6}$$

Mathematically, in order to have $\lambda_j \in R$ and to verify the normalization of these probabilities, the matrix ρ is required to be hermitian, while its trace has to be equal to

one:

$$\rho_{i,j} = \rho^*_{j,i} \tag{4.7}$$

$$\mathrm{Tr}\,\rho = \sum_{i=0}^{d-1} \rho_{i,i} = 1 \tag{4.8}$$

As a consequence of Eqs. 4.7-4.8, among the $2\,d^2$ real coefficients which define a density matrix, only $d^2 - 1$ are independent. The aim of QST is the determination of such parameters, starting from the outcome of an ensemble of measurements.

A basic approach to QST consists in the formulation of a system of $d^2 - 1$ equations, where the variables to be determined are the independent coefficients in ρ. Such equations are given in terms of the results of projective measurements, operated on a set of $d^2 - 1$ states. As we have seen previously, only for specify dimensions this set of states may correspond to a maximal set of MUBs. Interestingly, for these Hilbert spaces, MUBs are an optimal choice since they provide the minimum number of states for the required projective measurements, and at the same time they optimize the accuracy in the estimation of the matrix parameters. When realizing projective measurements for QST on an ensemble of identical particles, the choice of the states for projections influences the accuracy of the obtained results. Optimal strategies correspond to sampling the Hilbert space uniformly; in this sense, MUBs can play a key role since the associated states are distributed over the whole Hilbert space.

To make the concept of QST clear, and to introduce the technique we exploit in our experiments, we provide a simple and standard example. Let us consider the polarization of a single photon, which can be described in terms of a 2×2 density matrix; this can be written in terms of the reduced Stokes parameters introduced in Sec. 1.3

$$\rho = \frac{1}{2}\begin{pmatrix} 1 + s_3 & s_1 - is_2 \\ s_1 + is_2 & 1 - s_3 \end{pmatrix} \tag{4.9}$$

Reduced Stokes parameters are three normalized real numbers, that we can use to determine the three independent parameters in ρ. Nevertheless, to determine them in an experiment, we have to measure to four quantities S_0, S_1, S_2, S_3. A fourth measurement is needed in order to obtain matrix parameters which verify the normalization condition $\mathrm{Tr}\,\rho = 1$.

It is simple to understand that if we include the possibility of experimental imperfections, it can happen that the matrix we determine from Eq. 4.9 does not verify all requirements reported in Eqs. 4.7, 4.8. In our experiments, in order to avoid the possibility of determining "illegal" density matrices, we adopt a different strategy relying on a statistical approach introduced by James *et. al.* [104]. We start by defining a triangular matrix

$T(\vec{\mathbf{t}})$, in terms of four real parameters $\vec{\mathbf{t}} = \{t_1, t_2, t_3, t_4\}$

$$T = \begin{pmatrix} t_1 & 0 \\ t_3 + i\, t_4 & t_2 \end{pmatrix} \tag{4.10}$$

The matrix ρ obtained as

$$\rho = \frac{TT^\dagger}{\mathrm{Tr}(TT^\dagger)} \tag{4.11}$$

verifies Eqs. 4.6-4.8, thus it corresponds to a legal parametrization of a density matrix in terms of parameters $\vec{\mathbf{t}}$. In order to determine these numbers, we consider the operators $\widehat{M_j} = |\psi_j\rangle\langle\psi_j|$, defining projective measurements over states $|\psi_j\rangle$. Photons passing through a set of wave plates and a polarizer, oriented so as to implement the projector M_j, are sent to a detector; we label the associated photon counts as $\bar{n}_j$. On the other hand, we define the expected photon counts as

$$n_j = \mathrm{Tr}(TT^\dagger\, \widehat{M_j}) \tag{4.12}$$

assuming for the time being a density matrix which is not normalized ($\mathrm{Tr}(TT^\dagger) \neq 1$). The probability that we get the result $\bar{n}_j$ when measuring M_j depends on the parameters $\vec{\mathbf{t}}$, and it is proportional to

$$\exp\left[-\frac{(\bar{n}_j - n_j)^2}{2\sigma_j^2}\right] \tag{4.13}$$

where σ_j is the standard deviation associated with the quantity $\bar{n}_j$; typically this is equal to $\sqrt{\bar{n}_j}$. The total probability of obtaining the results $\{\bar{n}_j\}$, with $j = \{0, 1, ..., k\}$, is given by

$$P = \frac{1}{N}\prod_{j=0}^{k} \exp\left[-\frac{(\bar{n}_j - n_j)^2}{2\sigma_j^2}\right] \tag{4.14}$$

where N is a normalization factor; here we are assuming that all detectors and measurement settings are affected by the same detection efficiency. The parameters $\vec{\mathbf{t}}$ are determined so as to maximize the probability 4.14, which is equivalent to minimize the likelihood function

$$L(\vec{\mathbf{t}}) = \sum_{j=0}^{k} \exp\left[-\frac{(\bar{n}_j - n_j)^2}{2\bar{n}_j}\right] \tag{4.15}$$

The minimization of the function $L(\vec{\mathbf{t}})$ is achieved by exploiting dedicated routines; in our case, we use a standard minimization routine provided by *Mathematica*, by Wolfram

Research. Once the parameters $\vec{\mathbf{t}}$ are determined, the density matrix is recovered using Eq.4.12. In order to implement this "maximum likelihood technique", we need to perform k projective measurements, where we have seen that $k \geq d^2$. In place of MUBs, overcomplete sets of states can be used, as we did for example in the experiment we discuss below.

The technique we described can be generalized to Hilbert spaces of arbitrary dimensions, by considering an adequate number of parameters t_j. In real experiments, projective measurements can be characterized by many imperfections; when these are identified, they can be taken into account in order to get an accurate QST. A detailed pedagogical discussion about the QST of a polarization qu-bit which takes into account experimental imperfections can be found in Ref. [105].

4.4 Encoding OAM states exploiting a high fidelity holographic technique

Our scheme for the realization of MUBs in a 6D system relies on encoding the quantum information in 3D or 6D OAM spaces of a single photon. To this end, we need to be able to prepare single photon states which are superpositions of three or six helical modes, respectively, corresponding to complex light beams. It is well known that optical beams with an arbitrary field distribution can be generated by means of diffraction on a Spatial Light Modulator (SLM), whose screen displays a "kinoform" introducing a specific phase profile. In the very general case, to obtain a particular field distribution from a plane wave, it is required a manipulation of both phase and amplitude of the impinging wave; but how can this be achieved relying on a device that can uniquely change the phase of a beam, as most SLMs do? Several possibilities exist, all based on tailoring the contrast in the fringes of the kinoform, thus modulating at each point in the transverse plane the amount of light which is diffracted at the first order. Existing methods provide good results for many applications, but do not work properly in our case where a high fidelity is needed in the generation of the desired state.

Given the optical field $A^{e^{i\phi}}$, we may consider a kinoform introducing the phase factor [78, 79]

$$M = \mathrm{Mod}\left[\left(\phi - \pi\, I + \frac{2\pi x}{\Lambda}\right), 2\pi\right] I \tag{4.16}$$

where Λ is the grating period and fixes the diffraction angle, while

$$I = \left[1 + (1/\pi)\mathrm{sinc}^{-1}(A)\right]. \tag{4.17}$$

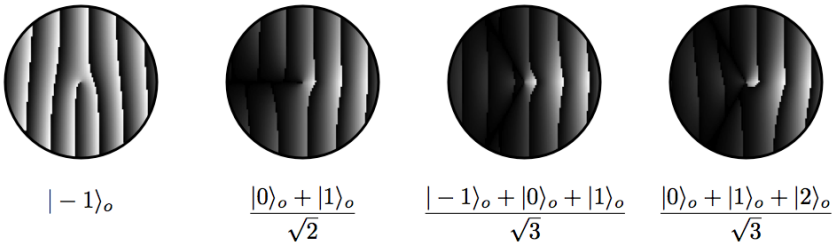

FIGURE 4.1: Kinoforms for the generation of complex optical fields, as calculated using Eq. 4.16. The optical fields we have considered are superposition of helical modes, neglecting the radial dependance. At the first diffraction order, a plane wave (or equivalently a Gaussian beam) is converted into the state reported below the corresponding hologram.

Here sinc^{-1} is the inverse of the sinc function $\mathrm{sinc}\, x = \sin x/x$, and Mod is the function that gives the reminder from division of the first argument by the second. Exact calculations [78] show that when a plane wave is impinging on a SLM displaying the kinoform reported in Eq. 4.16, in the far field in the first diffraction order the field $A\, e^{i\phi}$ is generated. This result is exact (no approximations were considered in its derivation), thus the fidelity is in principle equal to 100%; in every experiment lower values are obtained depending on the quality of the spatial light modulator and on its resolution, since the theoretical analysis refers to the ideal case of infinite pixels. The price we pay to achieve a high fidelity in the state preparation is a lower diffraction efficiency with respect to other existing methods. In Fig. 4.1 we report some holograms calculated for the generation of superposition of two and three helical modes, as described in the caption of the figure.

Eq. 4.16 represents a very important result since it allows one to prepare complex OAM states, characterized by a high fidelity; these features have been exploited recently for the quantum simulation of wave packets dynamics in a Quantum Walk [106](see Ch. 5).

4.5 Generation and characterization of hybrid MUBs combining SAM and OAM of single photons[3]

The first strategy we adopted to generate a 6D quantum system consisted in the hybrid combination of a 2D space and a 3D space, corresponding to the SAM and the OAM space of single photons. In particular, the 3D space is obtained from the superposition of three OAM modes $\{|-1\rangle, |0\rangle, |1\rangle\}$. Indeed, as discussed in Sec. 4.2, a possible route

[3]Some paragraphs and sentences of this section are adapted or copied verbatim from the work [79] which I coauthored

to construct three MUBs in H_6 is to consider products of MUBs for H_2 and H_3. In the SAM space, we considered the three bases $\Pi_1 = \{|H\rangle, |V\rangle\}$, $\Pi_2 = \{|A\rangle, |D\rangle\}$ and $\Pi_3 = \{|L\rangle, |R\rangle\}$. In the OAM space, we have four MUBs, $\mathcal{O}_1 = \{|+1\rangle, |0\rangle, |-1\rangle\}$, $\mathcal{O}_2 = \{|\alpha_1\rangle, |\alpha_2\rangle, |\alpha_3\rangle\}$, $\mathcal{O}_3 = \{|\beta_1\rangle, |\beta_2\rangle, |\beta_3\rangle\}$, and $\mathcal{O}_4 = \{|\gamma_1\rangle, |\gamma_2\rangle, |\gamma_3\rangle\}$. States introduced in the four OAM bases are defined as follows

$$
\begin{aligned}
|\alpha_1\rangle &= (|-1\rangle + |0\rangle + |1\rangle)/\sqrt{3} \\
|\alpha_2\rangle &= (|-1\rangle + \omega|0\rangle + \omega^2|+1\rangle)/\sqrt{3} \\
|\alpha_3\rangle &= (|-1\rangle + \omega^2|0\rangle + \omega|+1\rangle)/\sqrt{3} \\
|\beta_1\rangle &= (|-1\rangle + \omega|0\rangle + \omega|1\rangle)/\sqrt{3} \\
|\beta_2\rangle &= (|-1\rangle + \omega^2|0\rangle + |+1\rangle)/\sqrt{3} \\
|\beta_3\rangle &= (|-1\rangle + |0\rangle + \omega^2|+1\rangle)/\sqrt{3} \\
|\gamma_1\rangle &= (|-1\rangle + \omega^2|0\rangle + \omega^2|1\rangle)/\sqrt{3} \\
|\gamma_2\rangle &= (|-1\rangle + \omega|0\rangle + |+1\rangle)/\sqrt{3} \\
|\gamma_3\rangle &= (|-1\rangle + |0\rangle + \omega|+1\rangle)/\sqrt{3}
\end{aligned}
\tag{4.18}
$$

where $\omega = \omega_3 = e^{i\,2\pi/3}$. Combining SAM and OAM bases we obtained a set of three MUBs for the 6D space, defined as $I = \Pi_1 \otimes \mathcal{O}_1$, $II = \Pi_2 \otimes \mathcal{O}_2$ and $III = \Pi_3 \otimes \mathcal{O}_3$. The intensity and phase profiles of the nine OAM states belonging to these three MUBs are shown in Fig. 4.2. The preparation of SAM states is achieved by means of a set of wave plates, which are suitably oriented. In order to tailor the OAM part, we exploited the holographic technique introduced in Sec. 4.4. Accordingly, we calculated the kinoforms needed to generate the nine OAM states of the first three MUBs. The resulting hologram patterns are shown in Fig. 4.2. It can be seen that these kinoforms include only an azimuthal dependence, since the OAM state definition ignores the radial coordinate. This implies that the same holograms can also be used with a Gaussian input beam instead of a plane wave and only the radial profile of the diffracted wave will be affected, while the OAM state will remain the same. Moreover, we do not need to finely adjust the input beam waist of the Gaussian beam.

We remark that the holograms defined by Eq. 4.16 generate ideally exact modes in the far field, so that the expected overlap between states belonging to the same basis vanishes identically and that between states belonging to different MUBs is 1/3 in the qutrit space (and hence it will be 1/6 in the qusix space, after combining with polarization). As mentioned, this is not the case for other commonly used holographic methods (see [78, 79] for a quantitative analysis). In order to experimentally generate these hybrid qusix states we employed the setup shown in Fig. 4.3. Relying on an architecture similar to that introduced in Appendix B, we realized a single photon source operating in the heralded regime (this part of the setup is not shown in the figure). Single photons

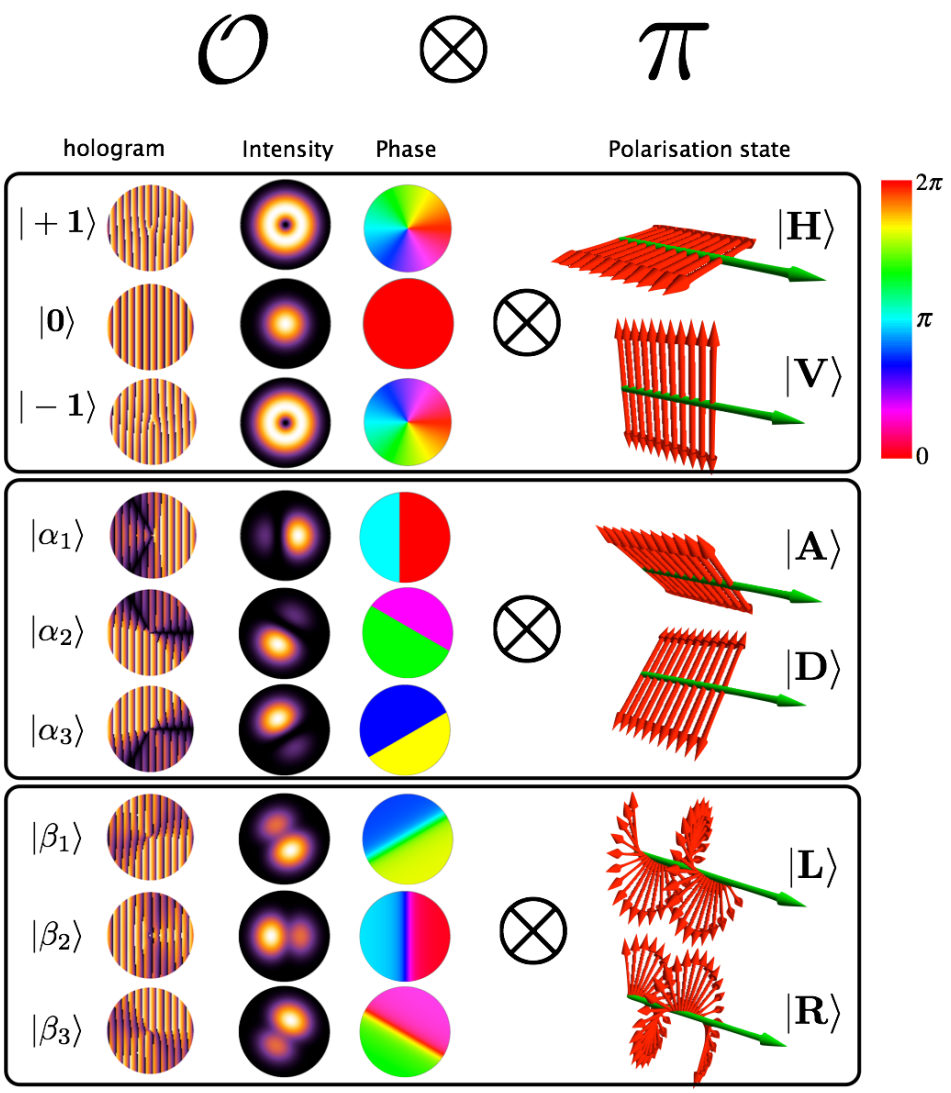

FIGURE 4.2: MUBs for hybrid photonic qusix encoding. Representation of quantum states with dimension $d = 6$ obtained from the direct product of a three-dimensional subspace $\mathcal{O}$ of OAM and the two-dimensional space π of polarization. The three main boxes correspond to the three MUBs. On the left side, the intensity and phase distributions of each OAM spatial mode and the corresponding generating kinoform are shown. On the right side the polarization states are illustrated graphically by showing the optical electric field orientation in space at a given time.

enter the setup shown in Fig. 4.3 after propagating in a single-mode fiber (SM) to filter out all the spatial modes but the Gaussian mode TEM_{00}, i.e., OAM state $|0\rangle$ (OAM qutrit initialization). A set of waveplates (C) compensates the polarization after the transmission through the fiber. The photons are then sent through a polarizing beam splitter (PBS) (polarization qubit initialization) and, after adjusting the beam radial size by a pair of lenses (MA), to a first reflecting spatial light modulator (SLM1) which generates the desired OAM qutrit state. The hologram kinoform displayed on the SLM1 for each OAM state to be generated, in the first-order diffraction, is shown in Fig. 4.2. After SLM1, a HWP and a (QWP) are used to write the polarization qubit in the

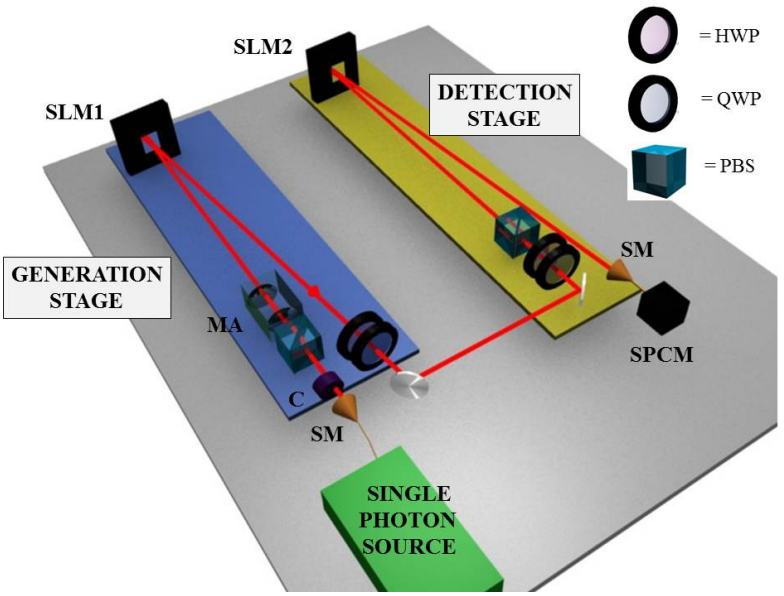

FIGURE 4.3: Sketch of experimental setup for generating and testing photonic MUBs in dimension six [79]. The polarization state is controlled by suitable sequences of wave plates, while the OAM mode is controlled by SLMs and single-mode fibers. Legend: SM - single-mode fiber; C - polarization compensation waveplates; HWP - half-wave plate; QWP - quarter-wave plate; MA - radial mode adjustment lens set; SLM - spatial light modulator; SPCM - single-photon counter module.

photon. Hence we are able to generate any hybrid qusix that is a product of a qutrit and a qubit.

The qusix-carrying photon is then sent to the detection stage. This stage is composed of a polarization analysis set (HWP, QWP and a PBS) and a second spatial light modulator (SLM2) for converting in diffraction the OAM state to be detected back into a Gaussian mode. The photon is finally coupled to a single mode fiber, to filter only this Gaussian mode, connected to a single-photon counter module (SPCM). To eliminate the Gouy phase-shift effects between different OAM eigenstates occurring in free propagation, an imaging system (not shown in the figure) has been included to image the screen of SLM1 onto the SLM2. All waveplates and SLMs were computer-controlled so as to allow for a fully automatic generation and measurement procedure. With this setup, it is possible to perform a projective measurement upon every possible separable state of polarization and OAM.

As a first test, we verified the MUBs properties by generating each qusix $|\psi_i\rangle$ among the 18 states of the MUBs and then projecting it onto all the 18 states $|\psi_j\rangle$. Figure 4.4 shows the resulting measured probability distribution $P_{ij} = |\langle\psi_j|\psi_i\rangle|^2$, compared to the theoretical one P'_{ij}. For a quantitative comparison, we used the similarity parameter $S = \frac{\left(\sum_{i,j}\sqrt{P_{ij}P'_{ij}}\right)^2}{\sum_{i,j}P_{ij}\sum_{i,j}P'_{ij}}$, which is a natural generalization of the fidelity used to compare two wavefunctions, finding $S = (99.19 \pm 0.04)\%$. As a second check of the quality of our

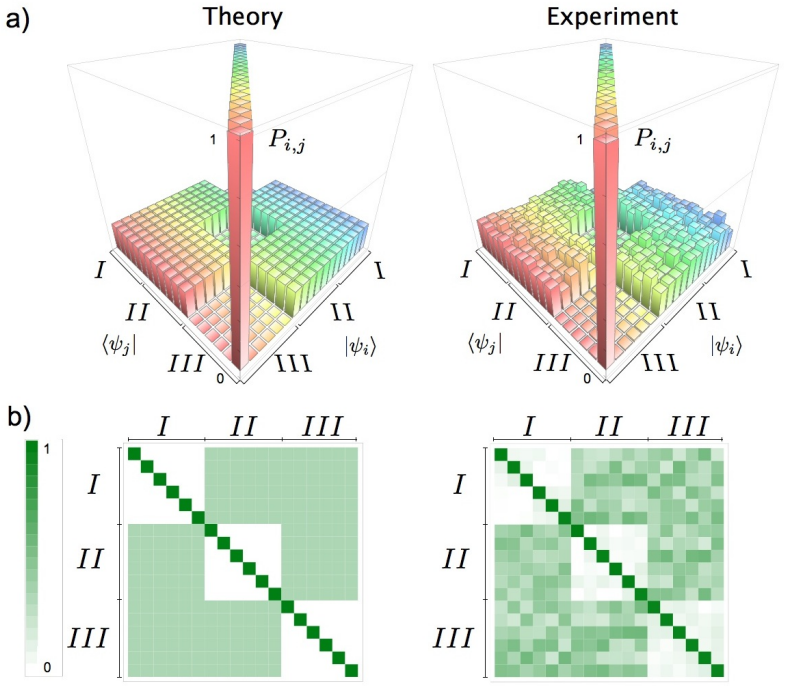

FIGURE 4.4: Experimental analysis of hybrid qusix photonic states [79]. Probability distribution resulting from all 18×18 projections of each state within the three MUBs over all the others, comparing theoretical and experimental values. According to theoretical predictions, we expect that the 18×18 matrix can be divided into nine 6×6 blocks A_n^m, where the two indices $m, n \in$ {I,II,III} label generation and detection bases, respectively. Blocks that correspond to projection of one basis over itself ($m = n$) should be diagonal, i.e., $(A_m^m)_{i,j} = \delta_{ij}$. Other blocks, whose values represent the overlap between states belonging to two different bases, should be flat, i.e., $(A_n^m)_{i,j} = 1/6$, for $m \neq n$.

hybrid qusix states, we reconstructed the density matrix of all the 18 states by quantum state tomography, exploiting the maximum likelihood technique illustrated in Sec. 4.3. Since we lack a complete set of MUBs in dimension six, we performed measurements in all possible product states obtained combining the three MUBs of the polarization space Π and the four MUBs in the OAM space $\mathcal{O}$, for a total of 72 projections. In Table 4.1, the resulting experimental fidelities of the 18 MUBs states are reported. The overall mean fidelity was $\bar{F} = (98.51 \pm 0.04)\%$. Moreover, Figure 4.5 shows the reconstructed density matrices compared to the theoretical ones for three representative qusix states, one for each MUB considered here.

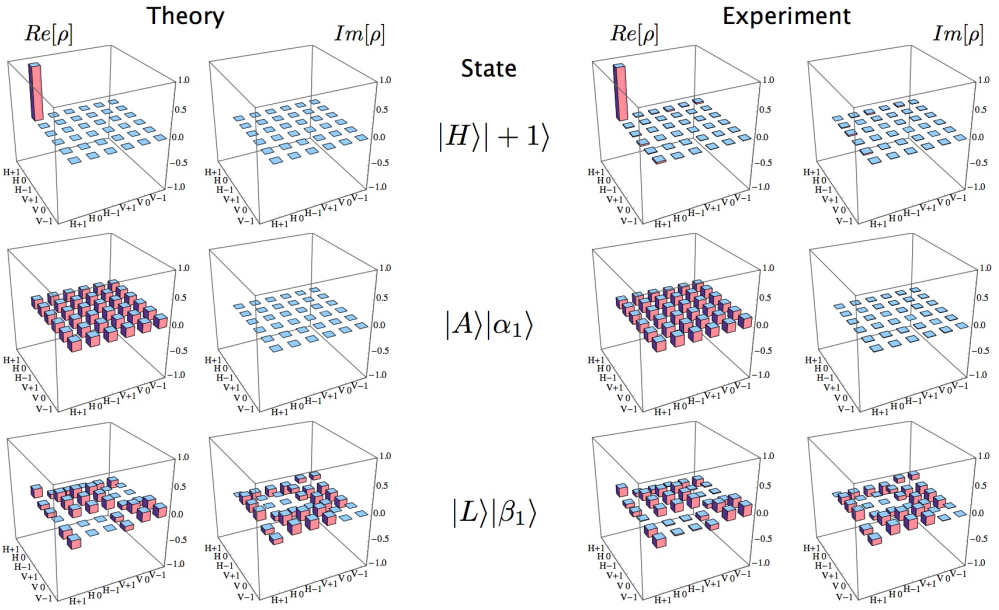

FIGURE 4.5: Quantum tomography of hybrid qusix photonic states [79]. Density matrices associated with states of each of the three MUBs have been fully reconstructed by projections over all the 72 states obtained by direct product of the three MUBs of the 2D polarization space Π and the four ones of the 3D OAM subspace $\mathcal{O}$. Here we show one state for each MUB. Experimental and theoretical matrices are reported for comparison.

4.6 Generation and characterization MUBs exploiting pure OAM modes of single photons[4]

In our second experiment, we implemented qusix photonic states using pure OAM modes, not taking into account the polarization degree of freedom. Although the hybrid approach may offer advantages for certain specific tasks [29], an encoding in OAM is in principle suitable of extension to arbitrary dimensionality and enables the generation of any kind of state, including the entangled ones which, for hybrid encoding, would need a more complex experimental setup. The 6D Hilbert space is realized exploiting OAM eigenstates as logical basis:

$$I = \{|-3\rangle, |-2\rangle, |-1\rangle, |1\rangle, |2\rangle, |3\rangle\}. \tag{4.19}$$

The three MUBs were still defined starting from the tensor products of a 2D and a 3D spaces, as in the hybrid case. This time the decomposition of the 6D space is not physical, since the two spaces do not correspond to different degrees of freedom. More details about the resulting states of the three bases I, II, III are given in Appendix C.

[4]Some paragraphs and sentences of this section are adapted or copied verbatim from the work [79] which I coauthored

Basis	**State**	**Fidelity**
I	$\|H\rangle\|+1\rangle$	0.986 ± 0.002
	$\|H\rangle\|0\rangle$	0.982 ± 0.002
	$\|H\rangle\|-1\rangle$	0.986 ± 0.002
	$\|V\rangle\|+1\rangle$	0.988 ± 0.002
	$\|V\rangle\|0\rangle$	0.980 ± 0.002
	$\|V\rangle\|-1\rangle$	0.983 ± 0.002
II	$\|A\rangle\|\alpha_1\rangle$	0.989 ± 0.001
	$\|A\rangle\|\alpha_2\rangle$	0.981 ± 0.002
	$\|A\rangle\|\alpha_3\rangle$	0.986 ± 0.002
	$\|D\rangle\|\alpha_1\rangle$	0.989 ± 0.001
	$\|D\rangle\|\alpha_2\rangle$	0.982 ± 0.002
	$\|D\rangle\|\alpha_3\rangle$	0.980 ± 0.002
III	$\|L\rangle\|\beta_1\rangle$	0.981 ± 0.002
	$\|L\rangle\|\beta_2\rangle$	0.981 ± 0.002
	$\|L\rangle\|\beta_3\rangle$	0.979 ± 0.002
	$\|R\rangle\|\beta_1\rangle$	0.977 ± 0.002
	$\|R\rangle\|\beta_2\rangle$	0.972 ± 0.002
	$\|R\rangle\|\beta_3\rangle$	0.970 ± 0.002
	Average Fidelity	0.9851 ± 0.0004

TABLE 4.1: Experimental fidelities measured for all 18 qusix hybrid states that characterize the three chosen MUBs [79].

The experimental setup used for generating and testing the states of the MUBs is the same as in the hybrid qusix case (see Fig. 4.3), but with the polarization optics set so as to keep a fixed polarization everywhere. The kinoform generation was based on the method described in Sec.4.4. Figure 4.6 a) shows the intensity and phase profile of the 18 OAM modes which form the three MUBs. In Figure 4.6 b), the theoretical and experimental probability distributions for all combinations of state preparation and detection are reported. The similarity between the two distributions is $S = (99.06 \pm 0.04)\%$ while the mean fidelity over the 18 states is $F = (98.78 \pm 0.08)\%$. Comparing this result with the hybrid case, in which only OAM states in dimension 3 were generated, we find that the fidelity of the OAM generation does not decrease rapidly with the dimensions. Hence, the holograhic method used in this work promises to be suitable for the high-fidelity generation of OAM photonic qudits with very large dimension d.

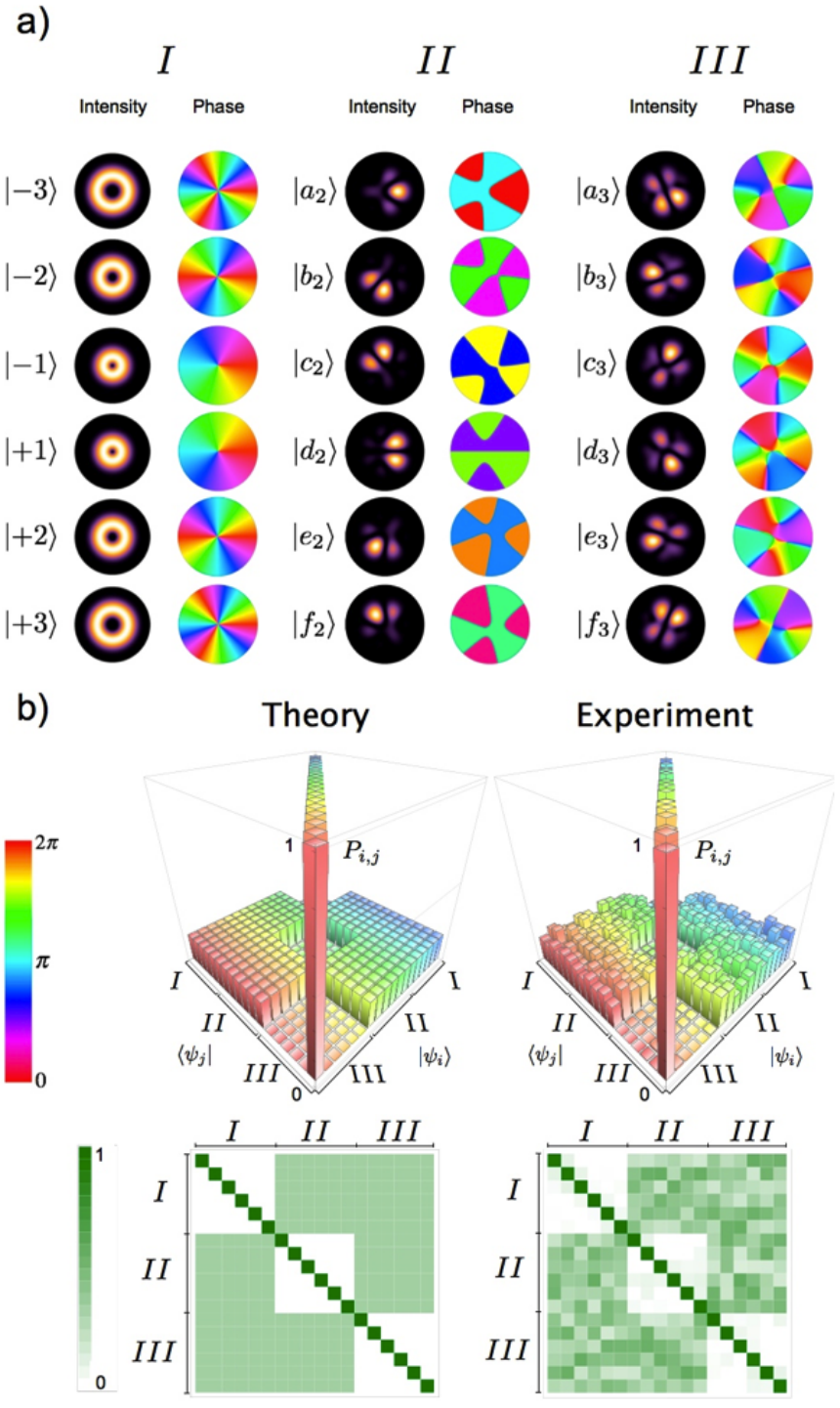

FIGURE 4.6: Experimental analysis of pure OAM qusix [79]. a) Graphical representation of all 18 states of the three selected MUBs, in the case of pure OAM 6D encoding. The precise definition of these states is given in in Appendix C. For each state, both the intensity and phase patterns are shown. b) Theoretical and experimental probability distributions for an experiment in which all the 18×18 combinations of generated/detected states belonging to the three MUBs are tested.

Chapter 5

Simulation of quantum walks and topological phases

5.1 Introduction

A random walk (RW) represents the dynamics of a single particle which moves in a discrete lattice; at each step of the evolution, the particle is shifted along a specific direction that is determined according to a random process, such as the toss of a coin. RWs and their generalization to multi-particle schemes are used to model a variety of physical systems, or stochastic processes bearing on other disciplines such as finance, and are a key element in computer sciences.

Quantum walks (QW) [107, 108] have emerged recently as the quantum analog of the classical RWs, and they are becoming an important resource in several quantum sciences. Relying on these processes, quantum algorithms [109–112] and schemes for universal quantum computation [113–115] have been introduced. Moreover, they can be exploited for the simulation of phenomena occurring in complex systems, such as energy transport in chemical processes [116] or Anderson localization in disordered media [117]. In 2010, Kitagawa *et al.* put forward for the first time the idea that QWs could be exploited for the simulation of topogical phases (TP) which characterize condensed matter systems [118], demonstrating that QWs protocols could realize all classes of TPs in 1D and 2D systems [119]. Recently, topologically-protected bound states have been observed at the interface between regions with different topologies [120].

The versatility of QWs as a tool for several quantum applications has fueled the search for platforms for their experimental realization; although many schemes have been demonstrated [121], the implementation of stable, scalable and efficient protocols is still a demanding task. In the last decade indeed, implementations of QWs in 1D have been

realized in a variety of physical systems, such as trapped ions [122, 123] or atoms [124], nuclear-magnetic resonance (NMR) systems [125], and photons, using both bulk optics [126–128] and integrated waveguides [129–131]. Remarkably, only a few photonic simulations of multi-particle QWs have been reported, using two-photon states [117, 129–131] or classical coherent sources [132]. Among these, photonic platforms can be distinguished according to the optical degrees of freedom that are considered for the encoding of the two sub-systems characterizing a QW, that is the walker and the coin. In 2010, Zhang *et al.* proposed a novel protocol based on the idea of encoding the walker and the coin in the OAM and in the SAM of single photons [133], respectively. The scheme relies on the presence of a q-plate at each step of the process, which realizes the shift of the walker's coordinate, conditioned by the coin state. The novel protocol was the first demonstration of a QW involving inner degrees of freedom and taking place in a single light beam, thus not requiring real space interferometers for its implementation. Other schemes involving SAM and OAM of light have already been demonstrated [126], but they rely on splitting and recombining the beam at each step, as for the other photonic implementations.

In this chapter, we report the results of two different experiments regarding the realization of quantum walks, and their application for the simulation of a quantum topological phase transition. In the first experiment, we implemented a generalization of the scheme proposed by Zhang *et al.*. In addition to the simulation of standard QWs, we considered a novel class of these processes, corresponding to the unitary evolution obtained with a partial tuning of the q-plates, which we named *hybrid* QWs. Interestingly, the optical retardation of the QP has a strong influence on the topological features of the system. In addition, we exploited one of the advantages of this implementation, that is the possibility of preparing the initial state of the walker in a delocalized state, as resulting from the superposition of many lattice sites [134, 135]; as a specific demonstration of the usefulness of such possibility, we prepared OAM Gaussian wave packets and observed their free evolution, which is governed by the QW band structure and the associated dispersion relation. Finally, we demonstrated that our platform is suitable for multi-particle walks, reporting a QW for two indistinguishable photons.

In the second experiment, we introduced a hybrid QW protocol, in which different values of the parameter δ (the q-plate optical retardation) determine the existence of two different topological phases. Varying δ in order to induce a phase change in the system, we investigated the transition by looking at the moments of the final probability distribution of the walker, after a finite number of steps. Indeed we have shown that in the large time limit (high number of steps) this moments are affected by a discontinuity at the phase transition, which is associated with the group velocity dispersion in the Brillouin zone. These features were observed directly in a 6-steps QW. At the same

time, we provided a theoretical demonstration of our results, determining the analytical expression for the first and the second order moments in the large time limit.

5.2 Theoretical description of a quantum walk[1]

The simplest version a QW consists of a single walker moving on a 1D lattice; this degree of freedom is described in terms of a infinite dimensional Hilbert space $\mathcal{H}_w$, spanned by kets $|x\rangle_w$, with $x \in \mathbb{Z}$. The walker has an internal degree of freedom, usually referred to as *coin*, described by a 2D Hilbert space $\mathcal{H}_c$; for the latter, we consider the basis formed by kets $\{|\uparrow\rangle_c, |\downarrow\rangle\}_c$ (in the following, subscripts c and w will be omitted for brevity whenever there is no risk of ambiguity). The Hilbert space $\mathcal{H}$ describing the global system (walker plus coin), is the direct product of $\mathcal{H}_c$ and $\mathcal{H}_w$. In this space, the QW dynamics is given by the evolution operator $\widehat{U}_0$ associated with a single step of the process; indeed, after n steps, a system prepared in the initial state $|\psi_0\rangle$ will evolve to the final state $|\psi_n\rangle$, given by

$$|\psi_n\rangle = (\widehat{U}_0)^n |\psi_0\rangle. \tag{5.1}$$

The positive integer n plays the role of a discrete temporal coordinate, and this type of quantum evolution is referred to as discrete time QW. We may consider the case where the time is a continuous variable, but the introduction of such continuous time QWs is out of the scope of this work. The operator U_0 is made of two terms; the first is a conditional displacement, described by the operator $\widehat{S}$. Being $\widehat{L}^{\pm}|x\rangle = |x \pm 1\rangle$ the two operators increasing or decreasing the walker's coordinate by one lattice unit, respectively, the operator $\widehat{S}$ is defined as follows:

$$\widehat{S} = |\uparrow\rangle\langle\uparrow| \otimes \widehat{L}^{+} + |\downarrow\rangle\langle\downarrow| \otimes \widehat{L}^{-} \tag{5.2}$$

The state of the coin subsystem determines the direction of the displacement the walker undergoes at each step of the process. Alternatively, the step operator can be expressed as

$$\widehat{S} = e^{i\widehat{S}_z \otimes \widehat{P}}, \tag{5.3}$$

where $\widehat{S}_z = |\uparrow\rangle\langle\uparrow| - |\downarrow\rangle\langle\downarrow|$ and $e^{i\widehat{P}\,a}$ is the operator associated with the translation in the walker space, being a the length of the displacement ($a = 1$ in our case) and $\widehat{P}$ the momentum operator. It is clear that $\widehat{S}$ is not separable in a coin and a walker part,

[1] Some paragraphs and sentences of this section are adapted or copied verbatim from the work [106] which I coauthored

whereas it entangles the two degrees of freedom [134, 136]. Between consecutive steps, the "randomness" is introduced by a unitary operator $\widehat{T}$, acting on the coin DOF only; this can be described as a matrix, that is

$$T = \begin{pmatrix} a & b^* \\ b & -a^* \end{pmatrix} \tag{5.4}$$

with a, b complex numbers such that $|a|^2 + |b|^2 = 1$. Unbiased walks are obtained when $|a| = |b|$; among these, it is common to consider the Hadamard walk, corresponding to the case $a = b = 1/\sqrt{2}$. The step operator is realized cascading the conditional displacement $\widehat{S}$ and the coin tossing $\widehat{T}$ operators, and it has the following expression:

$$\hat{U}_0 = \hat{S} \cdot (\hat{T} \otimes \hat{I}_w), \tag{5.5}$$

where $\hat{I}_w$ is the identity operator in $\mathcal{H}_w$. The translation symmetry which affects the process can be broken by letting the coin operator $\widehat{T}$ (5.4) depend on the x coordinate. This generalization is necessary when disorder is considered, as for the investigation of Anderson localization [117] and associated phenomena; nevertheless in this work we will concentrate on QWs where the coin tossing operator is uniform over the whole lattice. The basic features of QWs, and the main differences with respect to the classical RW, can be observed by studying the dynamics of a system whose initial state is

$$|\psi_0\rangle = (\alpha|\uparrow\rangle_c + \beta|\downarrow\rangle_c) \otimes |0\rangle_w, \tag{5.6}$$

where α and β are complex coefficients satisfying the normalization condition $|\alpha|^2 + |\beta|^2$. The state introduced in Eq. 5.6 is separable in terms of a coin and a walker term. It is worth to mention that we are considering the case of a walker which is initially localized, as it occupies only the site $x = 0$. Nevertheless, this not the general case, since quantum mechanics allows for extended initial conditions, corresponding to delocalized initial states obtained from the coherent superposition of many lattice sites; we will discuss this possibility later on. After a n-steps walk, we can compute the final state as defined in Eq. 5.1, and evaluate the probability $P(x)$ to find the system in any position x over the 1D lattice, regardless of the coin state. In the quantum formalism, $P(x)$ is equal to

$$P(x) = |\langle x, \uparrow |\psi_n\rangle|^2 + |\langle x, \downarrow |\psi_n\rangle|^2 . \tag{5.7}$$

In Fig. 5.1 we report the probability distributions calculated using Eq. 5.7 for three different coin initial states (the specific expression for these states is provided in the caption of the figure), in order to highlight the role of this feature and to mark some differences with respect to the classical RW. For this calculation, we referred to the

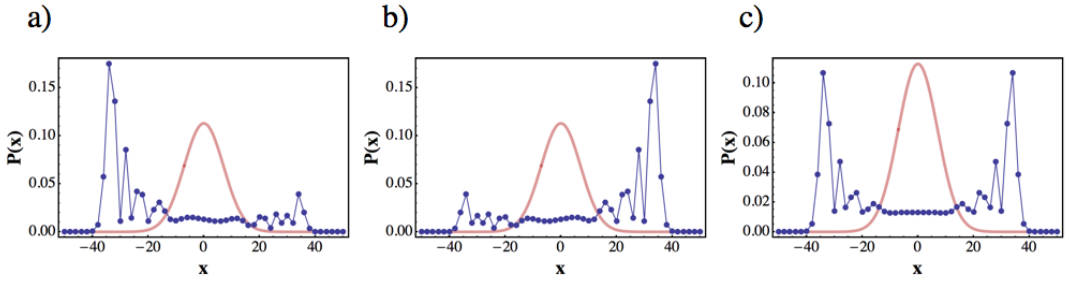

FIGURE 5.1: Comparison between classical and quantum probability distributions for the walker position after a 50-step walk. The red continuous line represents the typical Gaussian distribution for the walker position in a classical unbiased RW; it is centered around the initial position ($x = 0$), and it has a width that is proportional to $\sqrt{n}$, being n the number of steps of the walk; this feature is a signature of diffusive processes. The quantum case (blue points) has marked differences; the distribution is not symmetric in general, and such asymmetry depends on the initial state of the coin part of the system. This can be appreciated in panels a), b) and c), corresponding to initial conditions (see Eq. 5.6) $(\alpha, \beta) = (1, 0)$, $(\alpha, \beta) = (0, 1)$, and $(\alpha, \beta) = (1/\sqrt{2})\,(1, i)$, respectively. The reason for asymmetric distributions will be clear later on, when discussing the band structure of QWs and the propagation of Gaussian wave packets governed by the system dispersion relation. Independently of the coin initial state, remarkably the standard deviation of the quantum probability distribution is proportional to n, thus showing that a QW is a ballistic process.

case of the Hadamard walk; nevertheless, the results we obtain are generic properties of QWs. In contrast to the probability distribution of a RW, which has a Gaussian profile centered around the initial position $x = 0$, and with a variance $\sigma^2 \propto n$, in a QW the walker wave packet spreads much faster, as the variance of its probability distribution scales with the square of the number of steps, that is $\sigma^2 \propto n^2$. Moreover for QWs the quantity distribution $P(x)$ is asymmetric, and its shape depends on the initial conditions for the coin state. This shape is determined by the interferences of all the paths followed by the multiple components of the walker wave function [137], giving rise to the pronounced peaks appearing in Fig. 5.1. Quantum walks can be reduced to classical random walks measuring the state of the coin at each step [107], or by introducing a tunable decoherence during the evolution of the process [127].

5.3 Quantum walks using twisted photons[2]

In this section, I illustrate the main features of our photonic platform for the simulation of QWs. After describing the layout of the experimental apparatus, I report the experimental data of a QW for a single photon and for two indistinguishable photons.

In our implementation, the coin and the walker systems are encoded in the SAM and

[2]Some paragraphs and sentences of this section are adapted or copied verbatim from the work [106] which I coauthored

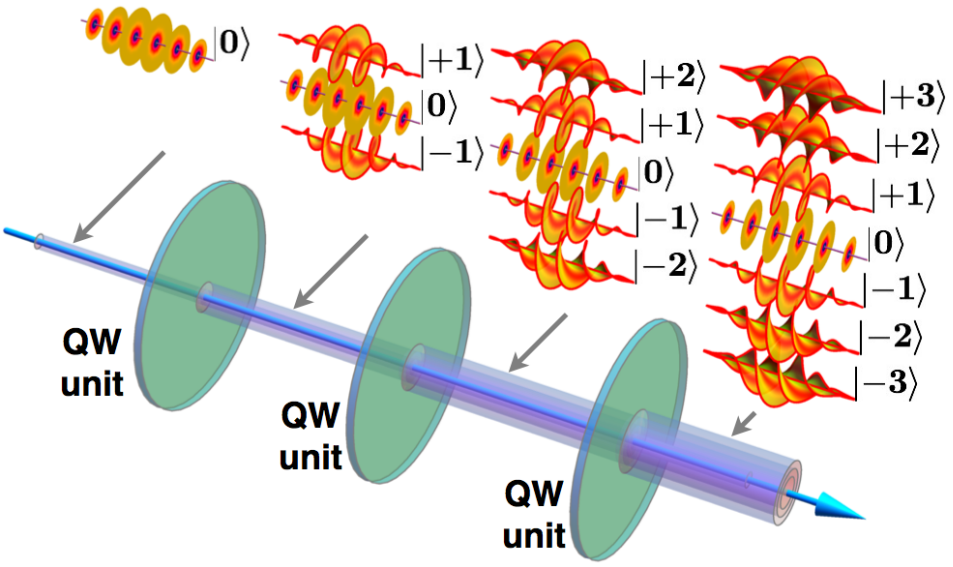

FIGURE 5.2: Conceptual scheme of the single-beam photonic quantum walk in the space of OAM [106]. In each traversed optical stage (QW unit), the photon can move to an OAM value m that is increased or decreased by one unit (or stay still, in the hybrid configuration). The OAM decomposition of the photonic wavefunction at each stage thus includes many different components, as shown in the call-outs in which modes having different OAM values are represented by the corresponding helical (or "twisted") wavefronts.

the OAM of a photon, respectively. In particular, the spatial walker coordinate x is replaced by the OAM coordinate m, while states $\{|\uparrow\rangle, |\downarrow\rangle\}$ are encoded in the polarization states $\{|L\rangle, |R\rangle\}$:

$$|x\rangle_w \longrightarrow |m\rangle_o \tag{5.8}$$

$$\{|\uparrow\rangle_c, |\downarrow\rangle_c\} \longrightarrow \{|L\rangle_\pi, |R\rangle_\pi\} \tag{5.9}$$

The concept of a QW in OAM within a single optical beam is pictorially illustrated in Fig. 5.2. The step operator $\hat{U}_0$ is realized by means of linear-optical elements. In the coin subspace, the unitary operator $\hat{T}$ can be implemented by birefringent plates, such as quarter-wave plates (QWP) and/or half-wave plates (HWP). The shift operator $\hat{S}$ is realized by a q-plate (QP), whose properties have been discussed in Sec. 1.7. In particular, we recall that the action of the QP results in raising or lowering the OAM of the incoming photon according to its SAM state, while leaving the photon in the same optical beam, that is with no deflections nor diffractions. In the actual device, the radial profile of the photonic wave function undergoes a small alteration, which however can be approximately neglected in our implementation (see Appendix D). As reported in Eq. 1.60, the action of the q-plate is made of two terms. The first, proportional to $\cos(\delta/2)$, leaves the photon in its input state. The second, proportional to $\sin(\delta/2)$, implements the conditional displacement of Eq. 5.2, but also adds a flip of the coin

state. The latter effect can be compensated by inserting an additional HWP. When $\delta = \pi$ ("standard" configuration) the first term vanishes and the standard shift operator $\hat{S}$ is obtained. When $\delta = 0$, the evolution is trivial (the walker stands still), while for intermediate values $0 < \delta < \pi$ we have a novel kind of evolution: besides moving forward or backward, the walker at each step is provided with a third option, that is to remain in the same position. We refer to this as a "hybrid" configuration, since it mimics a walk with three possible choices, although the coin is still two-dimensional. Similar to an effective mass, the δ parameter controls the degree of mobility of the walker, ranging from a vanishing mobility for $\delta = 0$ to a maximal mobility (not taking into account the effect of the coin) for $\delta = \pi$.

5.3.1 Quantum walk simulation for a single photon

To demonstrate the correct behavior of the proposed platform, in our first experiment we simulated a QW whose step operator $\hat{U}_0$ is implemented by a sequence of a QWP, a QP, and a HWP. The QPs have $q = 1/2$, so as to induce OAM shifts of ± 1. Due to reflection losses (mainly at the QP, which is not antireflection-coated), each step has a transmission efficiency of 86% (but adding an antireflection coating could easily improve this value to $> 95\%$). The n-step walk is then implemented by simply cascading a sequence of QWP-QP-HWP on the single optical axis of the system. In the implemented setup, the linear distance d between adjacent steps is small compared to the Rayleigh range z_R of the photons, i.e. $d/z_R \ll 1$ (near-field regime), so as to avoid optical effects that would alter the nature of the simulated process ((see Appendix D)). The layout of the apparatus is shown in Fig. 5.3. A single photon source, operating in the heralded regime, is realized as explained in Appendix B (this part of the setup is not shown in the figure).

The photon entering the QW setup is initially prepared in a separable state $|\psi_0\rangle = |\phi_0\rangle_c \otimes |\psi_0\rangle_w$. A computer-generated hologram shown on a spatial light modulator (SLM 1) can be used to prepare the walker initial state in a generic superposition of OAM states [78, 79] in H_o, as it will be discussed below. In this experiment, we displayed a simple grating on SLM1, so as to diffract photons without altering their spatial distribution, that is $m = 0$ at the exit of the device. Then the coin is prepared in the state $|\phi_0\rangle_c = \alpha|L\rangle + \beta|R\rangle$, where the two complex coefficients α and β (with $|\alpha|^2 + |\beta|^2 = 1$) can be selected at will by a QWP-HWP set (apart from an unimportant global phase). After the initial state preparation, the photon undergoes the QW evolution and, at the exit, is analyzed in both polarization and OAM so as to determine the output probabilities. In Figs. 5.4, 5.5 we report the experimental and predicted results relative to a 4-step QW, for a single photon entering the walk in the localized state $m = 0$, with varying the initial polarization. For each initial state of the coin, we performed the experiment both

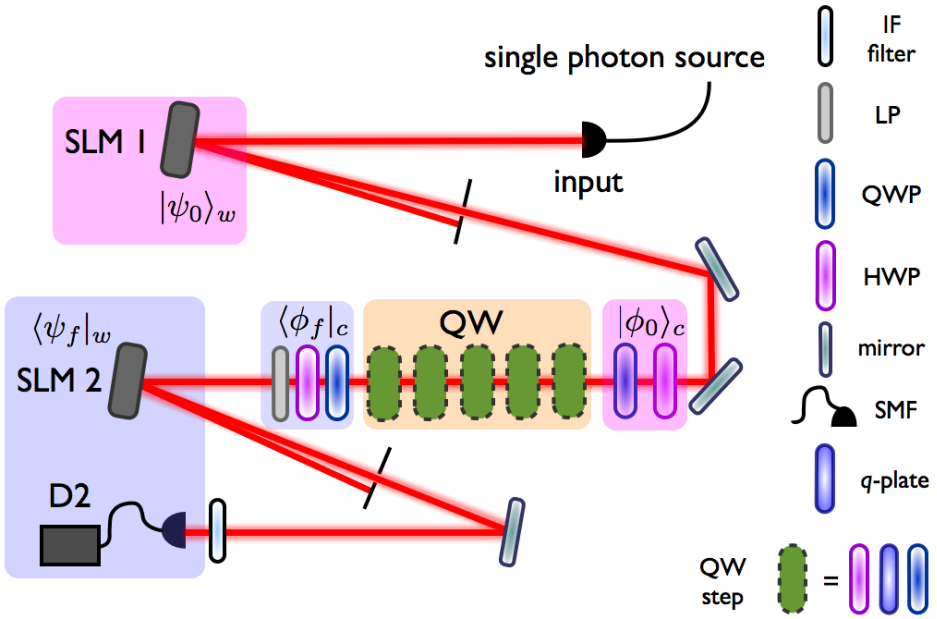

FIGURE 5.3: Experimental apparatus for single-photon QW experiments [106]. The single photon source, realized as explained in Appendix B, allows to have heralded single photons at the exit of the SMF represented in the figure. At the exit of the latter, the photon goes through N identical subsequent QW steps ($N = 5$ in the figure), is then analyzed in both polarization and OAM and is finally detected with an avalanche photodiode (APD) D2, in coincidence with D1 (not shown in the figure). Before entering the first QW step, a spatial light modulator (SLM 1) and a HWP-QWP set are used to prepare the photon initial state in the OAM and SAM spaces, respectively. At the exit of the last step, the polarization projection on the state $|\phi_f\rangle_c$ is performed with a second HWP-QWP set followed by a linear polarizer (LP). The OAM state is then analyzed by diffraction on SLM 2, followed by coupling into a SMF. The projection state $|\psi_f\rangle_w$ corresponding to each OAM eigenvalue m was thus fixed by the hologram pattern displayed on SLM 2. Before detection, interferential filters (IF) centered at 800 nm and with a bandwidth of 3.6 nm were used for spectral cleaning. As shown in the legend, a single QW step consists of a QWP (optical axis at 45° from the horizontal), a q-plate with $q = 1/2$ (axis at 0°), and a HWP (axis at 0°).

in the standard and hybrid configurations. To evaluate quantitatively the agreement between measured and predicted probability distributions, $P(m)$ and $P'(m)$, we also computed their "similarity", which was introduced in Sec. 4.5;

$$S = \frac{\left(\sum_m \sqrt{P(m)P'(m)}\right)^2}{\left(\sum_m P(m) \sum_m P'(m)\right)}. \tag{5.10}$$

The values we obtained in the various cases are given in the figure captions.

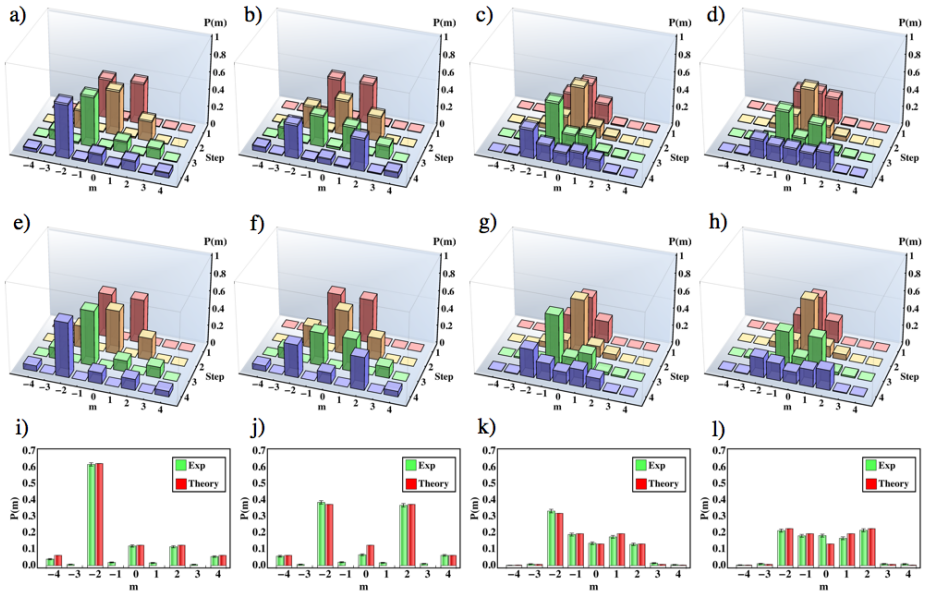

FIGURE 5.4: Four-step quantum walk for a single photon with localized input [106]. a-d) Experimental results, including both intermediate and final probabilities for different OAM states in the evolution (summed over different polarizations). The intermediate probabilities at step n are obtained by switching off all QPs that follow that step, that is setting $\delta = 0$. Panels a) and b) refer to the standard case with two different input states for the coin subsystem, $(\alpha, \beta) = (0, 1)$ and $1/\sqrt{2}(1, i)$, respectively. c) and d) refer to the hybrid case with $\delta = 1.57$, with the same initial coin-states. e-h) Corresponding theoretical predictions. Poissonian statistical uncertainties at plus-or-minus one standard deviation are shown as transparent-volumes in panels a-e. The similarities between experimental and predicted final OAM distributions are $(94.7 \pm 0.4)\%$, $(93.4 \pm 0.5)\%$, $(99.7 \pm 0.1)\%$ and $(99.2 \pm 0.2)\%$, respectively. Panels on the same column refer to the same configuration and initial state. The color scale reflects the number of steps.

5.3.2 Quantum walk for two indistinguishable photons

Specific applications of quantum walks require multi-particle schemes, as for instance the universal quantum computation protocol proposed in Ref. [115]. Moreover, although a QW of a single photon is a quantum regime, it behaves equivalently to a classical one, as the resulting probability distributions are identical to the intensity distributions that would be obtained using classical (coherent) light. For this reasons, we have shown that our scheme can efficiently simulate a multi-particle quantum walk, performing an experiment for two indistinguishable photons, and observing quantum interferences that cannot be reproduced classically. The layout of the setup for the simulation of a 2-photon QW is shown in Fig. 5.6. As explained in Appendix B, both photons generated in the SPDC process are collected in the same optical fiber, after compensating their temporal and longitudinal walk-off (this part of the setup is not shown in the figure.). At the

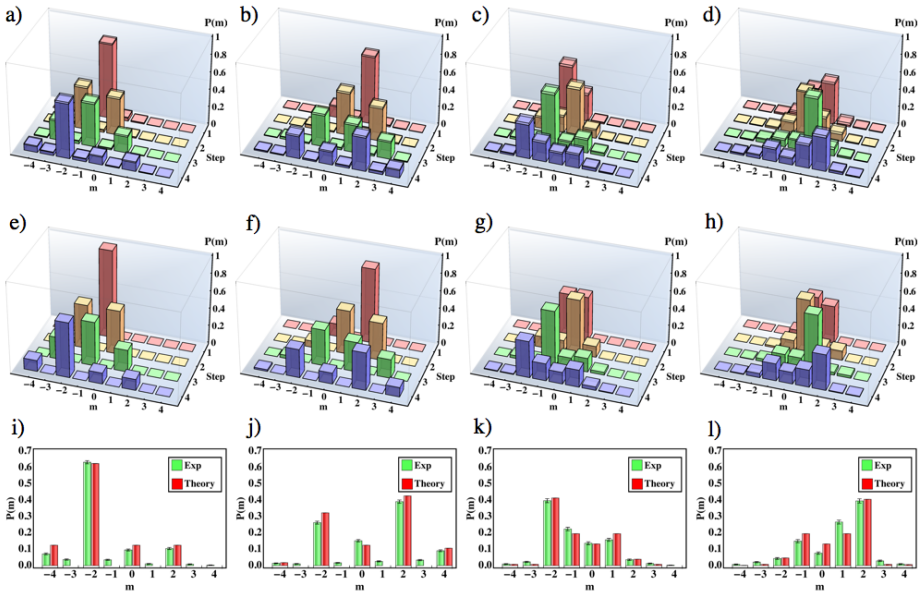

FIGURE 5.5: Further data for a four-step quantum walk [106], presented following the same scheme adopted in Fig. 5.4. a-b) Standard case with two different input states for the coin subsystem, $(\alpha, \beta) = (1, -1)$ and $1/\sqrt{2}(1/\sqrt{2}, 1 - i/\sqrt{2})$, respectively. c-d) Hybrid case for $\delta = \pi/2$, with the coin subsystem, $(\alpha, \beta) = (1, -1)$ and $1/\sqrt{2}(1 - i/\sqrt{2}, 1/\sqrt{2})$, respectively. e-h) Corresponding theoretical predictions. i-l) Comparison of measured and predicted final probabilities. Poissonian statistical uncertainties at plus-or-minus one standard deviation are shown as error bars in panels (i)-(n) and as transparent-volumes in panels (a)-(e). The similarities between experimental and predicted OAM distributions are $(89.7 \pm 0.2)\%$, $(90.9 \pm 0.6)\%$, $(98.9 \pm 0.1)\%$ and $(97.0 \pm 0.4)\%$, respectively. Panels in the same column refer to the same configuration and initial state.

exit of the SMF, both photons were sent through the QW step sequence. The biphoton polarization state is prepared as described by the ket $|L, R\rangle$, by means of QWP-HWP set. In this case we explored only the case where the walk starts in $m_1 = m_2 = 0$, thus we removed the first SLM to improve the setup efficiency. The two photons, propagating along the same optical axes, go through a 3 steps QW. Since the two photons cannot be distinguished (except for the input polarization, which is however modified in the QW process) and propagate along the same axis, at the exit of the last step we introduced a 50:50 beam splitter (BS) to split them and perform independent SAM-OAM projective measurements on the two arms. This splitting stage and the duplication of the projection devices represent the main difference of this setup with respect to the apparatus discussed in Fig. 5.3. This process has an efficiency of 50%, as a result of the 1/2 probability that the two photons will exit from distinct BS ports. At the exit of the BS, each arm is provided with a linear polarizer for the projective measurement in the SAM space. As in the previous case, the OAM projection is performed using an

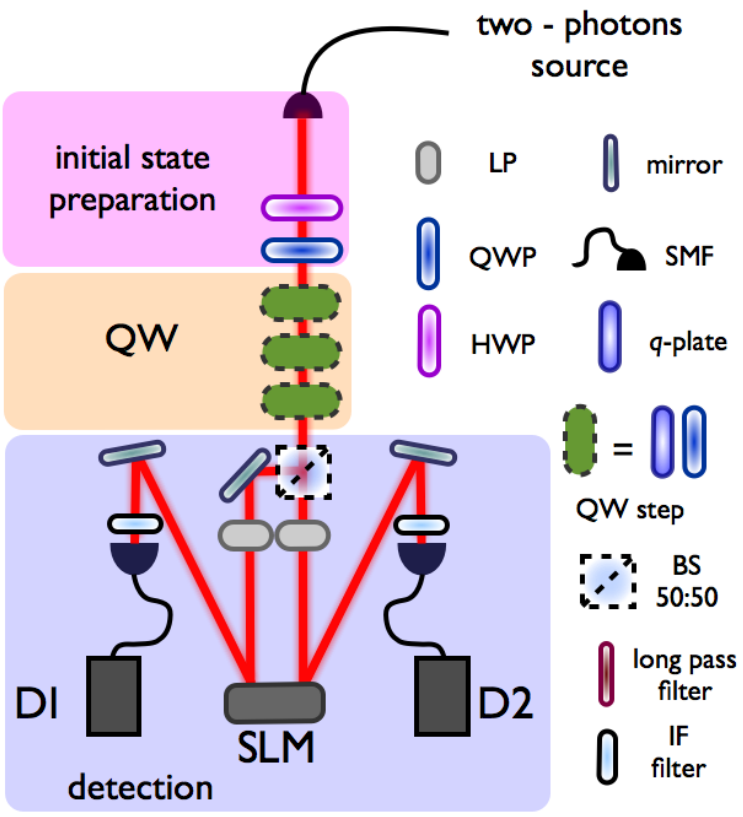

FIGURE 5.6: Two-photon quantum walk apparatus [106]. At the exit of the input SMF, a biphoton state is prepared by means of a QWP-HWP set in the state $|L, R\rangle$. Since here we explored only the case where the walk starts in $m_1 = m_2 = 0$, the first SLM was not needed and was removed. The two photons, propagating along the same optical axis, go through a 3 steps QW. At the exit of the last step, a 50:50 BS randomly separates the two photons. At the exit of the BS, each arm is provided with a HWP and a linear polarizer for the projective measurement in the SAM space. The OAM projection is then performed using an SLM and a SMF. For the projection on both arms, a single SLM was used, dividing its screen into two sections and showing independent holograms. Two interferential filters were used to filter the photon band so as to enhance the wavelength indistinguishability of the two photons. Finally, signals from photodiodes D1 and D2 provided the coincidence counts.

SLM and a SMF. For the projection on both arms, a single SLM was used, dividing its screen into two sections and showing independent holograms. Before the last SMFs two interferential filters (IF) centered at 800 nm and with a bandwidth of 3.6 nm were used to filter the photon band so as to enhance the wavelength indistinguishability of the two photons. Finally, signals from photodiodes D1 and D2 were analyzed using a digital logic unit (time window 8 ns) combined with digital counters in order to get the final coincidence counts. Before starting the main experiment, the indistinguishability of the two photons generated in the SPDC process was optimized and verified as discussed in Appendix B.

In Fig. 5.7, the results relative to a 3-step QW with localized OAM input $m = 0$ are reported and compared with the theoretical predictions obtained for indistinguishable

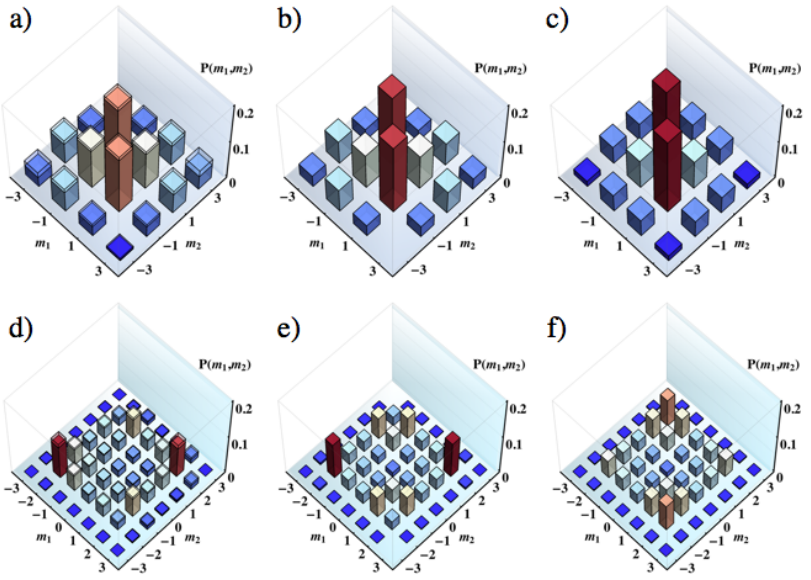

FIGURE 5.7: Three-step quantum walk for two identical photons [106]. In this case, only final OAM probabilities are shown (summed over different polarizations). a-c) Case of standard walk. a) Experimental results. Vertical bars represent estimated joint probabilities for the OAM of the two photons. Since the two measured photons detected after the BS splitting are physically equivalent, their counts are averaged together, so that (m_1, m_2) and (m_2, m_1) pairs actually refer to the same piece of data. Even values of m_1 and m_2 are not included, since they correspond to sites that cannot be occupied after an odd number of steps. b) Theoretical predictions for the case of indistinguishable photons. c) Theoretical predictions for the case of distinguishable photons, shown to highlight the effect of two-photon interference (Hong-Ou-Mandel effect) in the final probabilities. It can be seen that the experimental results agree better with the theory for indistinguishable photons. d-f) Case of hybrid walk (with $\delta = 1.46$). d), e) and f) refer respectively to experimental data, indistinguishable photon theory and distinguishable photon theory, as in the previous case. The QW step in these two-photon experiments is implemented with a QP and a QWP. Again, our experiment is in good agreement with the theory based on indistinguishable photons, proving that two-photon interferences are successfully implemented in our experiment. The similarities between experimental and predicted quantum distributions (IPT model) are $(98.2 \pm 0.4)\%$ and $(95.8 \pm 0.3)\%$ for the standard and the hybrid walk, respectively. The similarities with the DPT model are instead 96.4% and 91.8%, respectively. The color scale (common to all panels referring to the same case) reflects the vertical scale, to help comparing the patterns.

photons (while taking into account the effect of the final beam splitter), hereafter labeled as "indistinguishable-photon theory" (IPT). The two distributions show a good quantitative agreement, as is confirmed by their similarities being higher than 95% (see figure captions for details). These similarities are defined as in the single photon case, with the index m replaced by the pair of OAM values (m_1, m_2). The predicted distributions for the case of distinguishable photons (DPT) are also shown for comparison, to highlight the role of two-particle interference in the final distributions. The similarities of the data with the DPT distributions are significantly lower. However, the similarity is not a very

sensitive test, as it tends to remain high even for fairly different distributions. Hence, we also computed the "total variation distance" (TVD, defined as the sum of the absolute values of all probability differences divided by two) for the two cases. In the standard case, the TVD of the experimental distribution with the IPT one is $(6.5 \pm 0.9)\%$, to be compared with the TVD of $(16.5 \pm 0.9)\%$ for the DPT model. In the hybrid case, the TVD with the IPT is $(13.5 \pm 0.7)\%$, to be compared with $(21.1 \pm 0.7)\%$ for the DPT. These values confirm that two-photon interferences are present in our experiment. We ascribe the residual discrepancies between the observed distributions and the IPT quantum predictions to systematic errors arising from imperfect alignment of the setup. On the other hand, it is also possible to demonstrate a quantum behavior in the observed distributions independently of any specific model for the photon propagation in the QW system, so as to be insensitive to alignment imperfections or other kinds of systematic errors. This is accomplished by testing the violation of certain characteristic inequalities that constrain any possible correlation distribution obtained with two classical light sources instead of two photons [129], or with two distinguishable photons. Indeed for the former case, it can be proved that

$$T_{p,q} = \frac{1}{3}\sqrt{P_{p,p}P_{q,q}} - P_{p,q} < 0, \tag{5.11}$$

$$\tag{5.12}$$

where $P_{p,q}$ is the joint probability distribution for the OAM values of the two photons. For the case of distinguishable photons, we have that

$$T_{p,q} = \sqrt{P_{p,p}P_{q,q}} - P_{p,q} < 0. \tag{5.13}$$

Details about the derivation of Eqs. 5.11 and 5.13 are provided in Appendix E. The measured distributions violate these inequalities by several standard deviations, as illustrated in Fig. 5.8 for the standard QW. Further data relative to the hybrid walk are reported in Fig. E.1. These results proves once more that the measured correlations must be quantum and that they include the effect of multi-particle interference.

5.4 Band structure and dynamics of wave packets in a QW

In Sec. 5.2 we have introduced the theoretical formalism for the description of a quantum walk process, providing the expression of the step operator $\widehat{U}_0$ in the position representation of the walker degree of freedom. Nevertheless, the latter can be described in terms of the quasi-momentum k, which represents the conjugate variable with respect to the lattice position x labeling the lattice sites, and is defined in the first Brillouin zone

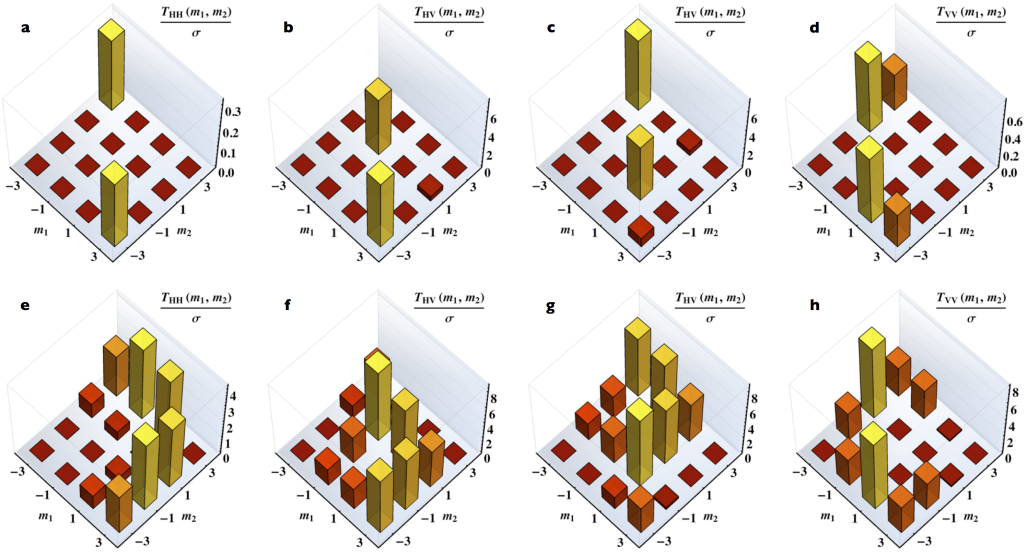

FIGURE 5.8: Experimental violation of correlation inequalities for two photons which have completed the standard QW ($\delta = \pi$). The data are based on the coincidences after the final beam-splitter. (a)-(d) Violations of the inequalities given in Eq. (5.11), constraining the correlations that would be obtained for two classical sources, incoherent to each other. Each panel refers to a different pair of measured polarizations for the two photons. These violations prove that our results can only be explained with quantum effects. (e)-(h) Violations of the inequalities given in Eq. (5.13), constraining the correlations obtained for two distinguishable photons. Again, each panel refers to a different pair of polarizations. These violations prove that our photons exhibit two-particle interferences. Only positive values of the $T_{p,q}$ are reported, while negative values which fulfil the inequality are omitted. All violations are given in units of Poissonian standard deviations σ, as determined from the coincidence counts. The color scale reflects the vertical scale.

$k \in (-\pi, \pi)$. The relation between the two representations is given by the discrete Fourier transform, i.e. $|k\rangle = (1/\sqrt{2\pi}) \sum_x e^{-ikx} |x\rangle$. The momentum representation provides the framework to analyze the effective band structure of the QW system. Indeed, due to the translational symmetry of the latter, eigenstates of the single step evolution operator $\hat{U}_0$ are obtained as the direct product of quasi-momentum eigenstates $|k\rangle_w$ in the walker space $\mathcal{H}_w$, and suitable eigenvectors $|\phi_s(k)\rangle_c$ living in the coin (polarization) space $\mathcal{H}_c$. We label these eigenstates as $|k, s\rangle = |\phi_s(k)\rangle_c \otimes |k\rangle_w$, with $s \in \{1, 2\}$[119, 120]. The corresponding eigenvalues are $\lambda_s(k) = e^{-i\omega_s(k)}$, where the relation between the energy ω and the quasi-momentum k can be derived once the coin operator $\hat{T}$ is assigned. The global phase of the latter, which has no influence on the dynamics of the system, can be adjusted so as to have $\det T = 1$ and $\omega_1 = -\omega_2$; in the following, we will refer explicitly to this case, omitting the index that labels the two energies. It is worth to mention that, being the QW characterized by a discrete temporal coordinate, ω is actually a quasi-energy, as it happens for the momentum k, defined in a Brillouin zone $(-\pi, \pi)$. The

problem of determining the coin part of the eigenstates of the system and the associated dispersion relation can be conveniently solved introducing the following representation for the evolution operator $\widehat{U}_0$

$$\widehat{U}_0 = \mathrm{Exp}\left\{-i\,\widehat{H}_e\right\} \tag{5.14}$$

where we have introduced the effective Hamiltonian $\widehat{H}_e$

$$\widehat{H}_e = \int_{-\pi}^{\pi} dk\,\omega(k)\,[\hat{\mathbf{u}}(k)\cdot\hat{\boldsymbol{\sigma}}]\otimes|k\rangle\langle k|. \tag{5.15}$$

Here, $\hat{\boldsymbol{\sigma}} = \{\widehat{\sigma}_1, \widehat{\sigma}_2, \widehat{\sigma}_3\}$ is a 3D vector whose components correspond to the three Pauli operators, while $\hat{\mathbf{u}}(k)$ is a 3D unit vector; for every value of $k \in (-\pi, \pi)$, $\hat{\mathbf{u}}(k)$ $[-\hat{\mathbf{u}}(k)]$ individuates the point on the Poincaré sphere corresponding to the coin eigenstate $|\phi_1(k)\rangle$ $[|\phi_2(k)\rangle]$. According to this picture, we are describing the QW as the stroboscopic simulation of a system characterized by the Hamiltonian $\widehat{H}_e$. In momentum space, the walker part of $\widehat{U}_0$ is diagonal, so for each value of k we can express this operator as a 2×2 matrix $U_0(k)$. The energy $\omega(k)$ can be simply determined as

$$\cos\omega(k) = \frac{1}{2}\mathrm{Tr}\,U_0(k) \tag{5.16}$$

Now let us consider the explicit case of the Hadamard walk, which we have introduced before. It is straightforward to see that the associated operator $U_0(k)$ can be written as

$$U_0(k) = \frac{i}{\sqrt{2}}\begin{pmatrix} e^{ik} & e^{ik} \\ e^{-ik} & -e^{-ik} \end{pmatrix} \tag{5.17}$$

The factor i was introduced in order to have $\mathrm{Det}\,U_0 = 1$. Using Eq. 5.16, we can determine the quasi-energy

$$\cos\omega(k) = \frac{\sin k}{\sqrt{2}}, \tag{5.18}$$

and the expressions for the components of the unit vector $\hat{\mathbf{u}}(k)$

$$u_1(k) = \cos k/N(k), \tag{5.19}$$

$$u_2(k) = -\sin k/N(k), \tag{5.20}$$

$$u_3(k) = \cos k/N(k), \tag{5.21}$$

where we have introduced a normalization factor $N(k) = \sqrt{2 - \sin^2 k}$. Now, starting from the dispersion relation $\omega(k)$, we can derive the group velocity $V(k) = d\omega/dk$;

$$V(k) = -\frac{\cos k}{\sqrt{2 - \sin^2 k}}. \tag{5.22}$$

From the previous equation, we can note that $u_1(k) = u_3(k) = -V(k)$, whereas $u_2(k) = \tan(k)\, V(k)$. We will exploit these properties later on. In Fig. 5.9 we report a graph for the dispersion relation and the group velocity dispersion. The two bands $s = 1$ and $s = 2$ are characterized by a finite energy gap, and their group velocities, defined as $V_s = d\omega_s/dk$, have the same magnitude but opposite sign, i.e. $V_1(k) = -V_2(k)$. Moreover, V_s is bound in the range $(-1/\sqrt{2}, 1/\sqrt{2})$, and it vanishes for $k = \pm\pi/2$. The coin eigenstates $|\phi_s(k)\rangle_c$ span a great circle on the Poincaré sphere, as a result of the so-called chiral or sublattice symmetry [119] [see Fig. 5.13a)]. The number of windings W of the vector $\hat{\mathbf{u}}(k)$, as k spans the entire Brillouin zone, is a topological invariant, which can be exploited to classify the topological phases of the system. These are typically referred to as symmetry-protected topological phases; indeed W is an invariant only when the continuous deformations applied to the system preserve the chiral symmetry. The role of this topological classification will be analyzed deeply in Sec. 5.6.

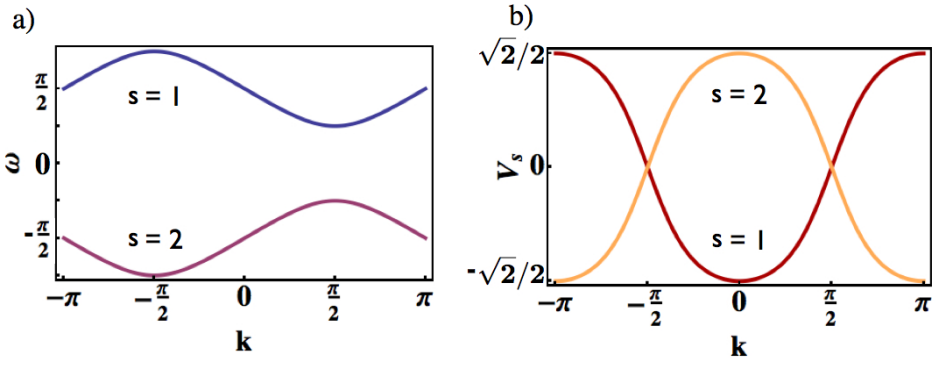

FIGURE 5.9: Band structure of the QW system [106]. a) The plot shows the dispersion relation $\omega_s(k)$ for both bands $s = 1$ and $s = 2$. A finite energy gap can be observed. b) Dispersion of the group velocity $V_s(k)$. It is worth noticing that when $k = \pm\pi/2$, the group velocity vanishes for both bands and, at the same time, it has the maximum slope. We will see later on that, in the context of wave packets dynamics, for these values of the quasi-momentum the dispersion of the group velocity will give a larger contribution to the broadening of the initial envelope, as compared with the case of packets propagating at finite speed.

The band structure characterizing a QW can be probed through the analysis of the free propagation of Gaussian wave packets, which is governed by the dispersion relations for the energy and the group velocity. Indeed, let us consider a state initially prepared as follows

$$|\psi_0\rangle = |\phi_1(k_0)\rangle \otimes \sum_x e^{-ik_0 x} A(x)|x\rangle, \tag{5.23}$$

where we assume that $A(x)$ is a Gaussian envelope centered around the position $x = 0$, whereas k_0 is a specific value of the quasi momentum in the Brillouin zone;

$$A(x) = N \,\mathrm{Exp}\left\{-\frac{x^2}{2\,\sigma^2}\right\} \tag{5.24}$$

Here σ^2 is the variance of the Gaussian distribution, and the constant N is introduced for normalization. Assuming a large value of σ, that is, a slowly varying envelope, Gaussian wave packets (5.23) propagate along the lattice with a finite speed, given by the group velocity $V_s(k_0)$, while the profile of the distribution undergoes only a tiny alteration [135]. In general, for any k_0, we can prepare the coin part as a superposition of the two bands $[\alpha|\phi_1(k_0)\rangle + \beta|\phi_2(k_0)\rangle]$, with $\{\alpha, \beta\}$ being normalized complex coefficients. Interestingly states belonging to different bands, which correspond to orthogonal coin eigenstates, propagate in opposite directions, i.e. $V_1(k_0) = -V_2(k_0)$, highlighting the strong coupling between the walker and the coin of this system. In Fig. 5.10 we plot the probability distributions $P(x)$ obtained from the simulation of a QW for Gaussian wave packets. It is clear that, when the value of σ is large enough to have a slowly varying envelope, wave packets propagate with negligible alterations. Being the whole process ruled by the dispersion relation of the system, we can exploit these phenomena to investigate the band structure of a QW; for instance, we can prepare these peculiar states at the beginning of the process and reconstruct their final distribution, eventually observing their propagation in the OAM lattice.

5.5 Verification of the band structure of a QW through the free propagation of OAM Gaussian wave packets[3]

One of the advantages of the photonic simulator of QWs described in Sec. 5.3 is the possibility to control the walker initial state, which can be prepared in any superposition of the different lattice sites. In particular, we can realize OAM Gaussian wave packets with a given quasi-momentum k_0, and study experimentally their free evolution in the QW system, thus probing the effective band structure and its associated topological structure. In this context, it is worth to mention that controlling the quasi-momentum of delocalized quantum states is crucial for carrying out quantum simulations of Bloch-particle dynamics, as shown for instance in Ref. [138]. Using the holographic method described in Sec. 4.4, we prepared single-photon wave packets given by $|\psi_0^s\rangle = |\phi_s(k_0)\rangle_c \otimes \left(\sum_m A(m)\, e^{-ik_0 m}|m\rangle_w\right)$, where $A(m) = A_0 e^{-m^2/2\sigma^2}$ is a Gaussian envelope in OAM space, as defined in Eqs. 5.23 and 5.24 . The associated quasi-momentum has a Gaussian

[3]Some paragraphs and sentences of this section are adapted or copied verbatim from the work [106] which I coauthored

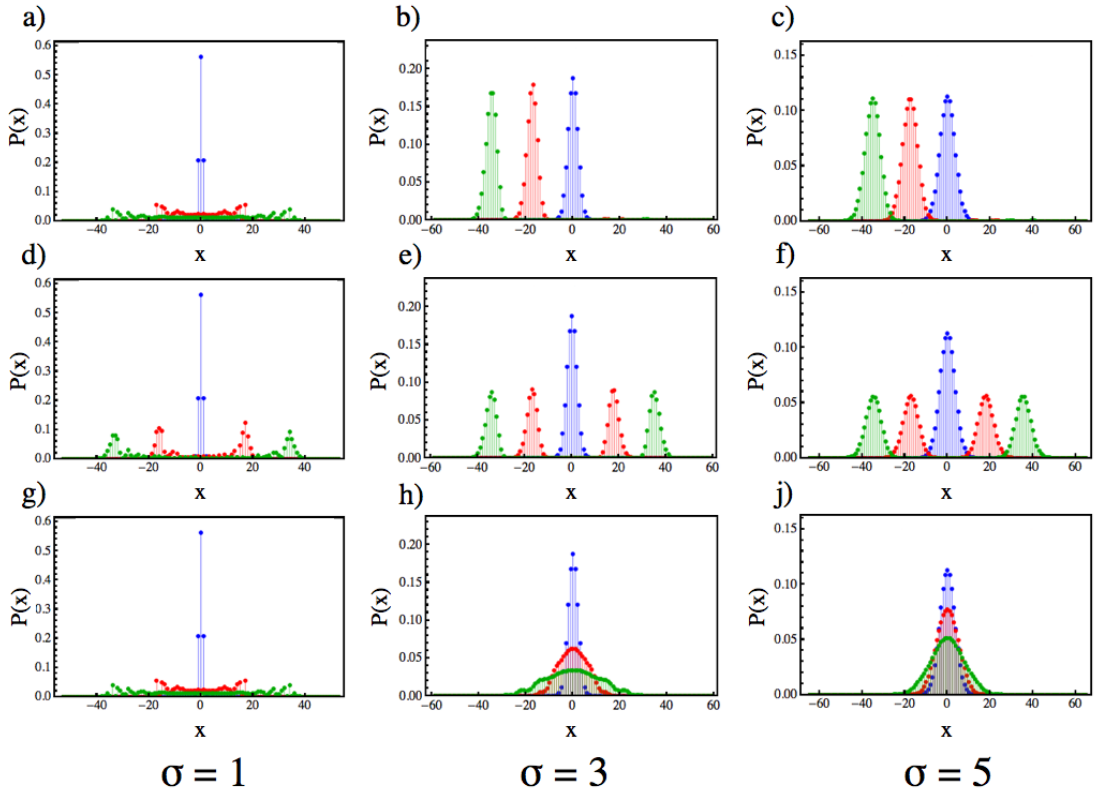

FIGURE 5.10: Propagation of Gaussian wave packets in a QW system. We simulate the QW evolution for the initial state given in Eq. 5.23. We report the probability distribution for the walker over the lattice sites as calculated after 25 steps (red points) and 50 steps (green points). Blue points correspond to the initial distribution. Various panels correspond to different initial states, obtained with varying the variance of the initial distribution and the values of the coefficients $\{\alpha, \beta\}$. a-c) $\{\alpha, \beta\} = \{1, 0\}$, $k_0 = 0$; the corresponding group velocity is $-1/\sqrt{2}$. Panels a), b) and c) refer to the case in which $\sigma = 1$, 3, 5, respectively, as reported in the lower part of the figure. Other panels are organized similarly. d-f) $\{\alpha, \beta\} = 1/\sqrt{2}\,\{1, 1\}$, $k_0 = 0$. Accordingly, the wave packet splits into two components, propagating in opposite directions. g-j) $\{\alpha, \beta\} = \{1, 0\}$, $k_0 = \pi/2$; the corresponding group velocity vanishes, and the wave packets remain centered around the initial position. Nevertheless, in this case σ increases with the number of steps, since the evolution is governed by the dispersion of the group velocity [135]. Comparison between the simulation for different values of σ highlights the role of the slowly varying envelope approximation, which was assumed to demonstrate that wave packets propagate with no significant alterations. From these figure, we can estimate a minimum value for σ which guarantees the validity of this approximation.

distribution centered on k_0. In our case, the average quasi-momentum k_0 corresponds to the average azimuthal angle in real space for the optical field distribution within the beam, thus represents a physical degree of freedom that can be observed directly. Few examples of the holograms we used for this experiment are reported in Fig. 5.11. As discussed in the previous section, when $A(m)$ is a slowly varying envelope, these wave packets are expected to propagate with only minimal shape variations and with a speed given by the group velocity $V_s(k_0) = (d\omega_s/dk)_{k=k_0}$.

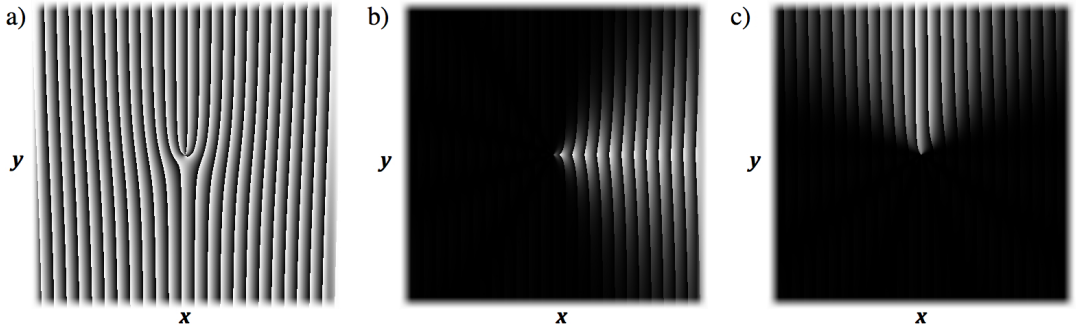

FIGURE 5.11: Holograms for the preparation of the OAM initial state before the QW process [106]. In the pictures the phase $M(x, y)$ (see Sec. 4.4), ranging in the interval $(0, 2\pi)$, is encoded in the grayscale level of each pixel. Panels a-c) refer to different initial states in the OAM space. a) Localized initial state $|\psi_0\rangle_w = |+3\rangle_w$. b-c) Delocalized Gaussian wave packets $|\psi_0\rangle_w = A_0 \sum_m e^{-ik_0 m} e^{-m^2/2\sigma^2} |m\rangle_w$, with $\sigma = 2$ and $k_0 = 0,\ \pi/2$, respectively. A_0 is a normalization constant.

In Fig. 5.12, we report the experimental "real-time" (i.e., step-by-step) observation of these propagating packets for a 5-step QW. These data refer in particular to the band $s = 1$, with $k_0 = \pi$ and $k_0 = \pi/2$, corresponding to maximum and vanishing group velocities, respectively, with a step operator implemented by a QP plus a QWP. Next, we proceeded to explore the whole irreducible Brillouin zone by varying the average quasi-momentum k_0 in steps of $\pi/8$ across the $(0, \pi)$ range. At each value of k_0, in order to obtain a single wave packet propagation, the SAM input state must be prepared in the eigenstate $|\phi_1(k_0)\rangle$, corresponding to a specific elliptical polarization. As discussed previously, SAM (or coin) eigenstates of these wave packets describe a maximum circle in the Poincaré polarization sphere, as illustrated in Fig. 5.13a. The number of full rotations of the vector $|\phi_1(k)\rangle$ on the sphere, as k varies from $-\pi$ to π, is a topological property of the QW system. In our case, we observe a single full rotation (we actually see half a rotation, as we tested only half Brillouin zone), thus verifying the topological class of our system. Other topological QW phases could be realized by modifying the QW step operator $\hat{U}$, as discussed in Ref. [119]. We then determined the group velocity of these wave packets by measuring the mean OAM exit value after 5 steps, as shown in Fig. 5.13b. The whole OAM distribution for some of these points is also shown in Figs. 5.13c-g.

Finally, the behavior of a wave packet whose coin is prepared in the superposition state $[|\phi_1(k_0)\rangle + |\phi_2(k_0)\rangle]/\sqrt{2}$ was also investigated. As a result of the spin-orbit coupling, the wave packet splits into two components propagating in opposite directions, as shown in Fig. 5.13h. In this example, the QW clearly leads to the generation of maximal entanglement between the SAM and OAM degrees of freedom.

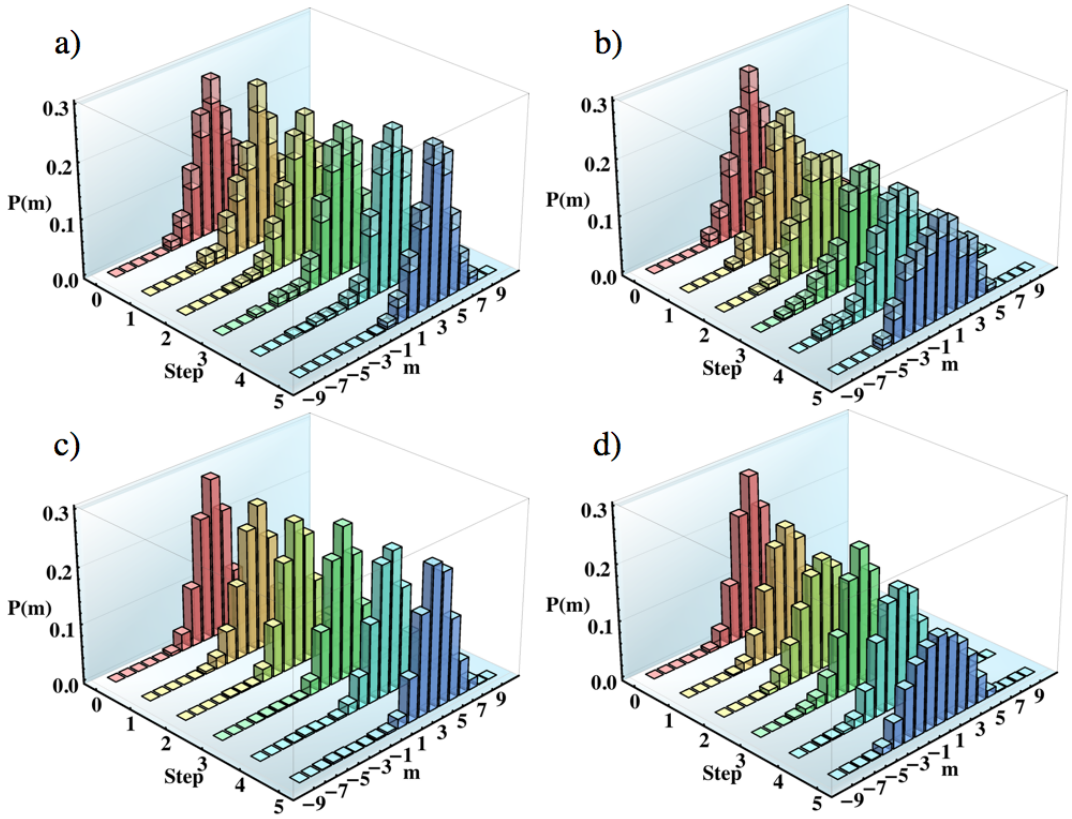

FIGURE 5.12: Wave packet propagation in a five-steps quantum walk [106]. a-b) Experimental results, showing the step-by-step evolution of the OAM distribution of a single photon prepared in a Gaussian wave packet with $\sigma = 2$, in the SAM band $s = 1$ (summed over different polarizations). Panels a) and b) correspond to the two cases $k_0 = \pi$ (maximal group velocity) and $k_0 = \pi/2$ (vanishing group velocity), respectively. The latter configuration shows some spreading of the Gaussian envelope, governed by the group-velocity dispersion. Poissonian statistical uncertainties at plus-or-minus one standard deviation are shown as transparent-volumes. c-d) Theoretical predictions corresponding to the same cases. At the fifth step, the similarity between experimental and theoretical OAM distributions are $(98.2 \pm 0.4)\%$ and $(99.0 \pm 0.2)\%$, respectively. The color scale reflects the number of steps.

5.6 Signature of a topological phase transition in a QW: theory and experiment

Topological features are responsible for fundamental phenomena in condensed matter systems [118, 139], such as for instance the fractional and integer quantum Hall effects or the existence of protected surface states in topological insulators. These systems are characterized by specific values of some topological invariants, defined in terms of the states forming the energy bands. Properties associated with these topological phases in complex systems can be conveniently studied through the use of quantum simulators [120, 138, 140, 141]; these allow for precise control of the system's symmetries and topological invariants, and for accurate measurements on the quantum state as

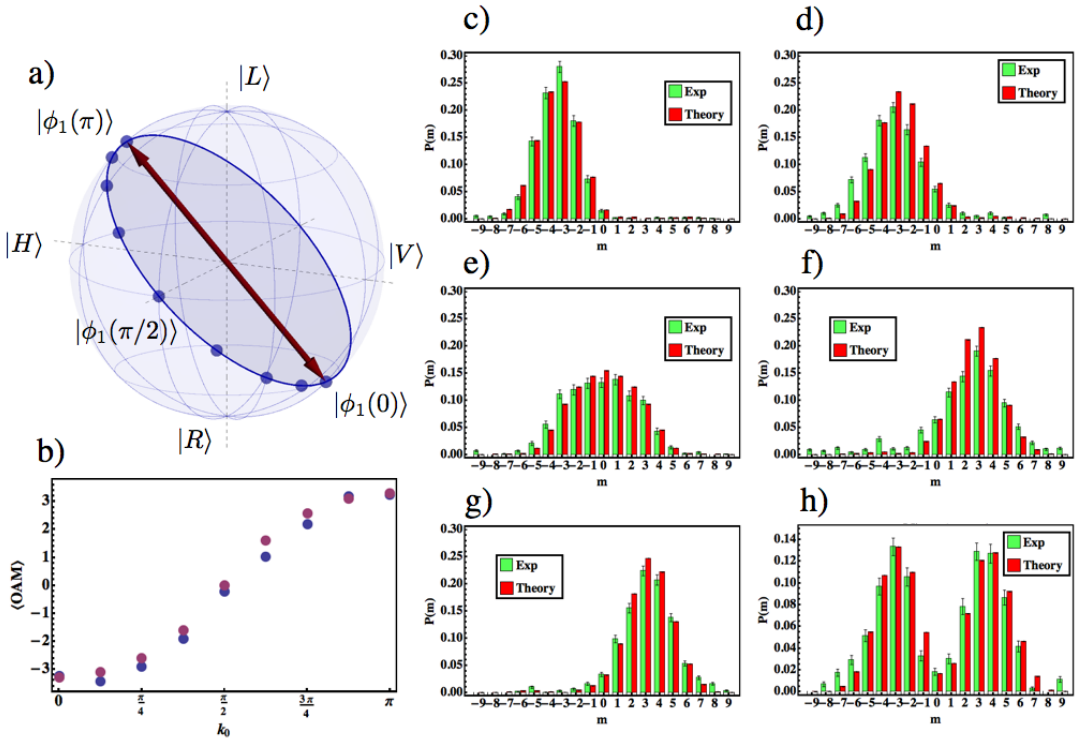

FIGURE 5.13: Quantum walk wave packet dispersion properties in the Brillouin zone [106]. a) Poincaré sphere representation of the polarization (or SAM) eigenstates $|\phi_1(k)\rangle$ prepared in our experiments, for different values of the quasi-momentum k in the irreducible Brilluoin zone $(0, \pi)$ taken in steps of $\pi/8$ (blue dots). These states lie on a maximal circle (blue line) of the sphere. b) Mean OAM after a five-steps QW for a single photon prepared in a Gaussian wave packet with $\sigma = 2$ and $s = 1$, with different values of average quasi-momentum k_0 in the range $(0, \pi)$. Blue and purple points are associated with experimental data and theoretical predictions, respectively; Poissonian statistical uncertainties are too small to be shown in the graph. c-g) Final OAM distributions associated with some of these cases (summed over different polarizations). Panels refer to $k_0 = 0, \pi/4, \pi/2, 3\pi/4, \pi$, respectively. h) OAM distribution after five-step QW for a wave packet whose coin is prepared in the superposition state $[|\phi_1(0)\rangle + |\phi_2(0)\rangle]/\sqrt{2}$. As predicted by the theory, it splits into two components propagating in opposite directions, thus generating a maximally-entangled SAM-OAM state. In panels c-h) Poissonian statistical uncertainties at plus-or-minus one standard deviation are shown by error bars. The similarity between experimental and theoretical OAM distributions are $(98.9 \pm 0.2)\%$, $(96.2 \pm 0.4)\%$, $(98.4 \pm 0.3)\%$, $(93.2 \pm 0.6)\%$, $(99.1 \pm 0.2)\%$ and $(97.3 \pm 0.4)\%$, respectively.

well. The idea of using QWs as simulators of such phenomena was proposed by Kitagawa *et al.* [119], who realized that these simple quantum dynamics could realize all topological phases of one and two dimensional systems of non interacting particles; as a first application of this concept, the formation of topologically protected bound states was observed in a photonic QW [120]. In this context, we developed a QW protocol characterized by a non-trivial topology; interestingly, the value of an external parameter determines the existence of two topological phases for the system, similarly to the

"split-step" protocol of Refs. [119, 120]. In terms of Hamiltonian symmetries and topological features, the system is equivalent to the S-S-H model for electron dynamics in the poly-acetylene chain [142]. Topological phase transitions in these systems are usually investigated in non-uniform systems, in which localized states are observed at the edge between the regions characterized by distinct topologies. In contrast we consider here homogeneous open systems, where the topological phase is uniform over all the lattice. In this case, we realized that a signature of the topological features of the QW is present in the moments of the walker distribution. Indeed, as it will be proved below, they show abrupt variations at the critical points.

5.6.1 A QW protocol with two distinct topological phases

Let use consider the single step operator $\widehat{U}_0(\delta)$ corresponding to a sequence of a QP, followed by QWP oriented at 90° with respect to the horizontal direction; here δ is the optical retardation introduced by the q-plate. In this case, the 2×2 matrix associated with the step operator $\widehat{U}_\delta(k)$ in momentum space is given by

$$U_\delta(k) = \frac{1}{\sqrt{2}} \begin{pmatrix} \cos\left(\frac{\delta}{2}\right) + \sin\left(\frac{\delta}{2}\right) e^{-i\,k} & -i\,\cos\left(\frac{\delta}{2}\right) + i\,\sin\left(\frac{\delta}{2}\right) e^{-i\,k} \\ -i\,\cos\left(\frac{\delta}{2}\right) + i\,\sin\left(\frac{\delta}{2}\right) e^{i\,k} & \cos\left(\frac{\delta}{2}\right) + \sin\left(\frac{\delta}{2}\right) e^{i\,k} \end{pmatrix}. \tag{5.25}$$

where we are referring to the circular basis in the polarization space. Being the optical retardation of the q-plate, δ is a periodic quantity, so we can limit our analysis to the case $\delta \in \{0, 2\pi\}$. Using Eq. 5.16, we get the dispersion relation for this system:

$$\omega_\delta(k) = \cos^{-1}\left(\frac{\cos\left(\frac{\delta}{2}\right) + \sin\left(\frac{\delta}{2}\right)\cos k}{\sqrt{2}}\right). \tag{5.26}$$

The components of the vector $\hat{\mathbf{u}}_\delta(k)$ appearing in Eq. 5.15 are given by

$$\begin{aligned} u_1(k) &= \{\cos(\delta/2) - \sin(\delta/2)\cos k\}/N(k) \\ u_2(k) &= -\sin(\delta/2)\sin k/N(k) \\ u_3(k) &= -u_2(k) \end{aligned} \tag{5.27}$$

where the quantity N is a normalization factor

$$N(k) = \sqrt{2\,\{1 - \cos^2[\omega_\delta(k)]\}}. \tag{5.28}$$

As for the Hadamard walk, we can observe that the $\hat{\mathbf{u}}_\delta(\omega)$ is related to the group velocity $V_\delta(k) = \mathrm{d}\,\omega_\delta(k)/\mathrm{d}k$; in particular, we have that

$$u_3(k) = V_\delta(k). \tag{5.29}$$

In Fig. 5.14 we plot the energy ω_δ and group velocity V_δ as function of k in the Brillouin

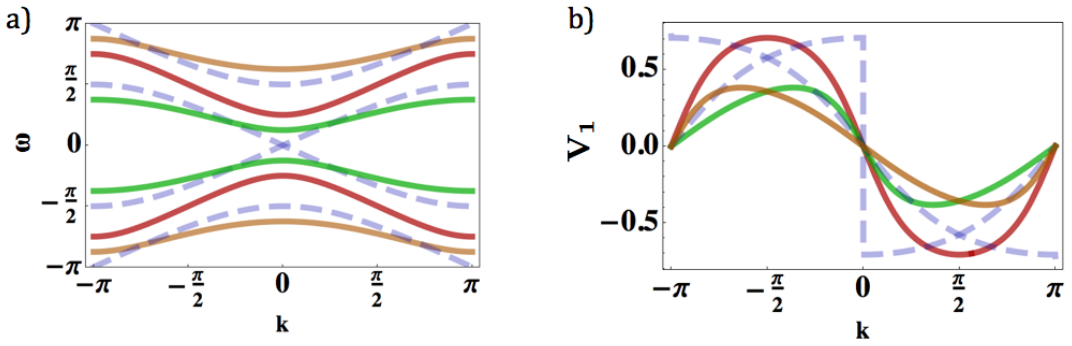

FIGURE 5.14: Dispersion relations for the hybrid QW protocol, obtained when varying the control parameter δ. The dispersion curves for the two bands depend on the external parameter δ. Here we report few examples; coloured green, red and orange curves are obtained for values of δ equal to $\pi/4$, π and $7\pi/4$, respectively. Here we report few examples; coloured green, red and orange curves are obtained for values of δ equal to $\pi/4$, π and $7\pi/4$, respectively. These few examples show a general feature of this system, i.e. the existence of a finite energy gap between the energies of the two bands (see panel a)) . Only at the two critical points $\delta = \delta_1 = \pi/2$ and $\delta = \delta_2 = 3\pi/2$ (the blue dashed lines) the gap vanishes for $k = 0$ and $k = \pi$, respectively, causing the presence of a discontinuous jump in the group velocity (see panel b)).

zone. In particular, it can be noted that the dispersion relations (Fig. 5.14a) show two gapped bands, where the energy gap depends on the parameter δ. There exist two values for the latter, that is $\delta_1 = \pi/2$ and $\delta_2 = 3\pi/2$, where this gap vanishes at $k = 0$ and $k = \pi$, respectively; at these points, the function $\omega_\delta(k)$ is characterized by a second order discontinuity, and locally the dispersion becomes linear. Accordingly, the group velocity dispersion (Fig. 5.14b) is discontinuous at $\delta = \delta_1$ and $\delta = \delta_2$, showing finite jumps at the crossing of the singular points $k = 0$ and $k = \pi$, respectively. We may divide the possible values of δ in two sets $P_0 = \{0, \pi/2\} \cup \{3\pi/2, 2\pi\}$ and $P_1 = \{\pi/2, 3\pi/2\}$, whose boundaries correspond to the points characterized by the gap closure. A simple question arises: is there anything that makes these sets different? The answer is yes, and in order to understand why we may consider the states $|\phi_s(k)\rangle$, or equivalently $\hat{\mathbf{u}}_\delta(k)$, that is the eigenstates of the coin part of the evolution operator. In Fig. 5.15 we plot these states on the Poincaré sphere associated with the coin space $\mathcal{H}_c$, when varying k in the interval $\{-\pi, \pi\}$. First of all, it is possible to note that $|\phi_s(k)\rangle$ lie on a great circle of the sphere, orthogonal to the vector $\hat{\mathbf{a}} = \{0, \sin(\pi/8), \cos(\pi/8)\}$, which is a

constant independent of the value of δ. This is a consequence of the chiral symmetry which is present in the system [119], as for the Hadamard QW introduced previously. As explained in the caption of the figure, for any value of δ we can characterize the QW system in terms of the closed loops formed by the coin eigenstates, when varying k in the Brillouin zone. This winding number W is a $\mathbb{Z}$ invariant, since in principle it can be equal to any relative number. As discussed before, the invariance we are considering takes into account only continuous deformations which do not alter the chiral symmetry (symmetry-protected invariance). In Fig. 5.15 we can observe that eventually P_0 and P_1 are characterized by different values of W, which is equal to 0 and 1, respectively. P_0 and P_1 are usually referred to as distinct topological phases, due the the topological nature of the invariant W; in particular, P_0 is the trivial phase, while P_1 is considered as the non-trivial phase. Interestingly, this is the same topological characterization emerging in the S-S-H model for the poly-acetylene system [119, 142]. In this framework, we

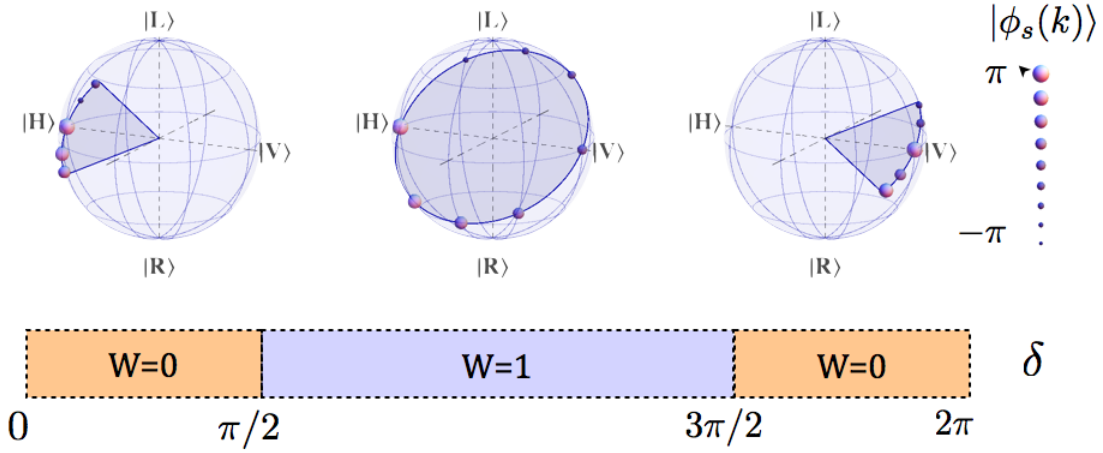

FIGURE 5.15: Poincaré sphere representation of the eigenstates of the coin part of the step operator $\widehat{U}_\delta$ (5.25), when varying the quasi-momentum k in the Brillouin zone. As shown in the legend of the figure, states $|\phi_s(k)\rangle$ are represented as points whose dimensions are associated with the value of the quasi-momentum k. The chiral symmetry of the system forces this states to lie on a great circle of the sphere. When varying k form $-\pi$ to π, the state $|\phi_s(k)\rangle$ will describe a closed trajectory; for the latter, different homotopy classes exist, characterized by the number of windings W. In our protocol, the value of δ determines the existence of two regimes; $W = 0$ when $\delta \in \{0, \pi/2\}$ and $\delta \in \{3\pi/2, 2\pi\}$, whereas $W = 1$ when $\delta \in \{\pi/2, 3\pi/2\}$. As discussed in the main text, W is a topological invariant, under continuos deformation that do not break the chiral symmetry. As a consequence, the regions $W = 0$ and $W = 1$ are considered as distinct topological phases.

investigated the properties of the moments of the probability distribution for the walker position $P(x)$, with particular attention to the behavior of these quantities at the phase transition between P_0 and P_1. Recalling that the j-th moment $M_j = \langle \widehat{x}^j \rangle$ is defined as

follows

$$M_j = \sum_x x^j \, P(x) \tag{5.30}$$

we considered a QW for a system initially prepared in the state $|\psi_0\rangle = |\phi_0\rangle_c \otimes |0\rangle_w$, whose coin part is generic, while the walker term is localized in the site $x = 0$. For these states, we considered the QW evolution after n steps; as already known, the dominant term of the associated moments at the exit of the walk, proportional to n^j, describes the ballistic behavior of the process. Interestingly, we have found that this contribution has a simple expression in terms of the group velocity of the system. In particular, for the first and the second moments (all the others have similar properties), we proved that;

$$M_1/n = (s_2 - s_3)\, L(\delta) + o(1/n) \tag{5.31}$$

$$M_2/n^2 = \; L(\delta) + o(1/n^2) \tag{5.32}$$

where s_2 and s_3 are the expectation values of the coin operators $\widehat{\sigma}_2$ and $\widehat{\sigma}_3$, calculated with respect to the initial state $|\phi_0\rangle$. The quantity $L(\delta)$ appearing in Eqs. 5.31 and 5.32 has an elegant expression, given by

$$L(\delta) = \int_{-\pi}^{\pi} \frac{\mathrm{d}k}{2\pi} \left[V_\delta(k)\right]^2 . \tag{5.33}$$

These results can be derived conveniently by evaluating M_1 and M_2 in momentum representation, where they are defined as follows:

$$\begin{aligned} M_1 &= \int_{-\pi}^{\pi} \frac{\mathrm{d}k}{2\pi} \langle\phi_0| \left(\widehat{U}^\dagger\right)^n - i\frac{\mathrm{d}}{\mathrm{d}k}\widehat{U}^n|\phi_0\rangle, \\ M_2 &= \int_{-\pi}^{\pi} \frac{\mathrm{d}k}{2\pi} \langle\phi_0| \left(\widehat{U}^\dagger\right)^n (-i)^2 \frac{\mathrm{d}^2}{\mathrm{d}k^2}\widehat{U}^n|\phi_0\rangle. \end{aligned} \tag{5.34}$$

Expanding the evolution operator as

$$\begin{aligned} U^n(k) &= \mathrm{Exp}\left\{-i\, n\, \omega(k)\, \hat{\mathbf{u}}(k)\cdot\hat{\boldsymbol{\sigma}}\right\} \\ &= \cos\left\{n\,\omega(k)\right\}\, I_2 - i\, \sin\left\{n\,\omega(k)\right\}\, \hat{\mathbf{u}}(k)\cdot\hat{\boldsymbol{\sigma}} \end{aligned} \tag{5.35}$$

where I_2 is the identity matrix in 2D, and the components of $\hat{\mathbf{u}}_\delta(k)$ are those reported in Eq. 5.27, it is straightforward to obtain Eqs. 5.31-5.32. Eq. 5.32 is derived without using the explicit expressions for the quantities ω_δ and $\hat{\mathbf{u}}_\delta$. On the other hand, the general expression for $M1/n$ is

$$M_1/n = \int_{-\pi}^{\pi} \frac{\mathrm{d}k}{2\pi}\, V_\delta(k)\, \langle\phi_0|\, (\hat{\mathbf{u}}(k)\cdot\hat{\boldsymbol{\sigma}})\, |\phi_0\rangle + o(1/n). \tag{5.36}$$

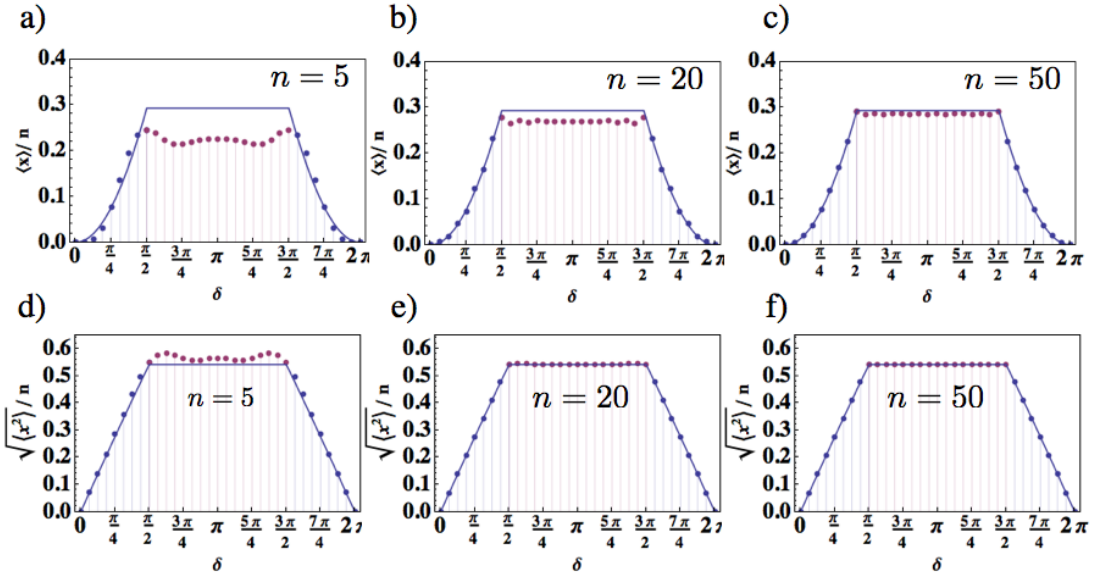

FIGURE 5.16: Analysis of the first and second order moments $\{M1, M_2\}$ of the probability distribution for the walker, after a n-steps QW. The system, initially prepared in the state $|\psi_0\rangle = |\phi_0\rangle_c \otimes |0\rangle_w$, undergoes a QW described by the step operator (5.25). For every plot, purple points are obtained from a numerical simulation, when varying δ with steps of $\pi/16$ in the range $\{0, 2\pi\}$; continuous blue lines represents the quantity $L(\delta)$ [panels a-c)], or $\sqrt{L(\delta)}$ [panels d-f)] (see Eq. 5.37). For the simulation, we prepared the coin in the state $\{s_1, s_2, s_3\} = \{0, 0, 1\}$. Panels a-c) First order moment $M1$, divided by the number of steps of the walk, as a function of the parameter δ, for a walk of 5, 20, and 50 steps, respectively (this number is reported inside each figure). As n increases, simulated data converge to the values predicted by Eq. 5.31. Panels d-f) Square root of the second order moment, divided by the number of steps n. The figures are organized as in panels a-c). In this case, we can observe that simulated data converge much faster to the asymptotic values reported in Eq. 5.32, with a discontinuity emerging even for a walk of few steps.

When evaluating the latter equation considering the vector $\hat{\mathbf{u}}_\delta(k)$ reported in Eq. 5.27, and exploiting the property $u_3 = V_\delta$, we get Eq. 5.31. In the specific case of our QW model, the integral appearing in Eq. 5.33 can be solved analytically. The procedure to find the solution is made of two steps; first of all, it is required to pass to the new variable $t = \mathrm{Tan}\,(k/2)$, and, accordingly, evaluate the integral between $-\infty$ and $+\infty$. The corresponding integral can be solved by residue method, choosing the real axis as integration path in the complex t-plane, closed at $\pm\infty$ by the upper half circle[4]; the final result is

$$L(\delta) = \begin{cases} 2\sin^2(\delta/4) & 0 < \delta < \pi/2 \\ 1 - 1/\sqrt{2} & \pi/2 \leq \delta \leq 3\pi/2 \\ 2\cos^2(\delta/4) & 3\pi/2 < \delta < 2\pi \end{cases} \tag{5.37}$$

Before analyzing the properties of the quantity $L(\delta)$, it is interesting to observe that both M_1 and M_2 are proportional to L, which is related to the square of the group

[4]This approach was devised by E. Santamato. Explicit calculations are omitted for brevity.

velocity. While this seems to be natural for M_2, it is not so obvious that the same dependance affects the first order moment too. Moreover, M_1 is strongly dependent on the initial state of the coin part of the system, and it vanishes along the great circle $s_2 = s_3$. Differently, M_2 is a constant of the system, depending only on the external parameter δ.

As a consequence of the discontinuity affecting the dispersion relation at the phase transition values δ_1 and δ_2, the function $L(\delta)$ has a similar behavior, which can be observed in Fig. 5.16. Interesting, L is equal to a constant in the non-trivial phase P_1. The link between the moments of the walker distribution and the integral of the square of the group velocity is the main result of our analysis, accompanied with the observation that such quantity is discontinuous at the phase transition.

Discontinuities of physical quantities at the transition between different phases is a typical property of these kind of phenomena. In the context of topological phases associated with chiral symmetry in 1D systems, we propose to use the moments M_j as figures of merit of the phase change; moreover, we conjecture that other systems behave similarly, being these features strongly related to the gap closure of the energy bands, which is typical for such phenomena. In a QW architecture, we highlighted these features experimentally, monitoring the values of the first and second order moments as the system is driven from one phase to the other.

5.6.2 Topological phases and moments analysis in a photonic QW with twisted photons.

In the previous chapter we have seen that two distinct topological phases are present in a QW system whose step operator is realized using a QWP oriented at 90° and a QP; here we describe the experiment we implemented to investigate moments of the probability distribution of the walker, which are affected by abrupt variations at the phase change when the number of steps of the walk is high.

The layout of the apparatus is shown in Fig. 5.17. As usual, the QW simulation is operated in the heralded single-photon quantum regime (see Appendix B). The heralded photon entering the QW setup is initially prepared in a separable state $|\psi_0\rangle = |0\rangle_o \otimes |\phi_0\rangle_\pi$, where $|\phi_0\rangle = \alpha|L\rangle + \beta|R\rangle$; the two complex coefficients α and β (with $|\alpha|^2 + |\beta|^2 = 1$) can be selected at will by a QWP-HWP set (apart from an unimportant global phase). The photon then undergoes the QW evolution and, at the exit, is analyzed in both polarization and OAM so as to determine the output probabilities and the associated moments. Letting δ vary in the range $\{\pi/8, \pi\}$ with steps of $\pi/16$, we determined the corresponding probability distribution of the walker after the 6-steps QW. In Fig.

5.18a we report the probability distribution as measured for the initial state $\{\alpha, \beta\} = 1/\sqrt{2}\{1, 1\}$, in a QW with $\delta = 2.95$. The agreement with the expected distributions is estimated by calculating the "similarity", as defined in Eq. 5.10. In Fig. 5.18b-c we plot the measured values of M_1/n and $\sqrt{M_2}/n$, respectively, as a function of the parameter δ. In good agreement with theoretical predictions, the emergence of a discontinuity at $\delta = \pi/2$ can be observed when considering $\sqrt{M_2}/n$. Preparing the initial state of the coin (m=0 for the walker) in two non-orthogonal polarizations (the specific states are reported in the caption of Fig. 5.18) we verified that the value of M_2 was not affected by this choice, as expected from Eq. 5.32; on the contrary, the same is not true for M_1. In this context, we repeated the experiment for many initial states (but only for specific values of δ), in order to highlight that M_2 is constant with respect to this choice. We prepared the initial polarization of single photons so as to correspond to specific points along the meridian $\phi = 0$ of the Poincaré sphere, and performed the experiment for four values of δ (two for each topological sector, as reported in the caption of the figure). Measured data, reported in Fig. 5.18d, match well the predicted results.

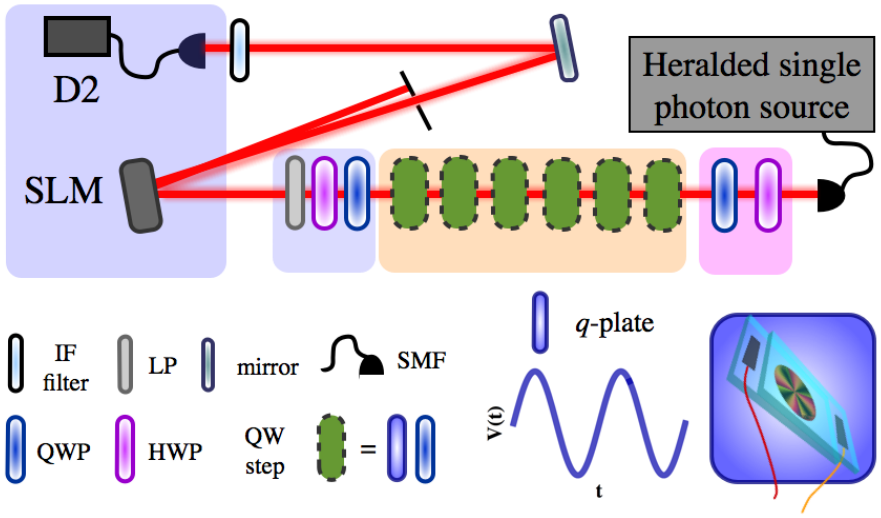

FIGURE 5.17: Experimental setup. Heralded single photons are produced at the input of the setup as described in Appendix B. The trigger photon is directly sent to an avalanche photodiode (D1) [this part is not shown in the figure] while the heralded one, after passing trough the QW system, is analyzed in polarization and OAM and finally detected by APD D2, in coincidence with D1. Before the QW, the photon exiting the fiber in the OAM state $m = 0$ passes through a HWP-QWP set, used for preparing the initial polarization. Then it goes through the 6-steps QW, with the single step consisting of a q-plate and a QWP oriented at 90°. At the exit of the QW, a polarization projection is realized by means of a second HWP-QWP set followed by a linear polarizer (LP). The OAM state is then analyzed by diffraction on a spatial light modulator (SLM), followed by coupling into a SMF. Before detection, interferential filters (IF) centered at 800 nm and with a bandwidth of 3.6 nm are used for spectral cleaning.

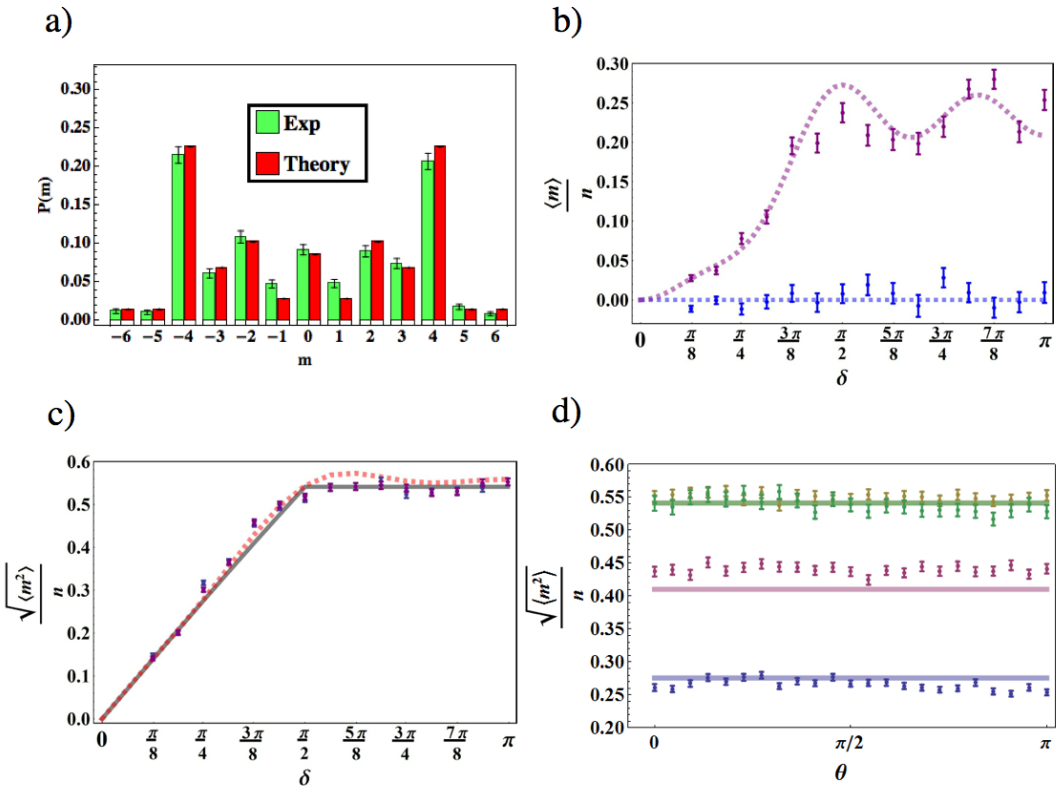

FIGURE 5.18: Experimental results. a) Measured (green, left) and expected (red, right) probability distributions after a 6 steps QW of a photon initially prepared in the state $m = 0$ and $\{\alpha, \beta\} = 1/\sqrt{2}\{1, 1\}$, when $\delta = 2.95$. The error bars represent statistical errors at one standard deviation, calculated assuming Poissonian fluctuations on single counts. The similarity between the experimental and the expected distributions is 99.2 ± 0.2. b-c) Measured values of M_1 and $\sqrt{M_2}/n$, respectively, when varying $\delta \in \{\pi/8, \pi\}$ with steps of $\pi/16$, for initial states $\{\alpha, \beta\} = 1/\sqrt{2}\{1, 1\}$ (blue dots), and $\{\alpha, \beta\} = \{0, 1\}$ (purple dots). Dashed lines represent the expected values for the plotted quantities, as obtained from numerical simulations. In panel b), the continuous line represents the asymptotic limit reported in Eq. 5.32. d) Measured values of M_2 when the initial polarization corresponds to the state $\cos(\theta/2)|L\rangle + \sin(\theta/2)|R\rangle$, with varying the polar angle $\theta \in \{0, \pi\}$ with steps of $\pi/22$; data are collected in correspondence of $\delta = \pi/4$ (blue), $\delta = 3\pi/8$ (purple), $\delta = 3\pi/4$ (yellow), $\delta = \pi$ (green).

Conclusions

Light-based technologies take advantage of the multiple degrees of freedom that characterize the e.m. radiation. Among these, we considered the "angular momenta", highlighting the physical distinction between the associated spin and orbital components. Big efforts in the last century led to the development of a variety of tools to handle such physical quantities, making them available for concrete applications. Relying on such existing tools, in this work we devised new schemes for exploiting spin and orbital angular momenta of light in several scenarios. In particular, we looked at these quantities from two different points of view. On one hand, being related to specific features of light, we manipulated the SAM and the OAM in order to tailor suitably the beam properties, accessing peculiar states of the e.m. field (structured light). On the other hand, we considered the SAM and the OAM as the physical realization of quantum systems (qu-bits and qu-dits for the SAM and the OAM, respectively). In both scenarios, we focused our attention on the effects of a controllable coupling between the two degrees of freedom. Most of the research described here relies on a specific device called q-plate, that we build in our laboratories. This allows one to engineer a spin-orbit interaction in a light beam, and, in specific cases, to generate pure OAM states.

In the domain of classical optics, we demonstrated a simple scheme which allows one to generate vector beams, in particular those characterized by the fundamental polarization singularities, that is the lemon and the star C-points. Remarkably, this approach is very simple, relying only on a single q-plate and a set of wave-plates. As a difference with respect to previous works, we gave here a first demonstration of the use of one of the parameters which define the action of a q-plate, that is the optical retardation δ. In this scenario, more complex states could be realized by using devices with high topological charges, or engineering these plates so as to modulate the radial structure of the field.

In the domain of quantum optics, the interaction between SAM and OAM results in the entanglement between the two degrees of freedom. Considering a 2D subspace of the infinite dimensional OAM space, jointly with the 2D SAM space, we realized single photon states characterized by tunable SAM-OAM entanglement. Non-classical correlations in this kind of systems have been widely exploited to rule out hidden variable

models, which were proposed after the EPR paradox to complete the quantum theory. In our case, we relied on maximally entangled states to demonstrate the violation of the so called Leggett inequalities, ruling out a possible description of the physical reality in terms of the contextual hidden variable models considered in the Leggett's theory. Concerning non-contextual models, we used partially entangled states to demonstrate the Hardy paradox, which highlights the contradictions arising when describing quantum systems using deterministic variables, as in the hidden variable theories.

Spin and orbital angular momenta of light can be exploited to encode high-dimensional quantum systems. As a specific application of this concept, we demonstrated the realization of mutually unbiased bases in a 6D Hilbert space, using both combinations of SAM qu-bits and OAM qu-trits and pure OAM qu-six.

Finally, we introduced the idea of considering the spin-orbit space of light for carrying out quantum simulations. In particular, we focused our attention on the quantum walk, which is a process emerged in recent years as the quantum analog of the classical random walk. We simulated such quantum evolution in the spin-orbit space of light, for both one and two indistinguishable photons. Taking advantage of a specific feature of our architecture, we realized OAM Gaussian wave packets that we used to probe the QW band structure. Among the variety of areas where QWs have been considered as a promising resource, we focused our attention on the quantum simulation of topological phases of non-interacting particles. In this context, we devised a new QW protocol which shows two different topological phases, according to the value of a controllable external parameter (interestingly, this is the q-plate retardation δ). We have shown that, if considering the probability that the system occupies each lattice site at the exit of the walk, the moments of the associated distribution are affected by abrupt variations at the phase change. We developed the simple theory that describes these features, linking the OAM distribution moments to the QW dispersion relations, and verified them in a dedicated experiment.

Current technology allows one to extend the approach that we proposed to more complex system, with the aim of studying phenomena which are typical of condensed matter system, such as topological phases. Nevertheless, we work towards the idea of including the radial coordinate as an extra degree of freedom of our platform. In this context, the development of novel q-plate-like devices, able to tailor the radial structure of a light beam (and eventually coupling it to the spin and to the orbital angular momentum), would pave the way to novel applications, not only in the domain of quantum simulations, but in all the fields that have been described in this thesis.

Appendix A

Jones matrices for wave plates

In this section we derive the expressions for the Jones matrices associated with a generic wave plate, both in linear and circular bases, considering the possibility that the plate is rotated with respect to the horizontal direction of the laboratory frame. First of all, let us consider a light beam propagating along the z axis of a cartesian frame, with the latter being oriented so as to have the x axis parallel to the optical table. In this reference frame, we associate linear horizontal and vertical polarizations with the x and y axes, respectively. The polarization state of a fully polarized light beam is described in terms of a 2D complex vector (the Jones vector), that is $\psi = (c_h, c_v)^T$. Here, we are explicitly referring to the basis of horizontal and vertical polarizations (HV); the other two relevant bases are reported in Eq. 1.26. In particular, we consider here the circular basis (LR), since it provides the simplest framework to express the action of the q-plate. When the components of the Jones vector are known in the HV basis, it is possible to determine the corresponding components in the LR basis, which are given by $(c_l, c_r)^T = U \cdot (c_h, c_v)^T$. The unitary matrix U, providing the mapping between the two bases, is expressed as follows:

$$U = \frac{1}{\sqrt{2}} \begin{pmatrix} 1 & -i \\ 1 & i \end{pmatrix}. \tag{A.1}$$

We recall that if $M_{(hv)}$ is the Jones matrix associated with an optical device in the HV basis, its expression in the LR basis is $M_{(lr)} = U\, M_{(hv)}\, U^\dagger$.

A wave plate is a slab of birefringent material. In the (x, y) plane, this is characterized by two orthogonal directions $\hat{\mathbf{e}}_f$ and $\hat{\mathbf{e}}_s$, usually referred to as fast and slow axes, respectively. In this context, let us consider the Jones vector $\psi = (c_f, c_s)$ in the linear basis corresponding to these two directions (FS). When a light beam passes through a wave plate, fast and slow components of the polarization acquire a relative phase retardation

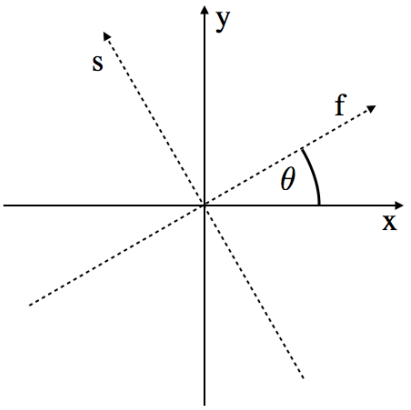

FIGURE A.1: Reference frame associated to the fast and slow axes of a wave plate, compared to the laboratory frames. The two are rotated with respect to each other by and angle θ. Labels f and s are associated with the fast and slow axes of the plate, respectively.

δ, given by

$$\delta = \frac{2\pi d(n_s - n_f)}{\lambda} \tag{A.2}$$

Here, d is the thickness of the plate, n_f and n_s are the refractive indices associated with the fast and the slow axes, respectively, and λ is the wavelength of the light beam. Wave plates with $\delta = \pi$ and $\delta = \pi/2$ are referred to as half-wave plates and quarter-wave plates, respectively. In such a representation, we can express the action of the wave plate through the Jones matrix L_δ

$$L_\delta = \begin{pmatrix} e^{-i\frac{\delta}{2}} & 0 \\ 0 & e^{i\frac{\delta}{2}} \end{pmatrix} \tag{A.3}$$

Typically fast and slow axes of a wave plate do not match the (x, y) directions of the laboratory, whereas $\{\hat{\mathbf{e}}_h, \hat{\mathbf{e}}_v\}$ and $\{\hat{\mathbf{e}}_f, \hat{\mathbf{e}}_s\}$ are rotated by an angle θ, as shown in Fig. A.1 . The expression of the Jones matrix L_δ in the laboratory frame is

$$L_\delta(\theta)_{h,v} = R(\theta) L_\delta R(-\theta) \tag{A.4}$$

where the rotation matrix $R(\theta)$ is defined as

$$R(\theta) = \begin{pmatrix} \cos\theta & -\sin\theta \\ \sin\theta & \cos\theta \end{pmatrix} \tag{A.5}$$

The signs of the coefficients of this matrix are obtained considering the rotation defined in Fig. A.1, linking (c_f, c_s) to (c_h, c_v), that is $(c_h, c_v)^T = R(\theta) \cdot (c_f, c_s)^T$. It is

straightforward to see that

$$L_\delta(\theta)_{(hv)} = \begin{pmatrix} \cos(\delta/2) - i\,\sin(\delta/2)\cos(2\theta) & -i\,\sin(\delta/2)\sin(2\theta) \\ -i\,\sin(\delta/2)\sin(2\theta) & \cos(\delta/2) + i\,\sin(\delta/2)\cos(2\theta) \end{pmatrix} \tag{A.6}$$

As a result, in the specific cases of a HWP and a QWP we have

$$H(\theta)_{(hv)} = -i \begin{pmatrix} \cos(2\theta) & \sin(2\theta) \\ \sin(2\theta) & -\cos(2\theta) \end{pmatrix} \tag{A.7}$$

$$Q(\theta)_{(hv)} = \frac{1}{\sqrt{2}} \begin{pmatrix} 1 - i\,\cos(2\theta) & -i\,\sin(2\theta) \\ -i\,\sin(2\theta) & 1 + i\,\cos(2\theta) \end{pmatrix} \tag{A.8}$$

Applying the transformation (A.1) to the expression (A.6) we obtain the Jones matrix for a wave plate in the basis circular basis:

$$L_\delta(\theta)_{(rl)} = U\,L_\delta(\theta)_{(hv)}\,U^\dagger = \begin{pmatrix} \cos(\delta/2) & i\,\sin(\delta/2)\,e^{-2i\theta} \\ i\,\sin(\delta/2)\,e^{2i\theta} & \cos(\delta/2) \end{pmatrix} \tag{A.9}$$

As for the HV basis, we give the explicit expression for the case of a HWP and a QWP in the LR representation.

$$H_\delta(\theta)_{(rl)} = \begin{pmatrix} 0 & i\,e^{-2i\theta} \\ i\,e^{2i\theta} & 0 \end{pmatrix} \tag{A.10}$$

$$Q_\delta(\theta)_{(rl)} = \frac{1}{\sqrt{2}} \begin{pmatrix} 1 & i\,e^{-2i\theta} \\ i\,e^{2i\theta} & 1 \end{pmatrix} \tag{A.11}$$

We can observe that the HWP action on a circular polarization corresponds to a flip of the handedness, with the introduction of a phase factor depending on the plate orientation. Whereas, a QWP is associated with an Hadamard matrix; its coefficients have the same modulus, whereas the relative phases can be adjusted through the angle θ.
We can extend Eq. A.9 to the case of a q-plate, which has the peculiar feature that the angle θ is not uniform in the (x, y) plane, whereas it has the following expression

$$\theta(\phi) = q\,\phi + \alpha_0 \tag{A.12}$$

with q being the plate topological charge and α_0 the value of θ at $\phi = 0$, as discussed in Sec. 1.7. The angle $\phi = \mathrm{ArcTan}\,(y/x)$ is the azimuthal coordinate. Using this property, we can immediately note that Eq. A.9 corresponds to the q-plate operator reported in Eq. 1.60.

Appendix B

The single photon source

The preparation of single photon states is a key element in the realization of this kind of experiments. There are multiple strategies to realize a single photon source; for instance, a simple approach would be to attenuate a laser beam until the arrival of single photons on the detectors can be resolved in time. Though simple, this scheme has some drawbacks, such as the impossibility to discriminate different sources of noise, as thermal light for instance. In our experiments, we adopt a different strategy, usually referred to as heralded photon technique. The latter is common to all single photon based experiments described in this thesis, and we provide here the details about this part of the experimental setup. The heralded photon technique relies on the simultaneous generation of two photons. After these have been separated in space, one of them is detected by means of a single photon-counting module D1, consisting usually in a avalanche photodiode. The other one is the "single photon" exploited as the physical system of the experiment, which is eventually revealed by detector D2 as a result of some projective measurements on its degrees of freedoms (SAM and OAM in our case); among all events recorded by D1, we select only the ones occurring in coincidence with the events detected by D2, filtering out all possible counts associated to thermal light or some noise due to the electronics. In simple words, a photon detected at D1 acts as trigger, heralding the presence of another photon at D2.

To realize such a kind of source, we exploit a nonlinear process called Spontaneous Parametric Down-Conversion (SPDC) [143, 144]. The experimental apparatus is shown in Fig. B.1. A pulsed laser beam in the fundamental TEM_{00} Gaussian mode is generated by a Titanium:Sapphire source (Ti:Sa); the wavelength of the emitted radiation is 800 nm, its average power is around 700 mW, the pulse duration is 100 fs and the repetition rate of the pulses is 82 MHz. A frequency doubled laser beam at 400 nm, 120 mW average power, is obtained through Second Harmonic Generation (SHG) in a nonlinear β-Barium Borate crystal (BBO), which is pumped by the fundamental beam at 800

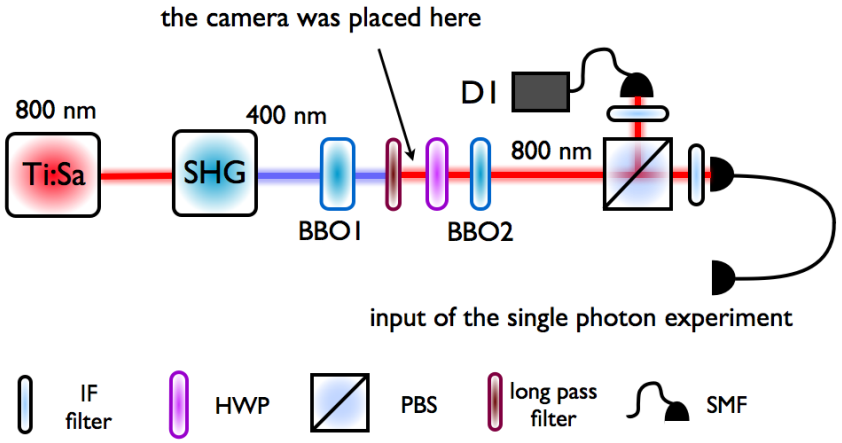

FIGURE B.1: Setup for the generation of photons pairs through Spontaneous Parametric Down-Conversion in a BBO nonlinear crystal. A 120 mw pulsed laser beam at 400 is pumping a BBO crystal (BBO1) where the SPDC process occurs). The pump beam was obtained through SHG in another BBO crystal, shined by the fundamental beam at 800 nm. After BBO1, a long-pass filter let only the photon pairs to be transmitted, while blocking the residual radiation at 400 nm. A HWP and a second BBO crystal (BBO2) are used for optimal compensation of both longitudinal and temporal walk-off, as discussed in the main text. By means of a PBS, signal and idler photons originating in BBO1 are spatially separated according to their polarization and then coupled into single mode optical fibers. The V-polarized photons is directly sent to an avalanche photodiode (D1), while the H-polarized one is sent the part of the setup mounted for the realization of the specific single photon experiment.

nm. After SHG, the residual part of the pump is filtered out using a pair of prisms and a short-pass filter (not shown in the picture). The SHG beam is pumping another BBO crystal (BBO1), where the SPDC process occurs. In a quantum interpretation, the latter basically consists in the absorption of a photon at 800 nm, and the simultaneous generation of two photons, called signal and idler, whose energy, momentum, polarization and spatial distribution depends on the features of the pump photon and the nonlinear crystal. This relation is provided by the phase matching condition, which is equivalent to the conservation of energy and momentum of light in the nonlinear process

$$\omega_p = \omega_s + \omega_i, \tag{B.1}$$

$$\vec{\mathbf{k}}_p = \vec{\mathbf{k}}_s + \vec{\mathbf{k}}_i, \tag{B.2}$$

where symbols p, s, i labels the pump, the signal and the idler photons, respectively. First of all, we use narrow bandpass interferential filter, centered at 800 nm, to realize

a degenerate architecture

$$\omega_s = \omega_i = \frac{\omega_p}{2} \tag{B.3}$$

In a type II configuration, we want the signal and the pump to share the same linear polarization, corresponding to the extraordinary polarization of the crystal in its transverse plane, whereas the idler is in the ordinary polarization state, which is orthogonal to the previous ones. In this case, using Eq. B.3, B.2 reads

$$2\, n_e(\theta)\, \hat{\mathbf{n}}_p = n_e(\theta)\, \hat{\mathbf{n}}_s + n_o\, \hat{\mathbf{n}}_i \tag{B.4}$$

where θ is the relative angle between the extraordinary axes and the pump propagation direction, while the unit vectors $\hat{\mathbf{n}}_j$ represent the propagation directions of the three photons. Since the BBO is a uniaxial crystal, only the extraordinary refractive index is depending on the orientation angle θ. For any value of the latter, there exist a set of directions $(\hat{\mathbf{n}}_s, \hat{\mathbf{n}}_i)$ which satisfy Eq. B.4. These directions describe the surface of two different cones, associated to the signal and the idler photons, which are displaced along the direction orthogonal to the polarization of the pump. The displacement of the cones and their aperture are determined by the value of θ, as shown in Fig. B.2. In this picture, we have detected single photons emitted in the SPDC process on the screen of an Electron Multiplying CCD camera (EMCCD camera) by Andor, which is positioned right after the BBO crystal at the exit of a long pass filter which removes the residual pump at 400 nm (this position is highlighted in Fig. B.1). The intersection of the cones and the screen of the camera give rise to characteristic rings. In our setup, the crystal was oriented so as to operate in the collinear regime (Fig. B.2 b)), using an aperture along the pump propagation direction and selecting only the intersection of the signal and idler cones.

As a result of the SPDC process that we implemented, two photons at 800 nm are generated simultaneously with the same momentum and orthogonal linear polarizations, corresponding to the horizontal and vertical directions. After passing through a HWP and a second BBO crystal (BBO 2), whose role will be discussed below, they are split according to their polarization by means of a PBS; the vertically polarized photon is reflected at the PBS and then coupled to a single mode optical fiber (SMF), which is directly connected to an avalanche photodiode (D1). The horizontally polarized photon is coupled to another SMF, which guides it to the input of the setup for the single photon experiment. Coincidences between detection events of the trigger and the heralded photons are counted through an electronic logic unit, characterized by a time window equal to 8 ns; this is sufficient to discriminate photons generated by consecutive pulses of the pump beam, whose temporal separation is equal to 12 ns. In some experiments

reported in this thesis the two photons were split after being coupled into the same optical fiber, which preserves the orthogonality of the corresponding polarization states; this configuration is completely equivalent to the one that we just presented (see Fig. 3.5 for a comparison).

The setup described in Fig. B.1 is suitable for the generation of two indistinguishable

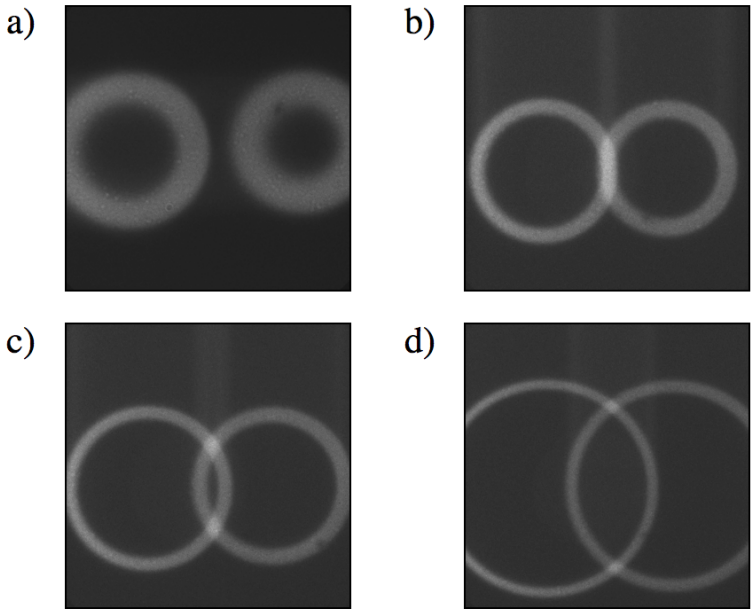

FIGURE B.2: Images of the SPDC rings formed by photons pairs generated in a BBO crystal, as detected by a CCD camera. Tilting the BBO crystal we can tune the phase matching conditions so as to change the dimensions of the rings; the latter can have no overlap, they can be tangent or they can cross in two points, as shown in panel a), b) and c-d), respectively. These pictures have been taken during an experiment performed in the laboratories of the quantum photonics group in the University of Ottawa, under the supervision of prof. Ebrahim Karimi and prof. Robert W. Boyd.

photons. As shown in Fig. B.3 a), a HWP and a second BBO crystal (BBO2), whose thickness is half with respect to BBO1, are placed to recover the indistinguishability of the signal and the idler photons; indeed propagation in the birefringent BBO1 introduces a temporal delay (temporal walk-off) between the two particles, which is about 300 fs. This quantity is estimated assuming that, on average, the SPDC occurs in the middle of BBO1. Such delay is larger than the pulse width, so idler and signal wave packets do not overlap anymore at the exit of the crystal. Moreover, double refraction causes a displacement of the extraordinary photon (longitudinal walk-off), which reduces the coupling efficiency of the photon pair in the SMF. The compensation of both temporal and longitudinal walk-off by means of a HWP and a second BBO crystal was proposed by Kwiat *et al.*[144]. The HWP is oriented at $\pi/4$, so as to exchange the polarization between the ordinary and the extraordinary cones. Then BBO2, oriented as BBO1, introduces a temporal and longitudinal displacement to the ordinary photon which was

not altered by BBO1; the magnitude of such displacements is comparable with the previous walk-off. To obtain the optimal orientation of the BBO2, we tested the temporal indistinguishability of the photon pairs coupled into the SMF, by performing an Hong-Ou-Mandel (HOM) test [145] in the polarization degree of freedom. As shown in Fig. B.3 a), at the exit of the fiber the two photons, whose polarization is described by the state $|\psi\rangle_{12} = |H_1, V_2\rangle$, passes through an HWP oriented at an angle θ, followed by a PBS. At the entrance of the latter, the biphoton state is

$$|\psi\rangle_{12} = \sin 2\theta \cos 2\theta \left(|H_1, H_2\rangle - |V_1, V_2\rangle\right) + \cos^2 2\theta \, |H_1, V_2\rangle - \sin^2 2\theta \, |V_1, H_2\rangle) \tag{B.5}$$

Here subscripts 1 and 2 label the two different photons; when these are not distinguishable, states ψ_{12} and ψ_{21} are physically equivalent. To test the HOM interference, we measure the coincidence counts between detectors D1 and D2, placed at the exit ports of the PBS. Given the state of Eq. B.5, the probability that the two photons exit from different ports is given by:

$$P_{12}^I = |\langle H_1, V_2|\psi_{12}\rangle + \langle V_1, H_2|\psi_{12}\rangle|^2 = \cos^2 4\theta \tag{B.6}$$

Being the two particles indistinguishable, states $|H_1, V_2\rangle$ and $|V_1, H_2\rangle$ are physically equivalent. It is easy to check that when $\theta = 22.5°$, the probability of a coincidence event vanishes. If distinguishable, the probability associated to the latter event is

$$P_{12}^D = |\langle H_1, V_2|\psi_{12}\rangle|^2 + |\langle V_1, H_2|\psi_{12}\rangle|^2 = 1 - \frac{1}{2}\sin^2 4\theta \tag{B.7}$$

As a difference with respect to the indistinguishable case, $P_{12}^D = 1/2$ when $\theta = 22.5°$. In Fig. B.3 b) we report the recorded coincidence counts when varying θ in the range $(0°, 46°)$, with steps of $2°$. The indistinguishability of the two photons can be quantified in terms of the visibility of interference dip; for this particular case, the latter is defined as

$$V = \frac{C_M - 2C_m}{C_M} \tag{B.8}$$

where C_M and C_m represent the maximum of the minimum values in the recorded coincidence counts, respectively. For our data, the visibility is larger than 90%, in agreement with the standard values for two-photon sources reported in the literature (see Ref. [146]).

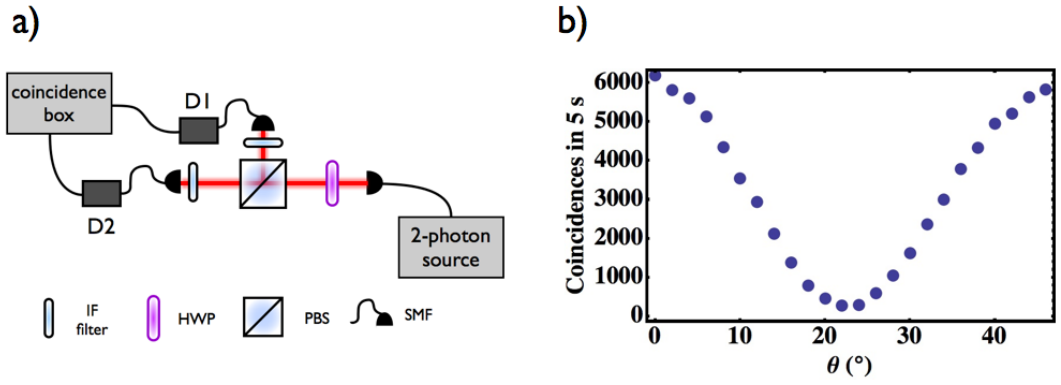

FIGURE B.3: Polarization Hong-Ou-Mandel interference between the two photons generated in the SPDC process, after optical compensation of the temporal walk-off. Panel a): experimental layout for the test of the two-photons indistinguishability. Photons pairs generated as shown in Fig. B.1 are coupled into a SMF; at the exit of the latter, a set of HWP and QWP is exploited to compensate the polarization alteration which both photons suffer when propagating in the fiber, which has a finite birefringence (these wave plates are not shown in the figure). The two photons, in the polarization state $|H_1, V_2\rangle$, pass through an HWP oriented at an angle θ, followed by a PBS. Transmitted and reflected photons are coupled into SMFs and sent to detectors D1 and D2, where they are detected in coincidence by means of a standard logic unit. Panel b): coincidences counts in 5 s between D1 and D2 for optimal compensation of the photons walk-off, measured when varying θ in the interval $(0, 46)^\circ$ with steps of 2°. The visibility of the dip is larger than 90%.

Appendix C

States forming MUBs in 2D, 3D and 6D Hilbert spaces

In dimension $d = 2$, the eigenstates of the three Pauli operators provide a complete set of MUBs, which can be represented by the columns of the following three matrices:

$$\pi_1 = \begin{pmatrix} 1 & 0 \\ 0 & 1 \end{pmatrix},\ \pi_2 = \frac{1}{\sqrt{2}} \begin{pmatrix} 1 & 1 \\ 1 & -1 \end{pmatrix},\ \pi_3 = \frac{1}{\sqrt{2}} \begin{pmatrix} 1 & 1 \\ \mathrm{i} & -\mathrm{i} \end{pmatrix}. \tag{C.1}$$

In $d = 3$, there exist four MUBs. We represent them here as the columns of the following four matrices:

$$\mathcal{O}_1 = \begin{pmatrix} 1 & 0 & 0 \\ 0 & 1 & 0 \\ 0 & 0 & 1 \end{pmatrix}, \quad \mathcal{O}_2 = \frac{1}{\sqrt{3}} \begin{pmatrix} 1 & 1 & 1 \\ 1 & \omega & \omega^2 \\ 1 & \omega^2 & \omega \end{pmatrix}$$
$$\mathcal{O}_3 = \frac{1}{\sqrt{3}} \begin{pmatrix} 1 & 1 & 1 \\ \omega & \omega^2 & 1 \\ \omega & 1 & \omega^2 \end{pmatrix}, \mathcal{O}_4 = \frac{1}{\sqrt{3}} \begin{pmatrix} 1 & 1 & 1 \\ \omega^2 & \omega & 1 \\ \omega^2 & 1 & \omega \end{pmatrix}, \tag{C.2}$$

where $\omega = \exp(\mathrm{i}2\pi/3)$.

In $d = 6$, we may construct three MUBs by a direct product of the π_1, π_2, π_3 bases and the corresponding first three bases $\mathcal{O}_1$, $\mathcal{O}_2$, $\mathcal{O}_3$:

$$I = \pi_1 \otimes \mathcal{O}_1, \quad II = \pi_2 \otimes \mathcal{O}_2, \quad III = \pi_3 \otimes \mathcal{O}_3. \tag{C.3}$$

These three 6D bases have the following matrix representation:

$$I = \begin{pmatrix} 1 & 0 & 0 & 0 & 0 & 0 \\ 0 & 1 & 0 & 0 & 0 & 0 \\ 0 & 0 & 1 & 0 & 0 & 0 \\ 0 & 0 & 0 & 1 & 0 & 0 \\ 0 & 0 & 0 & 0 & 1 & 0 \\ 0 & 0 & 0 & 0 & 0 & 1 \end{pmatrix} \tag{C.4}$$

$$II = \frac{1}{\sqrt{6}} \begin{pmatrix} 1 & 1 & 1 & 1 & 1 & 1 \\ 1 & \omega & \omega^2 & 1 & \omega & \omega^2 \\ 1 & \omega^2 & \omega & 1 & \omega^2 & \omega \\ 1 & 1 & 1 & -1 & -1 & -1 \\ 1 & \omega & \omega^2 & -1 & -\omega & -\omega^2 \\ 1 & \omega^2 & \omega & -1 & -\omega^2 & -\omega \end{pmatrix} \tag{C.5}$$

$$III = \frac{1}{\sqrt{6}} \begin{pmatrix} 1 & 1 & 1 & 1 & 1 & 1 \\ \omega & \omega^2 & 1 & \omega & \omega^2 & 1 \\ \omega & 1 & \omega^2 & \omega & 1 & \omega^2 \\ i & i & i & -i & -i & -i \\ i\omega & i\omega^2 & i & -i\omega & -i\omega^2 & -i \\ i\omega & i & i\omega^2 & -i\omega & -i & -i\omega^2 \end{pmatrix} \tag{C.6}$$

The 18 columns of these three matrices give the coefficients of the logical basis superpositions defining the 18 OAM states shown in Fig. 4.6a).

Appendix D

Role of the radial modes and Gouy phases in our QW platform[1]

Our QW realization relies on the encoding of the walker state in the transverse modes of light, in particular exploiting the azimuthal degree of freedom. For simplicity, the radial structure of the mode is not considered explicitly in our scheme. However, a full treatment of the optical process requires one to take the radial effects into account. Indeed, all optical devices used to manipulate the azimuthal structure and hence the OAM of light, including the QP, unavoidably introduce some alteration of the radial profile of the beam, particularly when subsequent free propagation is taken into account.

In this context, we choose Laguerre-Gauss (LG) modes as the basis, since they provide a set of orthonormal solutions to the paraxial wave equation. LG modes are indexed by an integer m and a positive integer p which determine the beam azimuthal and radial structures, respectively. Using cylindrical coordinates r, ϕ, z, these modes are given by

$$\mathrm{LG}_{p,m}(r,\phi,z) = \sqrt{\frac{2^{|m|+1}p!}{\pi w(z)^2\,(p+|m|)!}}\left(\frac{r}{w(z)}\right)^{|m|} e^{-\frac{r^2}{w(z)^2}} L_p^{|\ell|}\left(\frac{2r^2}{w(z)^2}\right) \tag{D.1}$$

$$\times\; e^{\left(\frac{i\pi r^2}{\lambda R(z)}\right)} e^{im\phi}\, e^{i(2p+|m|+1)\arctan\left(\frac{z}{z_R}\right)} \tag{D.2}$$

where λ is the wavelength, $w(z) = w_0\sqrt{1+(z/z_R)^2}$, $R(z) = z\left[1+(z/z_R)^2\right]$ and $z_R = \pi w_0^2/\lambda$ are the beam radius, wavefront curvature radius and Rayleigh range, respectively, w_0 being the radius at the beam waist [12]. $L_p^{|m|}(x)$ are the generalized Laguerre polynomials.

[1] This appendix correspond to a section of the Supplementary Material of Ref. [106], which I coauthored.

TABLE D.1: Power coefficients of the various p-index terms appearing in the expansion of the beam emerging from a QP (with $q = 1/2$) in the LG-mode basis, assuming that the input is an L-polarized LG mode with $p = 0$ and the given OAM m value.

OAM	$\lvert c_0\rvert^2$	$\lvert c_1\rvert^2$	$\lvert c_2\rvert^2$	$\lvert c_3\rvert^2$
$m = 0$	0.785	0.098	0.036	0.019
$m = 1$	0.883	0.073	0.020	0.008
$m = 2$	0.920	0.057	0.012	0.004
$m = 3$	0.939	0.046	0.008	0.002

As already discussed, the QP raises or lowers the OAM content of the incoming beam, according to its polarization state. Due to presence of the singularity at the origin, the QP also alters the radial index of the incoming beam. The details of these calculations are reported in Ref. [50]. Based on this analysis and assuming a low birefringence of the liquid crystals, a *tuned* QP (i.e. with $\delta = \pi$) transforms a circularly polarized, e.g. left-handed, input $\mathrm{LG}_{0,m}(r, \phi, 0)$ beam as follows:

$$\widehat{Q}_\pi \mathrm{LG}_{0,m}(r,z)|L,m\rangle = -i\,\mathrm{HyGG}_{|m|-|m+1|,m+1}(r,z)|R,m+1\rangle, \tag{D.3}$$

where $\mathrm{LG}_{0,m}(r, 0)$ (without the ϕ variable) denotes the radial part of the $\mathrm{LG}_{0,m}(r, \phi, 0)$ mode (i.e. with $\phi = 0$), $\mathrm{HyGG}_{p,m}(r, z)$ stands for the amplitude of Hypergeometric-Gauss (HyGG) modes [11] and the azimuthal term $e^{im\phi}$ has been replaced by the ket $|m\rangle$. Introducing dimensionless coordinates $\rho = r/w_0$ and $\zeta = z/z_R$, these modes are given by

$$\begin{aligned}\mathrm{HyGG}_{pm}(\rho,\zeta) &= i^{|m|+1}\sqrt{\frac{2^{p+|m|+1}}{\pi\Gamma(p+|m|+1)}}\frac{\Gamma\left(1+|m|+\frac{p}{2}\right)}{\Gamma\left(|m|+1\right)} \\ &\times \zeta^{\frac{p}{2}}(\zeta+i)^{-(1+|m|+\frac{p}{2})}\rho^{|m|}\,e^{-\frac{i\rho^2}{(\zeta+i)}}\,{}_1F_1\left(-\frac{p}{2},1+|m|;\frac{\rho^2}{\zeta(\zeta+i)}\right)\end{aligned} \tag{D.4}$$

where $\Gamma(x)$ is the gamma function and $F_1(a, b; x)$ is a confluent hypergeometric function. In order to determine the radial mode alteration introduced by the QP, we can expand the output beam in the LG modes basis, i.e. $\mathrm{HyGG}_{|m|-|m+1|,m+1} = \sum_p c_p \mathrm{LG}_{p,m+1}$ [11]. The expansion coefficients are given by

$$c_p = \sqrt{\frac{1}{p!\,m!\,(p+|m+1|)!}}\,\frac{(|m+1|+|m|)!\,\Gamma\left(p+\frac{|m+1|-|m|}{2}\right)}{\Gamma\left(\frac{|m+1|-|m|}{2}\right)} \tag{D.5}$$

Table D.1 shows the squared coefficients of this expansion for input beams possessing different OAM values. As can be seen, the effect of the QP on the radial mode decreases for beams having higher OAM values, so that only the $p = 0$ coefficient that was already present at the input retains a large value after the QP, and one can approximately

neglect higher-p terms. If the final detection based on coupling in a single-mode fiber filters only this term, then the presence of the other terms only introduces a certain amount of losses in the system. Hence, within such approximation, the p quantum number plays essentially no role and it can be ignored (except for the Gouy phase, which is discussed further below).

Even stronger is the argument one can use if the entire QW simulation takes place in the optical near field. Indeed, at the pupil plane ($\zeta \to 0$) the expression for the amplitude of HyGG and LG modes simplifies to

$$\begin{aligned} \mathrm{LG}_{p'm'}(\rho,0) &\propto L_p^{|\ell|}(\rho^2)\rho^{|m|}e^{-\rho^2} \\ \mathrm{HyGG}_{pm}(\rho,0) &\propto \rho^{p+|m|}e^{-\rho^2}. \end{aligned} \tag{D.6}$$

Combining Eq. D.3 and Eq. D.6, it is straightforward to prove that the action of a QP placed at the pupil plane of the beam is given by

$$\widehat{Q}_\pi \mathrm{LG}_{0,m}(\rho,0)|L,m\rangle = -i\,\mathrm{LG}_{0,m}(\rho,0)|R,m+1\rangle. \tag{D.7}$$

In other words, at the immediate output of the device, the QP ideally results only in the increment of the OAM content, without any alteration of the radial profile. This result remains approximately valid as long as the beam is in the near field, that is for $\zeta \ll 1$, except for a region very close to the central singularity and for some associated fringing that occurs outside the singularity. Both these effects can be neglected for $\zeta \ll 1$, as the overlap integral of the resulting radial profile with the input Gaussian profile remains close to unity (for example, at $\zeta = 0.1$ this overlap is still about 0.93 for a HyGG mode with $m = 1$). We exploit this property to minimize any effect due to a possible coupling between the azimuthal and the radial degree of freedom introduced by the QP. The setup was built in order to have all the steps of the QW in the near field of the input photons. To achieve this, we prepared the beam of input photons to have $z_R > 10$ m, while the distance between the QW steps was $d \approx 10^{-2} z_R$. For realizing a QW with high number of steps, a lens system could be used to image the output of each QW unit at the input of the next one; in this way the whole process may virtually occur at the pupil, i.e. at $\zeta = 0$, thus effectively canceling all radial-mode effects.

Free space propagation of photonic states carrying OAM is characterized by the presence of a phase term, usually referred to as Gouy phase, that evolves along the optical axis. Considering for example LG states of Eq. D.1, this phase factor is given by $\exp\left[-i(2p + |m| + 1)\arctan\left(z/z_R\right)\right]$, where z is the coordinate on the optical axis with respect to the position of the beam waist. The different phase evolution occurring for different values of $|m|$ could be a significant source of errors in the QW implementation. Let

us assume that after step n in the QW setup the state of the photon is $|\psi\rangle = \sum_m c_m|m\rangle$, where for simplicity we consider only modes with $p = 0$. When entering the following step, the coefficients c_m will evolve to $c'_m = e^{-i2|m|\arctan(d/z_R)}c_m$, where d is the distance between two steps along the propagation axis. At the step $n + 1$, coefficients c_m and c'_m lead to different interferences between the OAM paths, altering the features of the QW process. In our implementation we made this effect negligible by relying on the condition $d/z_R \ll 1$: indeed, as discussed previously, in our setup we had that $z_R > 10$ m and $d \simeq 10$ cm. Again, an alternative strategy could be based on using a lens system to image each QP on the following one; at image planes all relative Gouy phases vanish.

Let us conclude by noting that the need to remain in the optical near field is not a ultimate scaling limitation for our QW process implementation, as the Rayleigh range z_R can be made as large as desired by increasing the beam waist w_0. The beam waist w_0 scales as the square root of z_R. Hence, the overall needed resources of our QW implementation, defined as the number of needed optical devices multiplied by their transverse area, scales linearly in the number of steps n as long as w_0 can remain constant, while there is a crossover to the standard quadratic scaling when z_0 must be further increased.

Appendix E

Test of two-photon correlation inequalities in a quantum walk[1]

Let us consider two photons entering the QW apparatus in fixed states 1 and 2. Here, we use a notation in which the state label at input/output includes both the OAM and the polarization. In our experiment, labels $1, 2$ correspond to a vanishing OAM and L, R polarizations. The output states p will denote the combination of the OAM value m and horizontal or vertical linear polarizations H, V. The unitary evolution of each photon from these input states to the final states can be described by a matrix $U_{l',l}$, where the first index corresponds to the input state and the second to the output one (notice that here we are making no assumptions on this matrix, except for unitarity). Hence, the QW evolution can be described by the following operator transformation law

$$\hat{a}_{l'}^{\dagger} \rightarrow \hat{b}_{l'}^{\dagger} = \sum_{l} U_{l',l} \hat{a}_{l}^{\dagger} \tag{E.1}$$

Let us now discuss the inequalities constraining the measurable photon correlations in two specific reference cases. Our first reference case is that of two independent classical sources (or coherent quantum states with random relative phases) entering modes 1 and 2, in the place of single photons. The following inequality can be then proved to apply to the intensity correlations $\Gamma_{p,q} = \langle \hat{a}_p^{\dagger} \hat{a}_q^{\dagger} \hat{a}_p \hat{a}_q \rangle$, for any two given QW output modes p and q [129, 147]:

$$\frac{1}{3} \sqrt{\Gamma_{p,p} \Gamma_{q,q}} - \Gamma_{p,q} < 0. \tag{E.2}$$

[1] This appendix correspond to a section of the Supplementary Material of Ref. [106], which I coauthored.

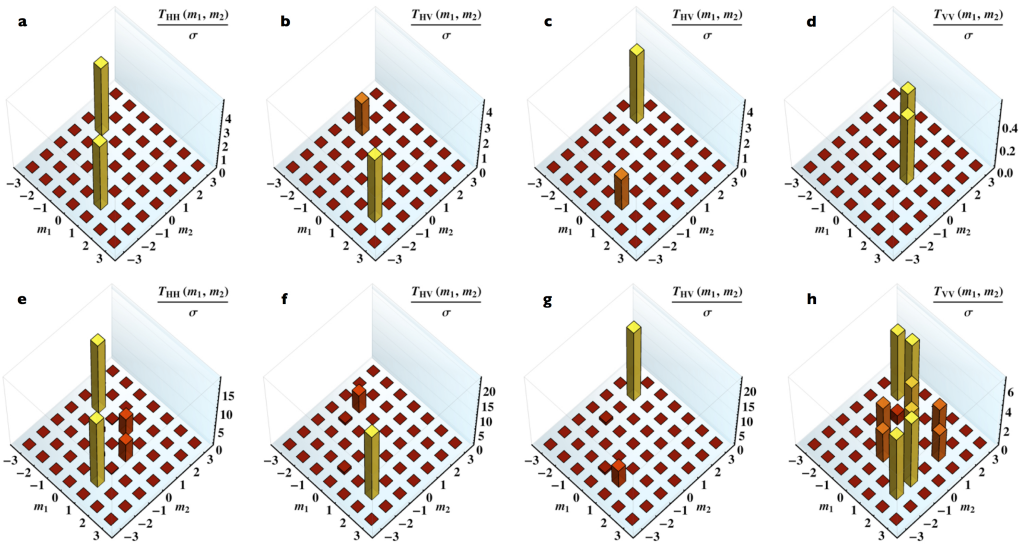

FIGURE E.1: Experimental violation of correlation inequalities for two photons which have completed the hybrid QW ($\delta = 1.46$). The data are based on the coincidences after the final beam-splitter. (a)-(d) Violations of the inequalities given in Eq. (E.4), constraining the correlations that would be obtained for two classical sources, incoherent to each other. Each panel refers to a different pair of measured polarizations for the two photons. These violations prove that our results can only be explained with quantum effects. (e)-(h) Violations of the inequalities given in Eq. (E.8), constraining the correlations obtained for two distinguishable photons. Again, each panel refers to a different pair of polarizations. These violations prove that our photons exhibit two-particle interferences. Only positive values of the $T_{p,q}$ are reported, while negative values which fulfil the inequality are omitted. All violations are given in units of Poissonian standard deviations σ, as determined from the coincidence counts. The color scale reflects the vertical scale.

In terms of two-photon detection probabilities $\bar{P}_{p,q} = (1 + \delta_{p,q})\Gamma_{p,q}$, the same inequality reads

$$\frac{2}{3}\sqrt{\bar{P}_{p,p}\bar{P}_{q,q}} - \bar{P}_{p,q} < 0, \tag{E.3}$$

where $\bar{P}_{p,q}$ stands for the probability of having state $|1_p, 1_q\rangle$, for $p \neq q$, or state $|2_p\rangle$, for $p = q$, after the QW but before the BS used to split the photons. After the BS, taking into account the photon-splitting probability, the inequality is rewritten as

$$T_{p,q} = \frac{1}{3}\sqrt{P_{p,p}P_{q,q}} - P_{p,q} < 0, \tag{E.4}$$

where $P_{p,q}$ is now the probability of detecting in coincidence a photon in state p at one (given) BS exit port and the other photon in state q at the other BS exit port.

Our second reference case is that of two single but distinguishable photons entering states 1 and 2. In this case, it is easy to prove a second stronger inequality for the

coincidence probabilities. Indeed, in this case one has

$$\bar{P}_{p,q} = |U_{1,p}U_{2,q}|^2 + |U_{1,q}U_{2,p}|^2 \tag{E.5}$$

for $p \neq q$ and

$$\bar{P}_{p,p} = |U_{1,p}U_{2,p}|^2, \tag{E.6}$$

where $\bar{P}_{p,q}$ now stands for the probability of having one of the two distinguishable photons in state p and the other in q after the QW, before the BS. The mathematical identity $(|U_{1,p}U_{2,q}| - |U_{1,q}U_{2,p}|)^2 > 0$ leads directly to the following inequality:

$$2\sqrt{\bar{P}_{p,p}\bar{P}_{q,q}} - \bar{P}_{p,q} < 0. \tag{E.7}$$

After the BS, this in turn is equivalent to

$$T_{p,q} = \sqrt{P_{p,p}P_{q,q}} - P_{p,q} < 0. \tag{E.8}$$

The violation of the first inequality (E.4) from our coincidence data would prove that the photon correlations cannot be mimicked by intensity correlations of classical sources. Panels (a-d) in Figs. 5.8 (standard QW) and E.1 (hybrid QW) show the set of violations found in our two-photon experiments, in units of Poissonian standard deviations. In some cases, the experimental violations are larger than 5 standard deviations, proving that the measured correlations are quantum. As these inequalities are valid for any possible unitary propagation of the photons, they are also independent of all possible misalignments of our setup. Hence, the use of statistical standard deviations to assess the violation magnitude is well justified.

The violation of the second inequality (E.8) from our data proves that the photon correlations are stronger than those allowed for two distinguishable photons, owing to the contribution of two-photon interferences. Although this is already demonstrated in some cases by the violation of the first inequality (as the violation of the first inequality logically implies the violation of the second one), this second inequality is stronger and should be therefore violated in a larger number of cases and with a larger statistical significance (although it requires assuming that there are two and only two photons at input, so that a classical source is excluded a priori). Panels (e-h) in Figs. 5.8 (standard QW) and E.1 (hybrid QW) show the observed violations. This time, certain measurements violate the inequality by as much as 15 standard deviations, thus proving that two-photon interferences play a very significant role in our experiment.

Bibliography

[1] O'Neil, A., MacVicar, I., Allen, L. & Padgett, M. Intrinsic and extrinsic nature of the orbital angular momentum of a light beam. *Phys. Rev. Lett.* **88**, 053601 (2002). URL http://link.aps.org/doi/10.1103/PhysRevLett.88.053601.

[2] Barnett, S. M. Optical angular-momentum flux. *Journal of Optics B: Quantum and Semiclassical Optics* **4**, S7 (2002).

[3] Allen, L., Beijersbergen, M., Spreeuw, R. & Woerdman, J. Orbital angular momentum of light and the transformation of Laguerre-Gaussian laser modes. *Phys. Rev. A* **45**, 8185–8189 (1992). URL http://link.aps.org/doi/10.1103/PhysRevA.45.8185.

[4] Yao, A. M. & Padgett, M. J. Orbital angular momentum: origins, behavior and applications. *Adv. Opt. Photon.* **3**, 161–204 (2011). URL http://aop.osa.org/abstract.cfm?URI=aop-3-2-161.

[5] Van Enk, S. J. & Nienhuis, G. Spin and orbital angular momentum of photons. *Europhysics Letters* **25**, 497 (1994).

[6] Van Enk, S. & Nienhuis, G. Commutation rules and eigenvalues of spin and orbital angular momentum of radiation fields. *Journal of Modern Optics* **41**, 963–977 (1994). URL http://dx.doi.org/10.1080/09500349414550911. http://dx.doi.org/10.1080/09500349414550911.

[7] Speirits, F. C. & Barnett, S. M. Do waves carrying orbital angular momentum possess azimuthal linear momentum? *Phys. Rev. Lett.* **111**, 103602 (2013). URL http://link.aps.org/doi/10.1103/PhysRevLett.111.103602.

[8] Slussarenko, S. *Novel tools for manipulating the photon orbital angular momentum and their application to classical and quantum optics*. Ph.D. thesis, Università degli Studi di Napoli Federico II (2010).

[9] Karimi, E. *Generation and manipulation of laser beams carrying orbital angular momentum for classical and quantum information applications*. Ph.D. thesis, Università degli Studi di Napoli Federico II (2009).

[10] Saleh, B. E. A. & Teich, M. C. *Fundamentals of photonics* (Wiley, 1990).

[11] Karimi, E., Zito, G., Piccirillo, B., Marrucci, L. & Santamato, E. Hypergeometric-Gaussian modes. *Opt. Lett.* **32**, 3053–3055 (2007). URL http://ol.osa.org/abstract.cfm?URI=ol-32-21-3053.

[12] Siegman, A. E. *Lasers* (University Science Books, 1986).

[13] Aiello, A., Toeppel, F., Marquardt, C., Giacobino, E. & Leuchs, G. Classical entanglement: Oxymoron or resource? *arXiv preprint arXiv:1409.0213* (2014).

[14] Marrucci, L. *et al.* Spin-to-orbital conversion of the angular momentum of light and its classical and quantum applications. *Journal of Optics* **13**, 064001 (2011). URL http://stacks.iop.org/2040-8986/13/i=6/a=064001.

[15] Piccirillo, B., D'Ambrosio, V., Slussarenko, S., Marrucci, L. & Santamato, E. Photon spin-to-orbital angular momentum conversion via an electrically tunable q-plate. *Applied Physics Letters* **97** (2010). URL http://scitation.aip.org/content/aip/journal/apl/97/24/10.1063/1.3527083.

[16] Karimi, E., Piccirillo, B., Nagali, E., Marrucci, L. & Santamato, E. Efficient generation and sorting of orbital angular momentum eigenmodes of light by thermally tuned q-plates. *Applied Physics Letters* **94**, – (2009). URL http://scitation.aip.org/content/aip/journal/apl/94/23/10.1063/1.3154549.

[17] Massa, F. *Realization of a Quantum Walk in the Orbital Angular Momentum Space of the Photon*. Master's thesis, Università degli Studi di Napoli Federico II (2013).

[18] Zhan, Q. Cylindrical vector beams: from mathematical concepts to applications. *Adv. Opt. Photon.* **1**, 1–57 (2009). URL http://aop.osa.org/abstract.cfm?URI=aop-1-1-1.

[19] Nye, J. F. & Hajnal, J. V. a. The wave structure of monochromatic electromagnetic radiation. *Proceedings of the Royal Society of London A: Mathematical, Physical and Engineering Sciences* **409**, 21–36 (1987). URL http://rspa.royalsocietypublishing.org/content/409/1836/21.abstract.

[20] Berry, M. V. & Dennis, M. R. a. Polarization singularities in isotropic random vector waves. *Proceedings of the Royal Society of London A: Mathematical, Physical and Engineering Sciences* **457**, 141–155 (2001). URL http://rspa.royalsocietypublishing.org/content/457/2005/141.abstract.

[21] Dennis, M. R., O'Holleran, K. & Padgett, M. J. Singular optics: optical vortices and polarization singularities. *Progress in Optics* **53**, 293–363 (2009).

[22] Dorn, R., Quabis, S. & Leuchs, G. Sharper focus for a radially polarized light beam. *Phys. Rev. Lett.* **91**, 233901 (2003). URL http://link.aps.org/doi/10.1103/PhysRevLett.91.233901.

[23] Novotny, L., Beversluis, M. R., Youngworth, K. S. & Brown, T. G. Longitudinal field modes probed by single molecules. *Phys. Rev. Lett.* **86**, 5251–5254 (2001). URL http://link.aps.org/doi/10.1103/PhysRevLett.86.5251.

[24] Varin, C. & Piché, M. Acceleration of ultra-relativistic electrons using high-intensity TM01 laser beams. *Applied Physics B* **74**, s83–s88 (2002). URL http://dx.doi.org/10.1007/s00340-002-0906-8.

[25] Lu, F., Zheng, W. & Huang, Z. Coherent anti-Stokes Raman scattering microscopy using tightly focused radially polarized light. *Opt. Lett.* **34**, 1870–1872 (2009). URL http://ol.osa.org/abstract.cfm?URI=ol-34-12-1870.

[26] Zhan, Q. Trapping metallic Rayleigh particles with radial polarization. *Opt. Express* **12**, 3377–3382 (2004). URL http://www.opticsexpress.org/abstract.cfm?URI=oe-12-15-3377.

[27] Anoop, K. K. *et al.* Femtosecond laser surface structuring of silicon using optical vortex beams generated by a q-plate. *Applied Physics Letters* **104**, 241604 (2014).

[28] Anoop, K. K. *et al.* Direct femtosecond laser ablation of copper with an optical vortex beam. *Journal of Applied Physics* **116**, – (2014). URL http://scitation.aip.org/content/aip/journal/jap/116/11/10.1063/1.4896068.

[29] D'Ambrosio, V. *et al.* Complete experimental toolbox for alignment-free quantum communication. *Nature Communications* **3**, 961 (2012). URL http://dx.doi.org/10.1038/ncomms1951.

[30] Vallone, G. *et al.* Free-space quantum key distribution by rotation-invariant twisted photons. *Phys. Rev. Lett.* **113**, 060503 (2014). URL http://link.aps.org/doi/10.1103/PhysRevLett.113.060503.

[31] Bauer, T. *et al.* Observation of optical polarization Möbius strips. *Science* **347**, 964–966 (2015). URL http://www.sciencemag.org/content/347/6225/964.abstract. http://www.sciencemag.org/content/347/6225/964.full.pdf.

[32] Oron, R. *et al.* The formation of laser beams with pure azimuthal or radial polarization. *Applied Physics Letters* **77** (2000).

[33] Kozawa, Y. & Sato, S. Generation of a radially polarized laser beam by use of a conical Brewster prism. *Opt. Lett.* **30**, 3063–3065 (2005). URL http://ol.osa.org/abstract.cfm?URI=ol-30-22-3063.

[34] Kawauchi, H., Kozawa, Y. & Sato, S. Generation of radially polarized Ti:Sapphire laser beam using a c-cut crystal. *Opt. Lett.* **33**, 1984–1986 (2008). URL http://ol.osa.org/abstract.cfm?URI=ol-33-17-1984.

[35] Bomzon, Z., Biener, G., Kleiner, V. & Hasman, E. Radially and azimuthally polarized beams generated by space-variant dielectric subwavelength gratings. *Opt. Lett.* **27**, 285–287 (2002). URL http://ol.osa.org/abstract.cfm?URI=ol-27-5-285.

[36] Wang, X.-L., Ding, J., Ni, W.-J., Guo, C.-S. & Wang, H.-T. Generation of arbitrary vector beams with a spatial light modulator and a common path interferometric arrangement. *Opt. Lett.* **32**, 3549–3551 (2007). URL http://ol.osa.org/abstract.cfm?URI=ol-32-24-3549.

[37] Zhang, X. & Qiu, L. Generation of radially and azimuthally polarized light by achromatic meniscus axicon. *Optical Engineering* **52**, 048001–048001 (2013). URL http://dx.doi.org/10.1117/1.OE.52.4.048001.

[38] Bouchard, F., Mand, H., Mirhosseini, M., Karimi, E. & Boyd, R. W. Achromatic orbital angular momentum generator. *New Journal of Physics* **16**, 123006 (2014).

[39] Cardano, F. *et al.* Polarization pattern of vector vortex beams generated by q-plates with different topological charges. *Appl. Opt.* **51**, C1–C6 (2012).

[40] Cardano, F., Karimi, E., Marrucci, L., de Lisio, C. & Santamato, E. Generation and dynamics of optical beams with polarization singularities. *Opt. Express* **21**, 8815–8820 (2013). URL http://www.opticsexpress.org/abstract.cfm?URI=oe-21-7-8815.

[41] Holleczek, A., Aiello, A., Gabriel, C., Marquardt, C. & Leuchs, G. Classical and quantum properties of cylindrically polarized states of light. *Opt. Express* **19**, 9714–9736 (2011). URL http://www.opticsexpress.org/abstract.cfm?URI=oe-19-10-9714.

[42] Milione, G., Sztul, H. I., Nolan, D. A. & Alfano, R. R. Higher-order Poincaré sphere, Stokes parameters, and the angular momentum of light. *Phys. Rev. Lett.* **107**, 053601 (2011). URL http://link.aps.org/doi/10.1103/PhysRevLett.107.053601.

[43] Freund, I. Polarization flowers. *Optics Communications* **199**, 47–63 (2001). URL http://www.sciencedirect.com/science/article/pii/S0030401801015334.

[44] Dennis, M. R. Polarization singularities in paraxial vector fields: morphology and statistics. *Optics Communications* **213**, 201–221 (2002). URL http://www.sciencedirect.com/science/article/pii/S0030401802020886.

[45] Flossmann, F., Schwarz, U. T., Maier, M. & Dennis, M. R. Polarization singularities from unfolding an optical vortex through a birefringent crystal. *Phys. Rev. Lett.* **95**, 253901 (2005). URL http://link.aps.org/doi/10.1103/PhysRevLett.95.253901.

[46] Berry, M., Dennis, M. & Lee Jr, R. Polarization singularities in the clear sky. *New Journal of Physics* **6**, 162 (2004).

[47] Angelsky, O., Mokhun, A., Mokhun, I. & Soskin, M. The relationship between topological characteristics of component vortices and polarization singularities. *Optics Communications* **207**, 57–65 (2002). URL http://www.sciencedirect.com/science/article/pii/S0030401802014797.

[48] Beckley, A. M., Brown, T. G. & Alonso, M. A. Full Poincaré beams. *Opt. Express* **18**, 10777–10785 (2010). URL http://www.opticsexpress.org/abstract.cfm?URI=oe-18-10-10777.

[49] Galvez, E. J., Khadka, S., Schubert, W. H. & Nomoto, S. Poincaré beam patterns produced by nonseparable superpositions of Laguerre-Gauss and polarization modes of light. *Appl. Opt.* **51**, 2925–2934 (2012). URL http://ao.osa.org/abstract.cfm?URI=ao-51-15-2925.

[50] Karimi, E., Piccirillo, B., Marrucci, L. & Santamato, E. Light propagation in a birefringent plate with topological charge. *Opt. Lett.* **34**, 1225–1227 (2009). URL http://ol.osa.org/abstract.cfm?URI=ol-34-8-1225.

[51] Einstein, A., Podolsky, B. & Rosen, N. Can quantum-mechanical description of physical reality be considered complete? *Physical Review* **47**, 777–780 (1935). URL http://link.aps.org/doi/10.1103/PhysRev.47.777.

[52] Bohm, D. A suggested interpretation of the quantum theory in terms of "hidden" variables. i. *Physical Review* **85**, 166–179 (1952). URL http://link.aps.org/doi/10.1103/PhysRev.85.166.

[53] Bell, J. On the Einstein-Podolsky-Rosen paradox. *Physics* **1** (1964).

[54] Bell, J. S. On the problem of hidden variables in quantum mechanics. *Reviews of Modern Physics* **38**, 447–452 (1966). URL http://link.aps.org/doi/10.1103/RevModPhys.38.447.

[55] Aspect, A., Dalibard, J. & Roger, G. Experimental test of Bell's inequalities using time- varying analyzers. *Physical Review Letters* **49**, 1804–1807 (1982). URL http://link.aps.org/doi/10.1103/PhysRevLett.49.1804.

[56] Leggett, A. Nonlocal hidden-variable theories and quantum mechanics: An incompatibility theorem. *Foundations of Physics* (2003).

[57] Gröblacher, S. *et al.* An experimental test of non-local realism. *Nature* **446**, 871–875 (2007). URL http://www.scopus.com/inward/record.url?eid=2-s2.0-34247361229&partnerID=40&md5=6c48092fab87c0dce89731554ebb8c4d.

[58] Branciard, C. *et al.* Experimental falsification of Leggett's nonlocal variable model. *Physical Review Letters* **99**, 210407– (2007). URL http://link.aps.org/doi/10.1103/PhysRevLett.99.210407.

[59] Paterek, T. *et al.* Experimental test of nonlocal realistic theories without the rotational symmetry assumption. *Physical Review Letters* **99**, 210406– (2007). URL http://link.aps.org/doi/10.1103/PhysRevLett.99.210406.

[60] Branciard, C. *et al.* Testing quantum correlations versus single-particle properties within Leggett/'s model and beyond. *Nature Physics* **4** (2009).

[61] Romero, J. *et al.* Violation of Leggett inequalities in orbital angular momentum subspaces. *New Journal of Physics* **12**, 123007 (2010). URL http://stacks.iop.org/1367-2630/12/i=12/a=123007.

[62] Michler, M., Weinfurter, H. & Żukowski, M. Experiments towards falsification of noncontextual hidden variable theories. *Phys. Rev. Lett.* **84**, 5457–5461 (2000). URL http://link.aps.org/doi/10.1103/PhysRevLett.84.5457.

[63] Mermin, N. D. Hidden variables and the two theorems of John Bell. *Reviews of Modern Physics* **65**, 803–815 (1993). URL http://link.aps.org/doi/10.1103/RevModPhys.65.803.

[64] Hardy, L. Nonlocality for two particles without inequalities for almost all entangled states. *Phys. Rev. Lett.* **71**, 1665–1668 (1993). URL http://link.aps.org/doi/10.1103/PhysRevLett.71.1665.

[65] Clauser, J. F., Horne, M. A., Shimony, A. & Holt, R. A. Proposed experiment to test local hidden-variable theories. *Physical Review Letters* **23**, 880–884 (1969). URL http://link.aps.org/doi/10.1103/PhysRevLett.23.880.

[66] Christensen, B. G. *et al.* Detection-loophole-free test of quantum nonlocality, and applications. *Phys. Rev. Lett.* **111**, 130406 (2013). URL http://link.aps.org/doi/10.1103/PhysRevLett.111.130406.

[67] Karimi, E. *et al.* Hardy's paradox tested in the spin-orbit Hilbert space of single photons. *Phys. Rev. A* **89**, 032122 (2014). URL http://link.aps.org/doi/10.1103/PhysRevA.89.032122.

[68] Mermin, N. D. Quantum mysteries refined. *American Journal of Physics* **62**, 880–886 (1994).

[69] Greenberger, D. M., Horne, M. A., Shimony, A. & Zeilinger, A. Bell's theorem without inequalities. *Am. J. Phys* **58**, 1131–1143 (1990).

[70] Torgerson, J. R., Branning, D., Monken, C. H. & Mandel, L. Experimental demonstration of the violation of local realism without Bell inequalities. *Physics Letters A* **204**, 323–328 (1995). URL http://www.sciencedirect.com/science/article/pii/037596019500486M.

[71] Di Giuseppe, G., De Martini, F. & Boschi, D. Experimental test of the violation of local realism in quantum mechanics without Bell inequalities. *Phys. Rev. A* **56**, 176–181 (1997). URL http://link.aps.org/doi/10.1103/PhysRevA.56.176.

[72] Boschi, D., Branca, S., De Martini, F. & Hardy, L. Ladder proof of nonlocality without inequalities: Theoretical and experimental results. *Phys. Rev. Lett.* **79**, 2755–2758 (1997). URL http://link.aps.org/doi/10.1103/PhysRevLett.79.2755.

[73] Lundeen, J. S. & Steinberg, A. M. Experimental joint weak measurement on a photon pair as a probe of Hardy's paradox. *Phys. Rev. Lett.* **102**, 020404 (2009). URL http://link.aps.org/doi/10.1103/PhysRevLett.102.020404.

[74] Vallone, G. *et al.* Testing Hardy's nonlocality proof with genuine energy-time entanglement. *Phys. Rev. A* **83**, 042105 (2011). URL http://link.aps.org/doi/10.1103/PhysRevA.83.042105.

[75] Fedrizzi, A., Almeida, M. P., Broome, M. A., White, A. G. & Barbieri, M. Hardy's paradox and violation of a state-independent Bell inequality in time. *Phys. Rev. Lett.* **106**, 200402 (2011). URL http://link.aps.org/doi/10.1103/PhysRevLett.106.200402.

[76] Chen, L. & Romero, J. Hardy's nonlocality proof using twisted photons. *Opt. Express* **20**, 21687–21692 (2012). URL http://www.opticsexpress.org/abstract.cfm?URI=oe-20-19-21687.

[77] Mair, A., Vaziri, A., Weihs, G. & Zeilinger, A. Entanglement of the orbital angular momentum states of photons. *Nature* **412**, 313–316 (2001). URL http://dx.doi.org/10.1038/35085529.

[78] Bolduc, E., Bent, N., Santamato, E., Karimi, E. & Boyd, R. W. Exact solution to simultaneous intensity and phase encryption with a single phase-only hologram.

Opt. Lett. **38**, 3546–3549 (2013). URL http://ol.osa.org/abstract.cfm?URI=ol-38-18-3546.

[79] D'Ambrosio, V. *et al.* Test of mutually unbiased bases for six-dimensional photonic quantum systems. *Scientific reports* **3** (2013).

[80] Cardano, F., Karimi, E., Marrucci, L., de Lisio, C. & Santamato, E. Violation of Leggett-type inequalities in the spin-orbit degrees of freedom of a single photon. *Phys. Rev. A* **88**, 032101 (2013). URL http://link.aps.org/doi/10.1103/PhysRevA.88.032101.

[81] Karimi, E. *et al.* Spin-orbit hybrid entanglement of photons and quantum contextuality. *Physical Review A* **82**, 022115– (2010). URL http://link.aps.org/doi/10.1103/PhysRevA.82.022115.

[82] Wootters, W. K. & Fields, B. D. Optimal state-determination by mutually unbiased measurements. *Annals of Physics* **191**, 363–381 (1989). URL http://www.sciencedirect.com/science/article/pii/0003491689903229.

[83] Gisin, N., Ribordy, G., Tittel, W. & Zbinden, H. Quantum cryptography. *Rev. Mod. Phys.* **74**, 145–195 (2002). URL http://link.aps.org/doi/10.1103/RevModPhys.74.145.

[84] Cabello, A., D'Ambrosio, V., Nagali, E. & Sciarrino, F. Hybrid ququart-encoded quantum cryptography protected by Kochen-Specker contextuality. *Phys. Rev. A* **84**, 030302 (2011). URL http://link.aps.org/doi/10.1103/PhysRevA.84.030302.

[85] Kochen, S. & Specker, E. P. The problem of hidden variables in quantum mechanics. *Journal of Mathematics and Mechanics* **17**, 59–87 (1967).

[86] Nagali, E., D'Ambrosio, V., Sciarrino, F. & Cabello, A. Experimental observation of impossible-to-beat quantum advantage on a hybrid photonic system. *Phys. Rev. Lett.* **108**, 090501 (2012). URL http://link.aps.org/doi/10.1103/PhysRevLett.108.090501.

[87] D'Ambrosio, V. *et al.* Experimental implementation of a Kochen-Specker set of quantum tests. *Phys. Rev. X* **3**, 011012 (2013). URL http://link.aps.org/doi/10.1103/PhysRevX.3.011012.

[88] Brukner, Č. Quantum complementarity and logical indeterminacy. *Natural Computing* **8**, 449–453 (2009). URL http://dx.doi.org/10.1007/s11047-009-9118-z.

[89] Cerf, N. J., Bourennane, M., Karlsson, A. & Gisin, N. Security of quantum key distribution using d-level systems. *Phys. Rev. Lett.* **88**, 127902 (2002). URL http://link.aps.org/doi/10.1103/PhysRevLett.88.127902.

[90] Caruso, F., Bechmann-Pasquinucci, H. & Macchiavello, C. Robustness of a quantum key distribution with two and three mutually unbiased bases. *Phys. Rev. A* **72**, 032340 (2005). URL http://link.aps.org/doi/10.1103/PhysRevA.72.032340.

[91] Ekert, A. K. Quantum cryptography based on Bell's theorem. *Phys. Rev. Lett.* **67**, 661–663 (1991). URL http://link.aps.org/doi/10.1103/PhysRevLett.67.661.

[92] Gröblacher, S., Jennewein, T., Vaziri, A., Weihs, G. & Zeilinger, A. Experimental quantum cryptography with qutrits. *New Journal of Physics* **8**, 75 (2006).

[93] Adamson, R. B. A. & Steinberg, A. M. Improving quantum state estimation with mutually unbiased bases. *Phys. Rev. Lett.* **105**, 030406 (2010). URL http://link.aps.org/doi/10.1103/PhysRevLett.105.030406.

[94] Giovannini, D. *et al.* Characterization of high-dimensional entangled systems via mutually unbiased measurements. *Phys. Rev. Lett.* **110**, 143601 (2013). URL http://link.aps.org/doi/10.1103/PhysRevLett.110.143601.

[95] Lima, G. *et al.* Experimental quantum tomography of photonic qudits via mutually unbiased basis. *Opt. Express* **19**, 3542–3552 (2011). URL http://www.opticsexpress.org/abstract.cfm?URI=oe-19-4-3542.

[96] Nagali, E., Sansoni, L., Marrucci, L., Santamato, E. & Sciarrino, F. Experimental generation and characterization of single-photon hybrid ququarts based on polarization and orbital angular momentum encoding. *Phys. Rev. A* **81**, 052317 (2010). URL http://link.aps.org/doi/10.1103/PhysRevA.81.052317.

[97] Durt, T., Englert, B.-G., Bengtsson, I. & Życzkowski, K. On mutually unbiased bases. *International journal of quantum information* **8**, 535–640 (2010).

[98] Planat, M., Rosu, H. & Perrine, S. A survey of finite algebraic geometrical structures underlying mutually unbiased quantum measurements. *Foundations of Physics* **36**, 1662–1680 (2006). URL http://dx.doi.org/10.1007/s10701-006-9079-3.

[99] Archer, C. There is no generalization of known formulas for mutually unbiased bases. *arXiv preprint quant-ph/0312204* (2003).

[100] Butterley, P. & Hall, W. Numerical evidence for the maximum number of mutually unbiased bases in dimension six. *Physics Letters A* **369**, 5–8 (2007). URL http://www.sciencedirect.com/science/article/pii/S0375960107006111.

[101] Klappenecker, A. & Rötteler, M. Constructions of mutually unbiased bases. In *Finite fields and applications*, 137–144 (Springer, 2004).

[102] McNulty, D. & Weigert, S. On the impossibility to extend triples of mutually unbiased product bases in dimension six. *International Journal of Quantum Information* **10** (2012).

[103] McNulty, D. & Weigert, S. The limited role of mutually unbiased product bases in dimension 6. *Journal of Physics A: Mathematical and Theoretical* **45**, 102001 (2012).

[104] James, D. F. V., Kwiat, P. G., Munro, W. J. & White, A. G. Measurement of qubits. *Phys. Rev. A* **64**, 052312 (2001). URL http://link.aps.org/doi/10.1103/PhysRevA.64.052312.

[105] Altepeter, J. B., Jeffrey, E. R., Kwiat, P. G., Berman, P. R. & Lin, C. C. *Photonic State Tomography*, vol. 52, 105–159 (Academic Press, 2005). URL http://www.sciencedirect.com/science/article/pii/S1049250X05520032.

[106] Cardano, F. *et al.* Quantum walks and wavepacket dynamics on a lattice with twisted photons. *Science Advances* **1** (2015). URL http://advances.sciencemag.org/content/1/2/e1500087.abstract.

[107] Kempe, J. Quantum random walks: an introductory overview. *Contemporary Physics* **44**, 307–327 (2003).

[108] Venegas-Andraca, S. E. Quantum walks: a comprehensive review. *Quantum Information Processing* **11**, 1015–1106 (2012). URL http://dx.doi.org/10.1007/s11128-012-0432-5.

[109] Shenvi, N., Kempe, J. & Whaley, B. Quantum random-walk search algorithm. *Phys. Rev. A* **67**, 052307 (2003).

[110] A.Childs & J.Goldstone. Spatial search by quantum walk. *Phys. Rev. A* **70**, 022314 (2004).

[111] Kendon, V. A random walk approach to quantum algorithms. *Phil. Trans. R. Soc. A* **364** (2006).

[112] Potoček, V., Gábris, A., Kiss, T. & Jex, I. Optimized quantum random-walk search algorithms on the hypercube. *Phys. Rev. A* **79**, 012325 (2009). URL http://link.aps.org/doi/10.1103/PhysRevA.79.012325.

[113] Childs, A. Universal computation by quantum walks. *Phys. Rev .Lett.* **102**, 180501 (2009).

[114] Lovett, N. B., Cooper, S., Everitt, M., Trevers, M. & Kendon, V. Universal quantum computation using the discrete-time quantum walk. *Phys. Rev. A* **81**, 042330 (2010). URL http://link.aps.org/doi/10.1103/PhysRevA.81.042330.

[115] Childs, A. M., Gosset, D. & Webb, Z. Universal computation by multiparticle quantum walk. *Science* **339**, 791–794 (2013). URL http://www.sciencemag.org/content/339/6121/791.abstract. http://www.sciencemag.org/content/339/6121/791.full.pdf.

[116] Mohseni, M., Rebentrost, P., Lloyd, S. & Aspuru-Guzik, A. Environment-assisted quantum walks in photosynthetic energy transfer. *J. Chem. Phys* **129** (2008). URL http://scitation.aip.org/content/aip/journal/jcp/129/17/10.1063/1.3002335.

[117] Crespi, A. *et al.* Anderson localization of entangled photons in an integrated quantum walk. *Nat. Phot.* **7**, 322–328 (2013).

[118] Qi, X. & Zhang, S. Topological insulators and superconductors. *Rev. Mod. Phys.* **83**, 1057–1110 (2011). URL http://link.aps.org/doi/10.1103/RevModPhys.83.1057.

[119] Kitagawa, T., Rudner, M. S., Berg, E. & Demler, E. Exploring topological phases with quantum walks. *Phys. Rev. A* **82**, 033429 (2010). URL http://link.aps.org/doi/10.1103/PhysRevA.82.033429.

[120] Kitagawa, T. *et al.* Observation of topologically protected bound states in photonic quantum walks. *Nat. Commun.* **3** (2012).

[121] Wang, J. & Manouchehri, K. *Physical Implementation of Quantum Walks* (Springer, 2013).

[122] Schmitz, H. *et al.* Quantum walk of a trapped ion in phase space. *Phys. Rev. Lett.* **103**, 090504 (2009). URL http://link.aps.org/doi/10.1103/PhysRevLett.103.090504.

[123] Zähringer, F. *et al.* Realization of a quantum walk with one and two trapped ions. *Phys. Rev. Lett.* **104**, 100503 (2010). URL http://link.aps.org/doi/10.1103/PhysRevLett.104.100503.

[124] Karski, M. *et al.* Quantum walk in position space with single optically trapped atoms. *Science* **325**, 174–177 (2009). URL http://www.sciencemag.org/content/325/5937/174.abstract.

[125] Ryan, C. A., Laforest, M., Boileau, J. C. & Laflamme, R. Experimental implementation of a discrete-time quantum random walk on an NMR quantum-information processor. *Phys. Rev. A* **72**, 062317 (2005). URL http://link.aps.org/doi/10.1103/PhysRevA.72.062317.

[126] Zhang, P. *et al.* Demonstration of one-dimensional quantum random walks using orbital angular momentum of photons. *Phys. Rev. A* **75**, 052310 (2007). URL http://link.aps.org/doi/10.1103/PhysRevA.75.052310.

[127] Broome, M. A. *et al.* Discrete single-photon quantum walks with tunable decoherence. *Phys. Rev .Lett.* **104**, 153602 (2010).

[128] Schreiber, A. *et al.* Photons walking the line: A quantum walk with adjustable coin operations. *Phys. Rev .Lett.* **104**, 050502 (2010).

[129] A.Peruzzo *et al.* Quantum walks of correlated photons. *Science* **329**, 1500–1503 (2010).

[130] Owens, J. O. *et al.* Two-photon quantum walks in an elliptical direct-write waveguide array. *New J. Phys.* **13**, 075003 (2011).

[131] Sansoni, L. *et al.* Two-particle bosonic-fermionic quantum walk via integrated photonics. *Phys. Rev. Lett.* **108**, 010502 (2012).

[132] Schreiber, A. *et al.* A 2d quantum walk simulation of two-particle dynamics. *Science* **336**, 55–58 (2012). URL http://www.sciencemag.org/content/336/6077/55.abstract.

[133] Zhang, P. *et al.* Implementation of one-dimensional quantum walks on spin-orbital angular momentum space of photons. *Phys. Rev. A* **81**, 052322 (2010).

[134] Abal, G., Siri, R., Romanelli, A. & Donangelo, R. Quantum walk on the line: Entanglement and nonlocal initial conditions. *Phys. Rev. A* **73**, 042302 (2006). URL http://link.aps.org/doi/10.1103/PhysRevA.73.042302.

[135] de Valcárcel, G. J., Roldán, E. & Romanelli, A. Tailoring discrete quantum walk dynamics via extended initial conditions. *New Journal of Physics* **12**, 123022 (2010).

[136] Vieira, R., Amorim, E. P. M. & Rigolin, G. Dynamically disordered quantum walk as a maximal entanglement generator. *Phys. Rev. Lett.* **111**, 180503 (2013). URL http://link.aps.org/doi/10.1103/PhysRevLett.111.180503.

[137] Knight, P. L., Roldán, E. & Sipe, J. E. Quantum walk on the line as an interference phenomenon. *Phys. Rev. A* **68**, 020301 (2003). URL http://link.aps.org/doi/10.1103/PhysRevA.68.020301.

[138] Atala, M. *et al.* Direct measurement of the Zak phase in topological Bloch bands. *Nature Phys.* **9**, 795–800 (2013).

[139] Xiao, D., Chang, M. & Niu, Q. Berry phase effects on electronic properties. *Rev. Mod. Phys.* **82**, 1959–2007 (2010). URL http://link.aps.org/doi/10.1103/RevModPhys.82.1959.

[140] Gomes, K. K., Mar, W., Ko, W., Guinea, F. & Manoharan, H. C. Designer Dirac fermions and topological phases in molecular graphene. *Nature* **483**, 306–310 (2012). URL http://dx.doi.org/10.1038/nature10941.

[141] Genske, M. *et al.* Electric quantum walks with individual atoms. *Phys. Rev. Lett.* **110**, 190601 (2013). URL http://link.aps.org/doi/10.1103/PhysRevLett.110.190601.

[142] Su, W., Schrieffer, J. & Heeger, A. Solitons in polyacetylene. *Phys. Rev. Lett.* **42**, 1698–1701 (1979). URL http://link.aps.org/doi/10.1103/PhysRevLett.42.1698.

[143] Pittman, T. B., Shih, Y. H., Sergienko, A. V. & Rubin, M. H. Experimental tests of Bell's inequalities based on space-time and spin variables. *Phys. Rev. A* **51**, 3495–3498 (1995). URL http://link.aps.org/doi/10.1103/PhysRevA.51.3495.

[144] Kwiat, P. G. *et al.* New high-intensity source of polarization-entangled photon pairs. *Phys. Rev. Lett.* **75**, 4337–4341 (1995). URL http://link.aps.org/doi/10.1103/PhysRevLett.75.4337.

[145] C.K.Hong, Z. & L.Mandel. Measurement of subpicosecond time intervals between two photons by interference. *Phys. Rev .Lett.* **59**, 2044–2046 (1987).

[146] Vitelli, C. *et al.* Joining the quantum state of two photons into one. *Nat. Photon.* **7**, 521–526 (2013).

[147] Bromberg, Y., Lahini, Y., Morandotti, R. & Silberberg, Y. Quantum and classical correlations in waveguide lattices. *Phys. Rev. Lett.* **102**, 253904 (2009).